Carbonation of ophiolitic ultramafic rocks: Listvenite formation in the Late Cretaceous ophiolites of eastern Iran

Arman Boskabadi[1, 2], Iain K. Pitcairn[2], Matthew I. Leybourne[3], Damon A. H. Teagle[4], Matthew J. Cooper[4], Hossein Hadizadeh[5], Rasoul Nasiri Bezenjani[6], Reza Monazzami Bagherzadeh[5]

1. Geosciences Department, University of Texas at Dallas, Richardson, TX 75080, USA
2. Department of Geological Sciences, Stockholm University, Stockholm, Sweden
3. Queen's Facility for Isotope Research (QFIR), Department of Geological Sciences and Geological Engineering, and McDonald Institute, Canadian Particle Astrophysics Research Centre, Stirling Hall, Department of Physics, Engineering Physics & Astronomy, Queen's University, Kingston, Ontario, Canada K7L 3N6
4. School of Ocean and Earth Science, National Oceanography Centre Southampton, University of Southampton, Southampton, SO14 3ZH, UK
5. Geological Survey of Iran, North East Territory, Mashhad, Iran
6. Pars Olang Engineering Consultant Company, Tehran, Iran

Abstract:

Late Cretaceous mantle peridotite of the Birjand ophiolite (eastern Iran) contains variably serpentinized and carbonated/listvenitized rocks. Transformation from harzburgite protolith to final listvenite (quartz + magnesite/± dolomite + relict Cr-spinel) reflects successive fluid-driven reactions, the products of which are preserved in outcrop. Transformation of harzburgite to listvenite starts with lizardite serpentinization, followed by contemporaneous carbonation and antigorite serpentinization, antigorite-talc-magnesite alteration, finally

producing listvenite where alteration is most pervasive. The spectrum of listvenitic assemblages includes silica-carbonate, carbonate and silica listvenites with the latter (also known as birbirite) being the youngest, based on crosscutting relationships. The petrological observations and mineral assemblages suggest hydrothermal fluids responsible for the lizardite serpentinization had low aCO_2, oxygen and sulfur fugacities, distinct from those causing antigorite serpentinization and carbonation/listvenitization, which had higher aCO_2, $aSiO_2$, and oxygen and sulfur fugacities. The carbonate and silica listvenite end-members indicate variations in $aSiO_2$ and aCO_2 of the percolating hydrothermal fluids, most likely driven by local variations in pH and temperature.

Beyond the addition of H_2O, serpentinization did not significantly redistribute major elements. Progressive infiltration of CO_2-rich fluids and consequent carbonation segregated Mg into carbonate and Si into silica listvenites. Trace element mobility resulted in different enrichments of fluid-mobile, high field strength, and light rare earth elements in listvenites, indicating a "listvenite mobility sequence".

The $\delta^{13}C$, $\delta^{18}O$ and $^{87}Sr/^{86}Sr$ values of magnesite and dolomite in carbonated lithologies and veins point to sedimentary carbonate as the main C source. Fluid-mobile element (e.g., As and Sb) patterns in carbonated lithologies are consistent with contribution of subducted sediments in a forearc setting, suggesting sediment-derived fluids. Such fluids were produced by expulsion of pore fluids and release of structurally bound fluid from carbonate-bearing sediments in the Sistan Suture Zone (SsSZ) accretionary complex at shallow parts of mantle wedge. The CO_2-bearing fluids migrated up along the slab-mantle interface and circulated through the suture zone faults to be sequestered in mantle peridotites with marked element mobility signatures.

Keywords: Peridotite CO_2-sequestration; lizardite-antigorite serpentinization; listvenite; element mobility; C, O and Sr isotopes; Birjand ophiolite

1. Introduction

Ultramafic rocks are not thermodynamically stable under low temperatures in near-surface environments and undergo serpentinization hydration reactions on contact with aqueous fluids (McCollom and Bach, 2009). Carbonation of ophiolitic ultramafic rocks is driven by infiltration of CO_2-bearing fluids causing anhydrous primary minerals such as olivine and pyroxene or secondary hydrous minerals such as serpentine to be replaced by Ca-Mg carbonates and silicates such as quartz and talc with a lower MgO/SiO_2 than serpentine (O'Hanley, 1996). Extensive alteration of ultramafic rocks by CO_2-rich fluids can yield a quartz-carbonate replacement rock termed "listvenite". This name was used by Rose (1837) to describe auriferous silica-carbonate metasomatic rocks in Listvenya Gora in the Urals of Russia. The term is defined differently by various workers (compare definitions of Halls and Zhao, 1995 and Falk and Kelemen, 2015). We define listvenite as a spectrum of quartz-carbonate alteration products of ultramafic rocks, as demonstrated by the presence of chrome spinel (Cr-spinel) relicts. Confusion is further compounded by the different spellings: listvenite, listvanite, listwanite, and listwaenite.

Listvenites have long been of interest to economic geologists due to a spatial relationship with some Au-bearing ore deposits (Buisson and Leblanc, 1985; Auclair et al., 1993; Ucurum, 2000; Zoheir and Lehmann, 2011). Carbonate alteration of ultramafic rocks has recently attracted broader scientific attention for two additional reasons: 1) Active carbonate dominated hydrothermal systems with carbonate vents and carbonated peridotite basement rocks have been discovered on the seafloor, e.g. at Lost City on the Mid-Atlantic ridge (Kelley et al., 2005) and the Shinkai Seep Field in the Mariana convergent margin (Okumura et al., 2016); and 2) because listvenites serve as natural analogs for subsurface mineral carbon storage zones in peridotites (Hansen et al., 2005; Kelemen et al., 2011), especially in the Samail ophiolite of NE Oman where peridotites and listvenites have recently been drilled for detailed study (Kelemen et al., 2013). Understanding these processes aids in designing systems for carbon storage (Seifritz, 1990; Lackner et al., 1995; Hansen et al., 2005; Kelemen and Matter, 2008). In this paper, we contribute to the understanding of how CO_2-rich fluids interact with mantle peridotite to

produce listvenite by presenting evidence and interpretations from a listvenite reaction zone in the Late Cretaceous Birjand ophiolite of eastern Iran (Fig. 1), which formed about the same time as the Wadi Mansah listvenites in Oman (~97 Ma; Falk and Kelemen, 2015).

In Iran, carbonated peridotites are mainly associated with Neotethyan (Late Cretaceous) ophiolites and have been reported by several researchers (e.g., Zarrinkoub et al., 2005; Monazzami Bagherzadeh et al., 2013; Aftabi and Zarrinkoub, 2013; Ghorbani, 2013), but these rocks are poorly studied compared to, for example, those in Oman. Extensive listvenite crops out in the Hangaran area within the Birjand ophiolites of eastern Iran. This is the only listvenite locality in Iran that has been explored for gold mineralization by the Geological Survey of Iran (GSI). The economic significance of listvenites due to their association with gold mineralization has been the focus of most studies, but the source of carbonate-rich fluid that caused the listvenitization and associated magnesite deposits remain poorly understood. With the exception of a single pilot study on the Hangaran listvenite, no other isotopic data have been published for Iranian listvenites and therefore the source of the hydrothermal fluid is unconstrained (Monazzami Bagherzadeh et al., 2013). Here, we report results of field and petrographic studies along with geochemical and stable (C, O and S) and radiogenic (Sr) isotope analyses from outcrop and drill core samples and compare these data with that for carbonated peridotites and listvenites from other global examples to better understand conditions of listvenitization, sources of carbon and the extent to which elements were mobilized by hydrothermal alteration.

2. Geological Setting

The ophiolites of Iran are part of the Tethyan ophiolite belt, that connects the eastern Mediterranean ophiolites in the west with SW Asian ophiolites in the east. An overview of the Paleozoic and Mesozoic ophiolites in Iran is provided in figure 1.

The Hangaran massif is a part of the Birjand ophiolite that is located about 80 km south of Birjand, between 32° 04′ 30″ to 32° 06′ 30″ N and 59° 11′ 50″ to 59° 15′ 00″ E (Fig. 1 and 2). A Late Cretaceous ophiolite belt crops out in eastern Iran within the Sistan Suture Zone (SsSZ). The N-S trending SsSZ is a remnant of the Neotethyan ocean seaway (Tirrul et al., 1983), that closed during Paleocene-Oligocene collision, between the Afghan and Lut continental blocks (Fig. 1b). Oceanic lithospheric slices preserved by these Cretaceous ophiolites are mixed with Late Cretaceous-Paleogene volcano-sedimentary rocks of the Neh and Ratuk Complexes and the Sefidabeh forearc basin (Tirrul et al., 1983). The Neh and Ratuk Complexes are mélanges and probably formed in accretionary prisms. These complexes comprise three basic lithologic associations: (i) fault-bounded blocks of ophiolite (~30 % of outcrop) and related pelagic sedimentary rocks; (ii) Late Cretaceous to Eocene phyllite and weakly metamorphosed turbidites and (iii) Paleogene unmetamorphosed terrigenous marine sedimentary rocks. Cenomanian to Eocene deep-marine carbonates and calc-alkaline volcanic rocks of the Sefidabeh forearc basin overlay the Neh and Ratuk Complexes (e.g., Tirrul et al., 1983; Moghadam and Stern, 2015). Widespread calc-alkaline and alkaline volcanic rocks together with syntectonic to post-tectonic intrusions range in age from Late Cretaceous to Neogene (Camp and Griffis, 1982; Sadeghian et al., 2005). The most striking feature of the SsSZ accretionary prism is the occurrence of slices of the high-P metamorphic rocks including blueschist and eclogite. These rocks occur within the ophiolitic mélange of the Ratuk Complex and in the Sulabest region (Fig. 1b) yield Late Cretaceous radiometric ages for the high-P metamorphism of their mafic protoliths (Bröcker et al., 2013).

From north to south, the main SsSZ ophiolitic occurrences include the Birjand, Nehbandan and Tchehel Kure ophiolites (Delavari et al., 2009; Saccani et al., 2010; Fig. 1b). Moghadam and Stern (2015) reported harzburgite (including Cpx-bearing varieties), dunite and chromitite lenses in the Birjand mantle sequence occurring together with massive to pillowed lavas for the crustal section. These rocks are covered by pelagic sedimentary and associated pyroclastic rocks. Minor troctolite, olivine gabbro and leucogabbro also crop out in the Birjand ophiolites (Zarrinkoub et al., 2012).

3. Field relationships and sampling

115 The study area has been divided in two subareas (I) and (II) for geological exploration by the GSI, including
116 drilling of three boreholes to ~80 m deep in subarea (II). The main rock units include Late Cretaceous ophiolites
117 and ophiolitic mélange with dolerite (diabase) dikes and minor gabbro, andesitic tuff, shale, sandstone and
118 pelagic limestone (Fig. 2). Two outcrops of pelagic limestone occur several hundred meters to the west and east
119 of the mapped area. Paleogene rock units include granitic intrusions with associated quartzofeldspathic veins.
120 Quaternary alluvial deposits and terraces are the youngest geological units in the area. Partially serpentinized
121 harzburgites are the most abundant rocks in the area. Occurring together with small gabbro bodies, the
122 harzburgites are the least altered ultramafic rocks in the area and grade laterally into listvenite bodies through
123 dark grey lizardite-rich (Lz-serpentinite) to strongly sheared greenish grey antigorite-rich (Atg-serpentinite)
124 variably carbonated serpentinites (Fig. 3a, c, d). In places, white magnesite stockworks occur in partially
125 serpentinized harzburgites (Fig. 3b).

126 Lz-serpentinites are commonly carbonate-poor and occur between partially serpentinized harzburgite and
127 carbonated lithologies. The Lz-serpentinites grade into variably carbonated Atg-serpentinites at the margins of
128 listvenites. The degree of carbonate alteration increases from Lz-serpentinite towards Atg-serpentinite and
129 finally listvenite. In places, the transition between the serpentinite and listvenite is highly weathered (Fig. 3e, f).
130 Listvenites are spatially associated with faults and shear zones (Fig. 2). The higher elevation of listvenite
131 outcrops reflects the greater resistance of these rocks to erosion relative to their ophiolitic hosts (Fig. 3a). The
132 shear zones are branches of the West Nehbandan fault (WNF, Fig. 1b) and occur within an area of about 5 × 20
133 km trending E-W from the Hangaran area in the west to the Pustin area in the east. Two sets of fractures are
134 reported in the listvenite bodies (Monazzami Bagherzadeh et al., 2013). The first set trends NW-SE, and the
135 second set trends NNE-SSW.

136 In the field, listvenites form lenses, pods and planar vein bodies vary from 1 to 400 m wide and a few meters to
137 several kilometers long with a general NW-SE trend, parallel to the WNF. They are commonly hosted by Atg-
138 serpentinite that occur in Lz-serpentinite but have no direct contact with partially serpentinized harzburgite.

Based on the quartz and carbonate abundances and thus chemical composition, the listvenites can be grouped into three principal types: silica-carbonate, carbonate and silica listvenites (Fig. 2, 4a-c). The degree of deformation in listvenite increases from the core of the bodies to the margins where they are commonly foliated and/or brecciated along fault zones (Fig. 4e, f). Crosscutting relationships show that listvenites were intruded by several generations of late carbonate (mainly dolomite) or quartz veins. There is no surface or drillcore evidence for any igneous bodies directly associated with the listvenites.

Silica-carbonate and carbonate listvenites occur as pinkish cream on the surface, but grey when fresh (drill core) and can only be distinguished from each other in hand specimen based on more hardness of the former (Fig. 4a, b). In some cases, mesh texture is preserved and visible in the core of the bodies away from the fault zones. Silica-carbonate and carbonate listvenite bodies have variable thickness and grade into Atg-serpentinite either through a weathered zone or sharp contact. They are the most abundant listvenite-types in the Hangaran area hosting subordinate silica listvenite in the center of shear zones (Fig. 2, 3g).

Silica listvenites (also called birbirite; Auclair et al., 1993; Akbulut et al., 2006) are highly porous pink to reddish-brown when weathered, and less porous brown to dark grey or black when fresh, as seen in drill core (Fig. 4c, d). The pink color is caused by supergene oxidation of abundant sulfide minerals to hematite, goethite and limonite. Silica listvenites formed later than the other listvenite types and form smaller bodies up to 20m wide and few hundreds of meters long. These rocks are harder than other types of listvenites due to the abundance of quartz and form the highest relief in the region (Fig. 3g).

In order to investigate the carbonation processes, the sources of carbonating fluids and the chemical changes that occurred during alteration of the ophiolitic rocks, a suite of 33 rock samples with different degree of carbonate alteration and their associated veins were collected from two adjacent localities. In addition, four samples were collected from the BH1 drill core from depths of 59 to 65 m. Sample locations, lithologies and mineral paragenesis observed in different rock types are presented in Table 1.

4. Analytical methods

Scanning Electron Microscope

Polished thin-sections of selected partially serpentinized harzburgite, serpentinites, listvenites and carbonate veins were examined with a Philips XL30 FEG environmental scanning electron microscope (ESEM) at Stockholm University, operating at 20 kV and equipped with OXFORD energy dispersive analytical X-ray spectrometer.

Electron Microprobe

Quantitative electron microprobe analyses of Cr-spinel, silicate and carbonate minerals were carried out using a Field Emission Electron Probe Microanalyser (FE-EPMA), JXA8530F JEOL SUPERPROBE at the Center for Experimental Mineralogy, Petrology and Geochemistry (CEMPEG), Uppsala University, Sweden; operating at 15 kV accelerating voltage and 10 nA probe current. Beam diameters of 1, 5, and 2 µm were used for Cr-spinel, silicates, and carbonates, respectively. Raw data counts were corrected using the PAP routine. Natural and synthetic mineral standards were used for calibration. The results are reported in Table 4 and Supplementary Table S1.

Raman spectrometry

Raman spectroscopy was performed at Stockholm University applying a laser Raman confocal spectrometer (Horiba instrument LabRAM HR 800) equipped with a multichannel air-cooled CCD detector. Raman spectroscopy was mainly used for identifying different serpentine phases, carbonate and sulfide minerals. An argon laser wavelength of λ = 514 nm was provided as the excitation source with an 8 mW output power. The spectral resolution is about 0.3 cm^{-1}. The laser beam was focused onto an area of 1 µm with an integrated

183 Olympus^{TM} microscope coupled to the spectrometer. The instrument was calibrated using a silicon standard
184 (520.7 cm^{-1}) and neon lamp. Instrument control and data acquisition was done using LabSpec 5 software.

185 Bulk-rock major and trace element analyses

186 Hand specimen samples were powdered separately using a hardened stainless steel mill at Stockholm
187 University. Bulk-rock geochemical analyses were performed at ALS Geochemistry, Vancouver, B.C., Canada and
188 included the following: 1) major elements were analyzed by inductively coupled plasma atomic emission
189 spectroscopy (ICP-AES) following lithium metaborate fusion ($LiBO_2/Li_2B_4O_7$; the resultant melt was digested in
190 4% HNO_3/2% HCl); 2) Cr and Ba by ICP-mass spectrometry following lithium metaborate fusion (Method ME-
191 MS81); and 3) trace elements by an ultra-trace four-acid digestion (HF, $HClO_4$, HCl, HNO_3) method (ME-MS61L)
192 followed by a mixture of ICP-AES and ICP-MS analysis. For the most depleted samples, some analyses (especially
193 the rare earth elements) were below the published, conservative, detection limits. For these samples, the
194 detection limit filter was removed and data above blank levels is reported here. Loss on ignition was determined
195 by difference in weight after 1 g sample was heated at 1000 °C for 1 hour. Many certified reference materials
196 were analyzed concurrently for different components of the analysis i.e., major elements by fusion (AMIS0085,
197 AMIS0167, AMIS0304, SRM88B, SY-4), trace elements by fusion (OREAS 146, SY-4), trace elements by four acid
198 digestion (MRGeo08, OREAS 905, OREAS-104, OREAS-45b) and loss on ignition (AMIS0286, SARM-43). Except
199 where analyses are close to detection, RSD values are < 2-3 %. The major and trace element concentrations of
200 28 analyzed samples are reported in Table 2.

201 Gold analyses

202 Gold analyses were performed at Stockholm University, using Thermo XSeries 2 ICP-MS following the ultra-low
203 detection limit method described in Pitcairn et al. (2006). A 3σ detection limit of 0.033 ppb Au is obtained for
204 this method. Analytical precision were controlled through analyzing several reference materials including TDB1,
205 WMS-1 and CH-4. The gold concentrations of 28 samples are reported in Table 2.

206 Stable isotopes (C, O and S)

207 Carbon and oxygen isotope analyses were carried out on 30 samples of (i) carbonate fraction of partially
208 serpentinized harzburgite, serpentinite and listvenite samples, (ii) micro-drilled carbonate veins associated with
209 listvenite core samples, (iii) dolomite, (iv) stockwork cryptocrystalline magnesite, (v) pelagic limestone, and for
210 sulfur isotope were carried out on micro-drilled pyrite vein from three sulfide-rich listvenites. Sample powders
211 of carbonates and pyrite were analyzed for $\delta^{13}C$, $\delta^{18}O$, $\delta^{33}S$ and $\delta^{34}S$ at the Stable Isotope Laboratory at the
212 Department of Geological Sciences at Stockholm University. Sample aliquots of at least 0.25 mg carbonate were
213 reacted with excess 100 % phosphoric acid at 100 °C for six hours before analysis of CO_2 using a Gasbench II
214 connected to a MAT253 isotope ratio mass spectrometer (IRMS) from Thermo Scientific. Repeat analysis of
215 NBS18, IAEA-CO-1 and IAEA-CO-8 standards and two controls gave standard deviations better than 0.1 ‰ for
216 $\delta^{13}C$ and 0.15 ‰ for $\delta^{18}O$. The $\delta^{18}O$ values of samples prepared at 100 °C were analyzed with a dolomite oxygen
217 isotopic fractionation factor of 1.00901 using Rosenbaum and Sheppard, (1986) for dolomite, magnesite and a
218 mixture of both and a calcite oxygen isotopic fractionation factor of 1.00789 for calcite using Kim et al. (2015).
219 For normalization of the $\delta^{18}O$ results, we used two IAEA standards ranging from a $\delta^{18}O$ VPDB value of -2.44 ‰
220 (IAEA-CO-1; Brand et al., 2014) to a $\delta^{18}O$ VPDB value of -23.01 ‰ (NBS18; Verkouteren and Klinedinst, 2004).
221 Simultaneous $\delta^{33}S$ and $\delta^{34}S$ isotope measurements were carried out using a Carlo Erba NC2500 elemental
222 analyzer connected to the same MAT 253 IRMS. Analytical precision was performed through replicate analyses
223 of IAEA standards IAEA-SO-5, IAEA-SO-6 and NBS127 run as unknowns, while IAEA standards IAEA-S-1, IAEA-S-2
224 and IAEA-S-3 were analyzed to set up the calibration for each analytical run. Results are reported as per mil
225 (δ‰) values relative to the VPDB, VSMOW and VCDT scales for C, O and S isotopes, respectively (Table 3) with
226 an analytical uncertainty better than ±0.2 ‰.

227 Sr isotopes

Sr isotope analysis and Rb and Sr abundance on the same digests were performed at the University of Southampton. The calcite sample, H1-31, was dissolved in 5% acetic acid, the remaining magnesite rich samples were attacked with 2M HNO3 at 130 °C overnight. Rb and Sr concentration analyses were carried out on a Thermo Fisher Scientific XSeries 2 ICP-MS using synthetic mixed element standards with Be, In and Re as internal standards. The mother solutions were subsampled to give approximately 1 µg Sr and the Sr isolated using ~50 µl Sr-Spec resin columns, the column blanks were < 0.1 ng. The dried samples were loaded onto a single Ta filament with a Ta activator solution. $^{87}Sr/^{86}Sr$ was analyzed using static routine with amplifier rotation on a Thermo Fisher Scientific Triton Plus Thermal Ionization Mass Spectrometer with a beam size of ^{88}Sr = 2V. $^{87}Sr/^{86}Sr$ measurements were normalized to $^{86}Sr/^{88}Sr$ = 0.1194. The long-term average $^{87}Sr/^{86}Sr$ for NIST SRM987 on the instrument is 0.710245 ± 0.000025 (2sd) on 161 analyses. The results for 9 samples are reported in Table 3.

5. Results

5.1. Petrology and mineralogy

Table 1 lists the minerals observed in ultramafic and associated carbonate-altered rocks and Tables 4 and Supplementary Table S1 show representative microprobe analyses of minerals. We distinguish ten lithologies/veins in this study: partially serpentinized harzburgite, Lz- and Atg-serpentinites, cryptocrystalline magnesite vein, sedimentary limestone, silica listvenite, carbonate listvenite, silica-carbonate listvenite, dolomite vein (from outcrop), and dolomite vein in core. The last five lithologies comprise the listvenitic assemblage and their associated dolomite veins. Figure 5 shows the interpreted paragenetic sequence for the Hangaran ophiolitic rocks.

Partially serpentinized harzburgite

Harzburgites are medium- to coarse-grained and are variably serpentinized (~20-50 vol.%). Relicts of primary olivine, clinopyroxene, orthopyroxene and disseminated Cr-spinel are preserved (Fig. 6a). Olivine is fractured

with globular to rounded crystals altered to brucite and lizardite (Fig. 6b). Magnetite commonly occurs on mesh rims or forms along serpentine veins in highly serpentinized domains. Olivine grains are forsterite-rich and homogenous in composition with 0.12 wt.% MnO, 0.37 wt.% NiO, Cr_2O_3 <0.01 wt.% and Mg# [$Mg/(Mg+Fe^{2+})$] of 0.91 (Table 4). Orthopyroxene occurs as pale brown subhedral grains of enstatitic composition with 2.6 wt.% Al_2O_3, 0.8 wt.% CaO, 0.63 wt.% Cr_2O_3 and Mg# of 0.92. Clinopyroxene occurs as green subhedral grains of diopside with comparable Al_2O_3 (2.7 wt.%), higher CaO (23.8 wt.%) and Cr_2O_3 (0.75 wt.%), and Mg# of 0.97 compared to orthopyroxene. Orthopyroxene is more abundant than clinopyroxene and both are partially to strongly altered to lizardite/bastite. In addition to lizardite and bastite, minor chrysotile is also present. Minor antigorite is present with carbonate overprinting lizardite along veins (Fig. 6c). In the same rock, lizardite-after-olivine contains similar NiO contents (0.37 wt.%) with comparable SiO_2 (38.2 wt.%) and Mg# of 0.92 compared to olivine. Bastite-after-orthopyroxene has elevated NiO (0.37 wt.%), lower Al_2O_3 (0.35 wt.%) and SiO_2 (37.6 wt.%) with similar Mg# of 0.92 compared to orthopyroxene phase. Late lizardite crosscutting other minerals has highest SiO_2 (40.4 wt.%), lowest NiO (0.1 wt.%) and Mg# of 0.96 compared to other serpentine phases present in partially serpentinized harzburgite (Table 4). The presence of brucite was confirmed by Raman spectroscopy, but it was impossible to measure its composition due to its very small grain size. Primary Cr-spinel is dark brown in plane-polarized light and is mostly fresh except for narrow magnetite alteration rims in places (Fig. 7a). Cr-spinel is characterized by Mg# and Cr# [Cr/(Cr+Al)] ranging between 0.38 to 0.43 and 0.62 to 0.64, respectively (Table S1). The main primary sulfide phases are pentlandite ± chalcopyrite that occur as disseminated grains that are locally altered to minor native copper, awaruite, heazlewoodite and magnetite (Fig. 7b). Stockwork magnesite veins hosted by partially serpentinized harzburgite display cryptocrystalline and/or botryoidal textures cemented by sparry crystalline dolomite (Fig. 6p).

Serpentinites

Serpentinites are medium- to coarse-grained with ubiquitous lizardite ± chrysotile and/or antigorite but lack relicts of primary olivine or pyroxenes (except small relicts of enstatite in sample H2-43). Depending on

serpentine polymorph abundances and carbonate content, they are grouped as Lz-serpentinites or Atg-serpentinites. Fine-grained magnetite defines the rims of individual mesh cells in fully serpentinized samples (Fig. 6d).

Lz-serpentinite

Lz-serpentinite is commonly carbonate-poor (< 2 vol.% carbonate), with lizardite being the main serpentine phase and mesh-textured or forming lizardite-bastite pseudomorph after orthopyroxene. Minor antigorite occurs in Lz-serpentinite replacing either clinochlore (Cr-bearing chlorite based on SEM data) around Cr-spinels or lizardite along interconnecting mesh rims (Fig. 6d), in parts with traces of magnesite (Fig. 6e). Late chrysotile veins are common crosscutting other serpentine phases. Lizardite in Lz-serpentinite (H2-2) has compositions with 0.2 wt.% NiO, 40.2 wt.% SiO_2, and 0.58 wt.% Al_2O_3 and Mg# of 0.94 whereas antigorite has comparable NiO (0.18 wt.%), higher SiO_2 (40.2 wt.%) and lower Al_2O_3 (0.07 wt.%), with Mg# of 0.95 (Table 4). Bastite has comparable NiO (0.18 wt.%), lower SiO_2 (37.8 wt.%) and higher Al_2O_3 (0.7 wt.%), with lower Mg# of 0.91 compared to other serpentine phases in Lz-serpentinites. Cr-spinel in the Lz-serpentinite is not zoned and in parts is altered to porous Cr-spinel and/or magnetite along grain margins. Sulfide phases are similar to those in partially serpentinized harzburgite with lower abundances and the appearance of millerite replacing previous sulfide phases.

Atg-serpentinite

Antigorite is the main serpentine phase in Atg-serpentinite and is commonly observed with interpenetrating texture, replacing lizardite in the mesh center/matrix or lizardite-bastite pseudomorphs (Fig. 6f). Atg-serpentinites are variably carbonated (10-60 vol.% carbonate; also referred to as ophicarbonate). Atg-serpentinites can also contain talc which occurs together with magnesite producing the antigorite + talc + magnesite (Atg-Tlc-Mgs) assemblage (Fig. 6g, h). Antigorite in Atg-serpentinite (i.e. H1-11 with no lizardite/bastite relicts) has 0.2 wt.% NiO, 42.8 wt.% SiO_2, 0.07 wt.% Al_2O_3 and Mg# of 96 (Table 4). Cr-spinel in

298 the Atg-serpentinite shows compositional zoning with optically intact cores that are altered to Cr-magnetite
299 through a narrow ferritchromite transition rim (Fig. 7c). Hematite is often present occurring on either mesh rim
300 or Cr-magnetite outer rim (Fig. 6 g, 7c). Compared to partially serpentinized harzburgite and Lz-serpentinite,
301 sulfide phase are dominated by disseminated millerite with traces pentlandite, chalcopyrite, and heazlewoodite
302 with hydrous nickel-sulfides such as garnierite (Fig. 7d). Magnesite coexisting with antigorite contains 44 wt.%
303 MgO and is low in Fe (X_{FeCO3} = 0.02) with some Si-impurities (0.47 wt.% SiO_2). Dolomite composition has
304 comparable Ca (X_{CaCO3}= 0.51) and Mg (X_{MgCO3} = 0.48), and is Fe-poor (X_{FeCO3} = 0.003) (Table 4).

305 Listvenites

306 Listvenites are generally fine- to medium-grained and composed of Mg-Fe-Ca carbonates and silica with minor
307 sulfides, relict Cr-spinel and trace fuchsite (Cr-muscovite). Other accessory minerals include relict serpentine ±
308 talc ± rutile. SEM-EDS and Raman spectrometry measurements indicate that magnesite and to a lesser extent
309 dolomite (with traces siderite, ankerite and calcite) are the present carbonate minerals in listvenites with
310 magnesite having elevated Iron contents. There is greater abundances of dolomite-quartz veins in listvenites
311 spatially associated with shear zones. Based on microscopic observations and the modal proportion of quartz
312 and carbonate, three types of listvenite lithologies are classified and described below.

313 *Silica carbonate listvenite*

314 These rocks are consist of silica and carbonate (~50 ± 10 vol.% for quartz and total carbonate). Silica is mainly
315 quartz and carbonate is dominated by magnesite with minor dolomite. Traces of K-bearing minerals including
316 fuchsite (H2-34, H2-38) and jarosite (H1-21), have been identified in silica-carbonate listvenites, with the latter
317 being a weathering product. Fuchsite occurs as fine/wispy green veinlets or flakes within magnesite (Fig. 6i) or
318 replacing Cr-spinel relicts. The pseudomorphic mesh texture of the harzburgite protoliths is preserved in some
319 silica-carbonate listvenites but is obliterated in fault zone samples and is not present in listvenites formed after
320 talc (Fig. 6j). Mesh textured listvenite (mesh size < 0.5 mm) shows progressive replacement of residual

serpentine by carbonate (Fig. 6k, l). Carbonate core is a single magnesite crystal; in parts with quartz and the rim is consist of a mixture of magnesite, quartz and dolomite.

Carbonate listvenite

Carbonate listvenites are composed of mainly carbonate (total carbonate > 85 vol.%) and minor quartz. Carbonate is dominated by magnesite except for one sample (H2-37) with higher modal dolomite. In foliated types, dolomite is usually coarser-grained forming late veins crosscutting finer-grained magnesite in the matrix (Fig. 6n). No fuchsite has been observed in this type of listvenite.

Silica listvenite

Silica listvenites display the opposite mineral modes compared to carbonate listvenite with abundant quartz (> 85 vol.%) and minor carbonate. Quartz is either cryptocrystalline or amorphous and occurs as groundmass that is locally crosscut by second generation polycrystalline quartz. Fuchsite occurs only in one sample (H2-14). These rocks are very porous and brecciated, but in cases, a mesh texture is still recognizable due to alignments of secondary porosity that define the former mesh cells (Fig. 6o). The porosity most likely reflects carbonate dissolution along mesh rims.

Listvenitization formed concomitant with new sulfide assemblages (Fig. 7e-h) that are rare in carbonate listvenites but more abundant in silica and silica-carbonate listvenites (i.e., C-0 to C-3, H1-21 and H1-22). They include pyrite-bravoite (Ni-bearing pyrite) solid-solution, violarite, minor garnierite, with traces of millerite, cinnabar and barite. Pyrite-bravoite is the most abundant sulfide mineral that occurs as fracture-filling, enclosing relict Cr-spinel or disseminated grains, more commonly observed in association with brecciated samples (Fig. 7e-g). Some sulfides and Fe-bearing minerals are altered to garnierite, hematite, goethite, violarite, limonite, malachite and covellite as a result of surficial (supergene) weathering (Fig. 7h).

5.2. Bulk-rock geochemistry

The bulk-rock compositions of partially serpentinized harzburgite, serpentinite and listvenite are given in Table 2. In the reporting and discussion of the geochemical data, the Atg-Tlc-Mgs rock (also referred to talc-bearing Atg-serpentinite) has been grouped with Atg-serpentinite samples.

5.2.1. Major oxides

Partially serpentinized harzburgites and serpentinites show comparable compositions and plot close to the middle of MgO+CaO-SiO_2 tie-line on a MgO+CaO-SiO_2-LOI ternary diagram (Fig. 8a). Partially serpentinized harzburgites contain 37.2-39.0 wt.% MgO, 39.1-40.4 wt.% SiO_2, 6.9 to 8.4 wt.% Fe_2O_3, and 8.1-14.2 wt.% LOI, similar to the composition of Neotethyan mantle peridotites in the region (e.g., Delavari et al., 2009; Saccani et al., 2010; Hanghøj et al., 2010). Concentrations of other major elements are low (< 1.4 wt.%). Lz- and Atg-serpentinite compositions overlap and compared to harzburgite protolith (Fig. 8a) show slightly wider ranges of major elements with 34.2-38.2 wt.% MgO, 34.7-41.2 wt.% SiO_2, 7.5-10.2 wt.% Fe_2O_3 and 12.5-19.3 wt.% LOI. Concentrations of other major elements are generally low (< 1.1 wt.%, except for H1-11 with 3.8 wt.% CaO).

On a MgO+CaO-SiO_2-LOI ternary diagram, listvenites can be distinguished from partially serpentinized harzburgites and serpentinites by showing higher compositional variability, making three fields mainly controlled by variable (Mg+Ca)/Si and wide range of LOI (Fig. 8a). Carbonate listvenites have slightly higher (Mg+Ca)/Si compared to their harzburgite protolith and have higher LOI. They have 16.9-35.2 wt.% MgO, 18.7-28.6 wt.% SiO_2, 2.6-6.8 wt.% Fe_2O_3, a wide range of CaO from 0.1 to 22.8 wt.% and 28.2-37.3 wt.% LOI. In contrast, silica listvenites are characterized by very low (Mg+Ca)/Si and LOI, clustering towards the SiO_2 corner. They contain 0.1-6.5 wt.% MgO, 64.4-96.1 wt.% SiO_2, 1.04-7.9 wt.% Fe_2O_3, 0.05-7.8 wt.% CaO and 2.0-14.1 wt.% LOI. Silica-carbonate listvenites show slightly lower (Mg+Ca)/Si compared to their harzburgite protolith and plot as a distinct group between the field of silica and carbonate listvenites. They contain 18.1-24.2 wt.% MgO, 35.8-48.1 wt.% SiO_2, 3.2 to 7.5 wt.% Fe_2O_3, 1.0-6.8 wt.% CaO and 20.8-28.3 wt.% LOI. Abundances of other major elements for all listvenite lithologies are < 1 wt.% (except for (C-3) and (H1-18) with 2.8 and 7.2 wt.% Al_2O_3, respectively).

Higher LOI in carbonate and silica-carbonate listvenites together with high MgO, is consistent with the presence of magnesite as the most abundant carbonate mineral in the listvenites, following by minor dolomite in samples with elevated Ca, in a good agreement with microscopic observations.

The variability of MgO and SiO_2 contents which was low in partially serpentinized harzburgites and serpentinites is much greater in different listvenite lithologies with biggest changes in silica listvenites (Fig. 8b). Accordingly, Mg contents and Mg# variations in the carbonate and silica-carbonate listvenites show less variability than Si, and are roughly in the range of Hangaran partially serpentinized harzburgites and serpentinites (Fig. 8c-d).

5.2.2. Trace elements

The ultramafic rocks (harzburgites and serpentinites) show high concentrations of Co, Cr, Ni and Sc (Table 2), and the high concentrations of these elements in listvenite lithologies confirm their ultramafic protolith. To facilitate comparison, trace element and REE concentrations have been normalized to primitive mantle (PM) compositions (Fig. 9). PM-normalized patterns show discernable enrichments (~ 5 to ~100x PM) in As, Cs, Mo, Li, Sb and W in partially serpentinized harzburgite and Lz- and Atg-serpentinites, whereas other trace element abundances are in the range of, or lower than PM values (Fig. 9a). Listvenite lithologies show higher PM-normalized abundances (~ 5 to > 1000x PM) for a larger number of trace elements including As, Ba, Cs, Li, Mo, Pb, Rb, S, Sb, Sr, U and W compared to harzburgite protolith (Fig. 9a, b). Gold and copper abundances in Lz- Atg-serpentinites and listvenite lithologies are within the range of harzburgite. PM-normalized REE patterns of partially serpentinized harzburgite and Lz-serpentinite are similar and show depleted LREE patterns compared to Atg-serpentinite with elevated LREE and a positive Eu anomaly (Fig. 9c). In contrast, listvenites show flat REE patterns with higher LREE abundances compared to harzburgite protolith and a positive Eu anomaly in carbonate listvenite (Fig. 9c, d).

5.3. Isotope data

389 The $\delta^{13}C_{(VPDB)}$, $\delta^{18}O_{(VSMOV)}$ and radiogenic Sr isotopic compositions of carbonate from thirty-three samples
390 (partially serpentinized harzburgites, serpentinites, listvenites, carbonate veins and limestones) and $\delta^{34}S_{(VCDT)}$
391 isotopic values of sulfide separates from three sulfide-rich listvenites together with Rb and Sr concentrations for
392 nine carbonate leaches are listed in Table 3 and shown in Figure 10. The $^{87}Sr/^{86}Sr$ values have been corrected for
393 ~59 million years of radiogenic growth, consistent with the proposed collisional age (Delavari et al., 2014). Fields
394 for other carbonated ophiolites and associated carbonate veins are also shown for comparison.

395 5.3.1. Carbon, oxygen and sulfur isotopes

396 Partially serpentinized harzburgite and serpentinite have relatively homogenous $\delta^{13}C$ values (except for the H1-
397 11 serpentinite sample with -1.8 ‰) that range between -8.3 to -5.9 ‰ (Fig. 10a, b). Among the carbonate
398 rocks, two extreme $\delta^{13}C$ values belong to cryptocrystalline magnesites with the lightest range of ~-11.9 to -8.7
399 ‰ and pelagic limestones with the heaviest range of +1.9 to +2.4 ‰. The three micro-drilled dolomite veins
400 from core samples (C-0v, C-1v, C-3v) also show relatively homogenous $\delta^{13}C$ from -6.9 to -5.6 ‰ that are similar
401 to $\delta^{13}C$ values in the harzburgite and serpentinites, but lighter than their host listvenite core samples that range
402 between -0.1 to +2.8 ‰ (C-0b, C-1b, C-3b). The range of $\delta^{13}C$ values in listvenite samples collected at the surface
403 is more heterogeneous, with values ranging from -8.5 to +2.5 ‰, which is comparable with dolomite veins from
404 outcrops (average = -0.5 ± 1.7 ‰) but generally heavier than partially serpentinized harzburgite and
405 serpentinite. $\delta^{13}C$ distribution in listvenite lithologies is shown in figure 10c.

406 Partially serpentinized harzburgites have the lowest $\delta^{18}O$ values, between +12.2 and +12.7 ‰, followed by
407 serpentinite with slight heavier range of +14.8 to +15.3 ‰. The $\delta^{18}O$ values of carbonate in both of these
408 lithologies are significantly heavier than MORB mantle (5.5 ± 0.2 ‰, Eiler, 2001) and mantle peridotite (+5.5 ‰,
409 Mattey et al., 1994). The $\delta^{18}O$ isotopic composition of carbonate in listvenites and dolomite veins are even
410 heavier (+17 to +25.6 ‰) than carbonate in partially serpentinized harzburgite and serpentinites but lower than

411 pelagic limestone values (+25.2 to +25.9 ‰). The $\delta^{34}S$ of a pyrite-rich vein in two listvenite and one silica
412 listvenite samples range between +0.3 to +6.7 ‰ (Fig. 10e).

413 5.3.2. Sr isotopes

414 Sr contents in all but two of the analyzed samples are low (3-23 ppm), which makes the original isotopic
415 compositions susceptible to alteration. However, $^{87}Rb/^{86}Sr$ are invariably low (< 0.17) so corrections for 59 Ma of
416 radiogenic growth is in all cases < 0.00025, which is small compared to the observed range of initial $^{87}Sr/^{86}Sr$.
417 Initial $^{87}Sr/^{86}Sr$ in the serpentinite and four listvenite core samples are comparable, ranging from 0.7062 to
418 0.7072; this consistency provides some confidence that the Sr isotopic compositions of these samples are not
419 strongly affected by recent meteoric alteration. Among the other samples, the initial $^{87}Sr/^{86}Sr$ in cryptocrystalline
420 magnesite (0.7079) is similar to pelagic limestone (0.7078) and comparable with Cretaceous seawater (i.e.,
421 0.70722 to 0.70783, Ogg et al., 2012). With these considerations in mind, the $^{87}Sr/^{86}Sr$ in ultramafic rocks and
422 listvenites are greatly elevated compared to most mantle-derived igneous rocks including MORB (Fig. 10b).

423

424 **6. Discussion**

425 6.1. Unravelling the transformation of harzburgite to listvenite

426 Based on petrographic observations and mineral assemblages, two main episodes of alteration can be
427 elucidated for the transformation of harzburgite to listvenite: 1) Lz-serpentinization and 2) carbonation including
428 serpentine phase transition.

429 6.1.1. First episode: lizardite/chrysotile serpentinization

430 Petrographic observations indicate that the first episode of harzburgite alteration is characterized by hydration
431 of olivine and pyroxene to produce mesh textured lizardite-brucite and bastite (Fig. 6a, b) according to simplified
432 reaction R1:

433 $4\ (Mg)_2SiO_4 + CaMgSi_2O_6 + 7\ H_2O = 3\ Mg_3Si_2O_5(OH)_4 + Ca^{2+}_{(aq)} + 2\ HO^-_{(aq)}$ (R1).

434 (olivine) (clinopyroxene) (lizardite-bastite)

435 However, during the onset of serpentinization, little or no magnetite formed in low serpentinized domains (Fig.
436 6b), similar to other serpentinized peridotites (Bach et al., 2006; Frost and Beard, 2007). A comparison between
437 the chemical compositions of the primary olivine and pyroxenes in Hangaran harzburgites and the associated
438 hydration reaction products indicates the produced hydrated phases have high Fe contents (Table 4). These
439 observations suggest that during the initial serpentinization, iron partitions from olivine and pyroxene into
440 lizardite and brucite having Fe-rich nature, according to simplified reactions R2:

441 $2\ Fe_2SiO_4 + 3\ H_2O = Fe_3Si_2O_5(OH)_4 + Fe(OH)_2$ (R2).

442 (in olivine) (Fe-lizardite) (Fe-brucite)

443 Magnetite formation is accompanied by release of iron from early-formed phases such as Fe-serpentine or Fe-
444 brucite (R2) (Frost and Beard, 2007; Klein et al., 2009; Frost et al., 2013):

445 $9\ Fe(OH)_2 + 4SiO_{2(aq)} = 2\ Fe_3Si_2O_5(OH)_4 + Fe_3O_4 + 4\ H_2O + H_2$ (R3).

446 (Fe-brucite) (Fe-serpentine) (magnetite)

447 Partial oxidation of Fe^{2+} from dissolution of olivine/pyroxene or secondary Fe-brucite/Fe-serpentine phases to
448 form magnetite and H_2 (e.g., R3) causes strongly reducing condition during serpentinization allowing for the
449 formation of sulfur-poor assemblages characterized by heazlewoodite, native copper and Fe-Ni alloys (awaruite)
450 (Eckstrand, 1975; Lorand, 1987; Klein and Bach, 2009). Textural relationship of sulfide assemblages in partially
451 serpentinized harzburgites suggests that pentlandite and chalcopyrite desulfurized to native copper + awaruite +
452 magnetite due to interaction of highly reducing fluid with low sulfur fugacity (Fig. 7b). Partitioning of iron into
453 magnetite favors formation of Mg-rich serpentine which is documented in late lizardite veins (Mg# = 0.96)
454 compared to early-formed serpentine phases (Mg# = 0.92) (Table 4). The presence of Fe-rich serpentine (Klein et

al., 2009, 2014), and direct olivine replacement by lizardite and brucite (O'Hanely, 1996) indicate low-T (< 200 °C) for the initial serpentinization of Hangaran harzburgite.

6.1.2. Second episode: carbonation

The carbonation episode of the Hangaran ultramafic protolith can be further summarized over three alteration stages with distinct mineral assemblages: a) coeval lizardite/chrysotile-antigorite transition and carbonation, b) formation of talc-bearing Atg-serpentinite (Atg-Tlc-Mgs assemblage) and c) a final quartz-carbonate assemblage (listvenite).

Lizardite/chrysotile-antigorite phase transition and carbonation

Textural relationships in Hangaran ophiolites suggest that antigorite mainly formed after lizardite/chrysotile during carbonation stage with minor amounts forming after clinochlore or fine-grained mesh textured lizardite along mesh rim in carbonate-poor Lz-serpentinite (Fig. 6d). However, CO_2-bearing fluid may have reached partially serpentinized harzburgite through fractures and initiated carbonation as evidenced by the appearance of antigorite and magnesite in proximal veins, but no direct carbonation of olivine has been observed (Fig. 6c). Antigorite is dominantly observed overprinting lizardite/bastite pseudomorphs in fully serpentinized samples during carbonation stage attested by co-precipitation of antigorite and magnesite (Fig. 6e), where conversion of almost all lizardite occurred in carbonated Atg-serpentinite (Fig. 6f). Therefore, the onset of the carbonation stage occurred when infiltration of CO_2-rich fluids destabilized lizardite/chrysotile to form antigorite and magnesite according to following reaction:

$$17\ (Mg, Fe)_3Si_2O_5(OH)_4 + 3\ CO_2 = (Mg, Fe)_{48}Si_{34}O_{85}(OH)_{62} + 3\ Mg(Fe)CO_3 + 3\ H_2O \quad \text{(R4)}.$$

(lizardite/chrysotile) (antigorite) ((Fe-) magnesite)

Phase relations indicate that coexisting lizardite is the dominant serpentine phase at T < 300 °C (Evans, 2004; Schwartz et al., 2013). Lizardite destabilizes at higher temperatures and thermodynamic modelling suggests that

the lizardite to antigorite phase transition occurs between ~280-350 °C during sub-greenschist facies (Evans, 2004) or between 320-390 °C during blueschist facies metamorphism (Evans, 2004; Schwartz et al., 2013). The maximum temperature of 280 °C recorded from the quartz veins microthermometry (Monazzami Bagherzadeh et al., 2013) in the Hangaran listvenites supports the suggestion that the lizardite-antigorite transition occurs upon reaching sub-greenschist facies conditions where coeval antigorite and carbonate formation is documented by microscopic observations (Fig. 6c, f). Contemporaneous lizardite-antigorite phase transition and carbonation has been reported from other carbonated ophiolites and listvenites elsewhere (Groves et al., 1974; Boskabadi et al., 2017; Menzel et al., 2018).

The alteration of clinopyroxene from (R1) produces in excess $Ca^{2+}_{(aq)}$ that can react with CO_2 to form calcite or dolomite, most likely at the end of serpentinization process when low ratio of Mg/Ca is attained due to vanishing serpentine phases:

$$Ca^{2+}_{(aq)} + CO_{2(aq\ or\ gas)} + 2\ (OH)^-_{(aq)} \pm (Mg^{2+}) = CaCO_3 + H_2O \pm [CaMg(CO_3)_2] \qquad (R5).$$

(calcite) (dolomite)

Carbonation is actually a coupled carbonation-dehydration reaction that is involved with higher oxygen fugacity (i.e. H_2O loss and CO_2 gain and hence oxygen) towards the carbonation front if compared to the redox condition during initial serpentinization step that further supported by the appearance of hematite on the outermost relict Cr-spinel grain (Fig. 7c). Following oxygen, sulfur fugacity also increases in the carbonation front as shown by the replacement of the former sulfur-poor assemblage such as heazlewoodite and awaruite in the partially serpentinized harzburgite and Lz-serpentinite, by new sulfur-rich sulfides such as millerite (Fig. 7d), similar to other carbonated serpentinites (Eskstrand, 1975; Alt and Shanks, 1998).

Formation of talc-bearing Atg-serpentinite (Atg-Tlc-Mgs assemblage)

More infiltration of CO_2-rich fluids destabilizes antigorite to form talc and magnesite (Fig. 6g, h), buffering the $aSiO_2$ and aCO_2 of the fluid and making Atg-Tlc-Mgs rock according to the following reactions:

$Mg_{48}Si_{34}O_{85}(OH)_{62} + 48CO_{2(aq)} = 48\ MgCO_3 + 34\ SiO_{2(aq)} + 31\ H_2O$ (R6),

(antigorite) (magnesite)

and

$Mg_{48}Si_{34}O_{85}(OH)_{62} + 30\ SiO_{2(aq)} = 16\ Mg_3Si_4O_{10}(OH)_2 + 15\ H_2O$ (R7).

(antigorite) (talc)

Formation of listvenite

Reactions R6 and R7 suggest that $aSiO_{2(aq)}$ is not fully conserved due to the unbalanced buffering (i.e., less consumption by reaction R7), resulting in net gradual increase in the silica saturation by congruent antigorite dissolution. Thus, progressive influx of CO_2-rich fluids, could lead to quartz oversaturation and co-precipitation with magnesite via reaction (R6) that makes the first reaction path of listvenitization in Hangaran area. This is attested to by the static replacement of serpentine by magnesite + quartz (Fig. 6j, K) that further developed to entire replacement of the mesh cells upon complete dissolution of the serpentine (Fig. 6l). Similar mesh center carbonation has been observed in other ophiolites, where relict olivine or serpentine is replaced by carbonate (Lafay et al., 2017; Noël et al., 2018; Menzel et al., 2018), however, direct replacement of olivine is not observed in Hangaran ophiolite. The coexistence of serpentine and quartz (e.g. Fig. 6j, k) is uncommon in nature and has been reported from listvenite localities as well as weathered and silicified serpentinites elsewhere (Tsikouras et al., 2006; Boschi et al., 2009; Beinlich et al., 2010; Streit et al., 2012). Similar occurrences of antigorite + quartz (± talc ± carbonate) in the Wadi Mansah listvenite-serpentine transition zone in Oman ophiolite have been related to decreased X_{CO2} of the fluid at the margin of the listvenite zone at low temperatures (Falk and Kelemen, 2015).

A similar interpretation could explain the observed serpentine + quartz + carbonate assemblage in Hangaran (Fig. 6j, K) indicating low temperature carbonation.

The quartz pseudomorphs after talc coexisting with incipient magnesite in listvenite samples, as well as lack of mesh texture (Fig. 6m), suggest talc replacement by quartz + magnesite as the second reaction path for listvenitization in the Hangaran ophiolite according to reaction:

$$Mg_3Si_4O_{10}(OH)_2 + 3\ CO_{2(aq)} = 3\ MgCO_3 + 4\ SiO_{2(aq)} + H_2O \qquad \text{(R8)}.$$

(talc) (magnesite)

In the Hangaran area, talc-carbonate (also referred to as soapstone, e.g., Beinlich et al., 2012) as an intermediate product of ultramafic carbonation (Hansen et al., 2005) should usually occur between carbonated serpentinites and fully quartz-carbonate altered (listvenite) lithologies, but instead, this zone is demarcated by heavily weathered, bleached, soft lithology, making lower topographies in the field (Fig. 3a, e, f). This might be due to less resistance of talc-carbonate compare to other outcropping lithologies, making it prone to weathering and erosion. In outcrop, talc occurrence is mostly limited to talc-bearing Atg-serpentinite, similar to reported assemblage from the Wadi Mansah listvenite-serpentine transition zone in the Oman ophiolite (Falk and Kelemen, 2015). According to phase relationships in the $MgO\text{-}SiO_2\text{-}H_2O\text{-}CO_2$ system, Falk and Kelemen (2015) concluded that the stability of talc + magnesite without serpentine would occur over a small range of temperature and X_{CO2} that could be another reason for the absence of the talc-carbonate and the presence of talc-bearing Atg-serpentinite in the study area. In summary, the lack of talc-carbonate in the Hangaran area could be due to the complete conversion of talc to quartz + magnesite assemblage (R8), disequilibrium carbonation alteration, low temperature carbonation or intense weathering. The paucity of talc, however, seems to be a common feature of carbonated Cretaceous ophiolites in Iran, similar to other counterparts in the region (Ucurum, 2000; Akbulut et al., 2006; Aftabi and Zarrinkoub, 2013) in contrast to older carbonated Neoproterozoic ophiolites reported from northern parts of Arabian-Nubian Shield (e.g., Ali-Bik et al., 2012).

6.1.3. Listvenite variability

Occurrences of listvenite lithologies with variable abundances of quartz and carbonate, and Fe-Ni-O-S assemblages, in an outcrop down to meter scales imply significant physicochemical changes (e.g., pH, temperature, oxygen and sulfur fugacities, as well as $aSiO_2$ and aCO_2) in the circulating hydrothermal fluids occurred over short distances or multiple periods of infiltration of chemically distinct hydrothermal fluids. The solubility/precipitation of silica and magnesite require two contrasting physicochemical gradients of the hydrothermal fluid. Solubility of Si is enhanced by increasing temprature and pH (Fournier, 1985a, b; Rimstidt, 1997), and decreases in the hydrothermal fluids with elevated aCO_2 (Akinfiev and Diamond, 2009). Therefore, carbonate-dominated listvenite assemblages are likely formed from hotter, more alkaline fluids (pH > 9, Ucurum, 2000; Akbulut et al., 2006) with higher aCO_2, compared to silica-dominated listvenites where magnesite precipitation is hindered by Si-rich fluids (Klein and Garrido, 2011), lower temperature and lower pH (Boschi et al., 2009; Escayola et al., 2009). Abundant sulfur-rich sulfides such as pyrite-bravoite (Fig. 7e-g) in silica and to a minor extent in silica-carbonate listvenites attest to higher sulfur fugacity of the hydrothermal fluids forming these listvenites (Eckstrand, 1975; Frost, 1985) compared to sulfide-poor carbonate listvenites.

Based on field observations, silica listvenites are hosted by the other listvenite lithologies (Fig, 2, 3g), and their dominantly brecciated texture with ubiquitous multiple generations of late quartz and dolomite veins suggest formation from a long-lived hydrothermal system in tectonically active fault zones, most likely at low temperature (e.g., ≤ 200 °C; Klein and Garrido, 2011; Akbulut et al., 2006). Their porous textures (Fig. 4c, d, 6o) indicates magnesite dissolution upon influx of fluids with lower pH that is further supported by their distinctly lower Mg# compared to other listvenite lithologies (Fig. 8d). The abundant dolomite that occurs as late veins crosscutting other listvenite lithologies (Fig. 4a, b, f) is most likely due to lower Mg/Ca ratios in the fluid. This could be related to early magnesite precipitation in listvenite lithologies leading to lower Mg^{2+} supply and dominance of Ca^{2+} in the fluid enhancing dolomite precipitation by decreasing the stability field of magnesite (Franz, 1989; Boschi et al., 2009).

569 6.1.4. Formation of late cryptocrystalline vein magnesite

570 The temporal association between carbonated lithologies on topographic highs compared to stockwork
571 magnesite on topographic lows suggests magnesite remobilization by percolation of meteoric fluids draining the
572 outcrops through conduits and depositing pure magnesite in the fractures, perhaps during the final stages of
573 tectonic activity (Fig. 3b). Textural and SEM-EDS observations indicate that cryptocrystalline magnesite with
574 botryoidal texture is poor in iron and lacks relict Cr-spinel (Fig. 6p). The is similar to other cryptocrystalline
575 magnesites associated with ophiolites in Iran and elsewhere (e.g., Mirnejad et al., 2015; Oskierski et al., 2013)
576 that is formed by direct re-precipitation from Mg-rich fluids rather than mineral dissolution-precipitation
577 reactions.

578

579 6.2. Element Mobility

580 Although the external addition of CO_2 must be responsible for carbonation of ultramafic rocks and
581 listvenitization, there is still controversy regarding the modification of elemental compositions during
582 carbonation and listvenitization. Some workers suggest that these processes are approximately isochemical
583 (Griffis, 1972; Hansen et al., 2005; Kelemen et al., 2011; Falk and Kelemen, 2015; Hinsken et al., 2017) while
584 others regard it as a non-isochemical process (Buisson and Leblanc, 1985; Schandl and Naldrett, 1992; Ashley,
585 1997; Boschi et al., 2009). It is likely that some elements are derived locally, with transport paths ranging from
586 mm to m, whereas other elements are introduced with the fluid (and are derived distally, with transport paths
587 ranging from 100's of m to 10s of km).

588 In order to compare element mobilities during lizardite serpentinization and carbonation, volatile-free bulk-rock
589 compositions of two types of serpentinites and listvenite lithologies are compared to the average composition of
590 a harzburgite protolith to propose a "listvenite mobility sequence" (Fig. 11). Based on harzburgite-normalized
591 patterns, elements mobility are categorized into four levels: 1) immobile elements showing no discernable

mobility (variations < ±1 standard deviation of the average harzburgite), 2) slightly mobile (variations < 10x harzburgite), 3) moderately mobile (10x < harzburgite < 100x) and 4) strongly mobile (> 100x harzburgite). Here we follow the same structure as the previous section (6.1) and discuss the element mobilities during two episodes of a) lizardite serpentinization and b) carbonation.

6.2.1. Element mobility associated with lizardite serpentinization

Beyond the addition of water, lizardite serpentinization did not redistribute major elements much (Fig. 11a), except for Ca loss that is likely linked to breakdown of clinopyroxene from harzburgite (reaction R1). Harzburgite-normalized patterns of trace elements and REE in Lz-serpentinite broadly overlap the average composition of harzburgite (±1 S.D.), except for slight Mo, U and W gains, and Cs, Nb, and Zr loss. These variations may be inherited from partial serpentinization effect on the composition of harzburgite protolith leading to gain (e.g., Cs) or loss of these elements prior to full lizardite serpentinization. Other factors such as primary compositional heterogeneity of the harzburgite protolith, different hydration rate of olivine and pyroxenes, and nature of hydrating fluids cannot be excluded. Chemical compositions of olivine-pyroxene and newly formed lizardite-bastite indicate incompatible elements such as Cr, Ni and Al, as well as Mn redistributed by aqueous fluid during serpentinization at a mineral-scale with no discernable mobility on the bulk rock composition (Table 4).

PM-normalized trace element and REE patterns for partially serpentinized harzburgite and Lz-serpentinite show large (up to 50x PM) enrichment in Cs, and to a lesser extent Li, As, Sb and W with no Eu anomaly, similar to mantle wedge serpentinites (Deschamps et al., 2013; Peters et al., 2017), but lack Pb and Sr enrichments commonly observed in this type of serpentinite (Fig. 9a, b). Their bulk rock compositions based on alkali-U discrimination diagrams also point to mantle wedge serpentinization (Fig. 12). The observed enrichments suggest interactions of peridotite protolith with sediment-derived fluids (Kodolányi et al., 2012; Deschamps et al., 2013; Peters et al., 2017).

615 6.2.2. Element mobility associated with carbonation (including Lizardite-antigorite phase transition)

616 Atg-serpentinite and listvenites show greater variations in element mobility patterns with noticeable similarities
617 between Atg-serpentinite and carbonate listvenite, and between silica-carbonate and silica listvenites (Fig. 11).
618 Major elements show no discernable redistribution in Atg-serpentinite except for slight Ca enrichment, whereas
619 greater variations in element mobility is evidenced by higher abundances of Ca and K in all listvenite types with
620 distinct Si enrichment and strong Mg and Mn depletion in silica listvenites. Ca enrichment likely occurred by
621 either internal supply (reaction R1) and/or late external supply when lower Mg/Ca in the fluids favored
622 precipitation of Ca-Mg carbonate (e.g., reaction R5), as recorded by dolomite veins crosscutting listvenites (Fig.
623 4a, b, f). Mg and Si are possibly the most mobile major elements during peridotite carbonation with mobilization
624 attested by formation of carbonate and silica listvenite end-members and late dolomite/quartz veins. The
625 extremely low Mg# and Mg (also Mn) depletion in silica listvenite is most likely due to mobility of Mg as the Fe
626 content of this type of listvenites is comparable to that of silica-carbonate and carbonate listvenites (Fig. 8b-d).
627 This implies that the formation of silica listvenites involves release of Mg from carbonate and replacement by Si
628 due to influx of a later Si-rich fluid with lower pH. Mg and Si mobility is not very obvious in other types of
629 listvenites as these elements show similar concentrations to their harzburgite protolith, thus showing low
630 mobility on the harzburgite-normalized patterns in figure 11.

631 Except for silica listvenites, incompatible elements such as Co, Cr, Ni, Sc, and V, as well as Cu and Zn for all
632 serpentinite and listvenites are still within the range of harzburgite protolith and show no discernable mobility,
633 suggesting redistribution between antigorite and other coexisting phases (e.g., Cr-spinel, Fe-oxide, sulfide and
634 carbonate) at the mineral-scale. These elements show low concentrations in silica listvenites most likely either
635 due to breakdown of their host minerals (Cr-spinel, Ni-sulfide and/or carbonate), or to dilution by silicification.

636 A number of trace elements categorized with slight mobility in figure 11a such as Y, Sn, Rb, Mo and Li are also
637 within the range of harzburgite protolith in Atg-serpentinite but show progressive enrichments from carbonate,

638 to silica-carbonate and silica listvenites, respectively. Another suite of trace elements including Nb and Zr with
639 no discernable mobility in Atg-serpentinite indicate slight to moderate mobility in carbonate listvenite together
640 with Sr, Pb and Sr with a marked S depletion in both rock types. In contrast, silica-carbonate and silica listvenites
641 show moderate mobility with higher enrichments in these elements (except for Sr) and distinct S enrichment.
642 Another similarity in the mobility patterns is observed between Atg-serpentinite and carbonate listvenite for W,
643 As and Sb with comparably stronger enrichments in the latter with the highest U enrichment factor (up to 200x
644 harzburgite). In contrast, silica listvenite is characterized by the highest enrichment factor for W, As and Sb (up
645 to 250x, 2000x and 4000x harzburgite, respectively), followed by silica-carbonate listvenite.

646 Similar enrichment in elements such as Ca, Sr, Ba and Pb in Atg-serpentinite and carbonate listvenite is most
647 likely due to the effect of carbonation. Experimental investigations on carbonation of serpentinite under forearc
648 conditions demonstrates that magnesite may sequester these elements (Sieber et al., 2018), likely by interaction
649 with more CO_2-rich fluids released from subducting carbonate-bearing sediments undergoing dehydration in
650 forearc mantle. This is further supported by Cs/U, Li/U, and Rb/U relations in Hangaran lithologies, showing
651 modification of harzburgite protolith compositions towards the composition of global subducted sediment
652 (GLOSSII) through transient carbonated lithologies (Fig. 12).

653 Accordingly, general similarity of REE patterns between Atg-serpentinite and listvenites with moderate to strong
654 mobility, distinguished LREE/HREE enrichments, and marked positive Eu anomaly may further support
655 carbonation as the main cause of LREE/HREE fractionation in the carbonated rocks (Fig. 11b). LREE enrichments
656 are common in listvenites (Buisson and Leblanc, 1987; Tsikouras et al., 2006; Akbulut et al., 2006; Qiu and Zhu,
657 2018) and REE-carbonate complexes may be able to fractionate LREE/HREE in CO_2-rich fluids during
658 carbonation/listvenitization (e.g., Tsikouras et al., 2006 and references therein).

659 Chalcophile elements such as As, Mo, Sb and Sn as well as siderophile W correlate positively with S enrichments
660 in sulfide-rich listvenites (Fig. S2), suggesting these elements reside in sulfide phases. Higher abundances of As

661 and Sb in Atg-serpentinite and sulfide-poor carbonate listvenite with depleted S (Fig. 11a) may point to a
662 different host mineral such as antigorite during serpentine phase transition (e.g., Deschamps et al., 2011) and/or
663 magnesite in carbonate listvenite.

664 In summary, with the exception of K, CO_2, H_2O, and/or Ca, carbonation/listvenitization of harzburgite is
665 isochemical with respect to the major elements that are redistributed at a hand specimen to an outcrop scale.
666 However, with respect to many trace elements, carbonation is a non-isochemical process.

667 6.2.3. Lack of gold mineralization

668 Listvenites have been previously reported to contain economic concentrations of gold and precious metals
669 (Ashley, 1997; Tsikouras et al., 2006, Zoheir and Lehmann, 2011; Aftabi and Zarrinkoub, 2013; Qiu and Zhu,
670 2015; Belogub et al., 2017), while gold-poor listvenites are also common (e.g., Akbulut et al., 2006; Hinsken et
671 al., 2017). It is unclear whether gold enrichments were caused by listvenitization or by a later mineralization
672 event using the same fluid conduits overprinting the former listvenite. There is no evidence for gold enrichment
673 in the listvenite samples investigated in this study (Fig. 11a). Abundances of gold in Hangaran listvenites
674 (average = 1 ppb) are indistinguishable from harzburgite protolith and serpentinite, with an average of 1.2 ppb
675 (Table 2).

676

677 6.3. Sources of carbonating fluids and T constraints

678 A wide range of temperatures from 80-130 °C (Falk and Kelemen, 2015) up to 420 °C (Menzel et al., 2018) have
679 been reported for listvenitization of peridotite, with optimal carbonation temperatures of 150-250 °C for
680 serpentinite (Klein and Garrido, 2011). Limited fluid inclusion microthermometry from quartz veins within silica-
681 carbonate listvenites in the Hangaran area suggests hydrothermal fluid temperatures ranging from 110 to 280 °C
682 (Monazzami Bagherzadeh et al., 2013). The lack of metamorphic olivine and the occurrence of mesh-textured

683 listvenites and the prevalence of silica listvenites further supports moderate to low temperatures for most
684 Hangaran listvenites.

685 Stable isotope data (O, C, S) and to a lesser extent Sr isotopes have been used to constrain the sources of
686 carbonating fluids in listvenites worldwide (Auclair et al., 1993; Beinlich et al., 2012; Falk and Kelemen, 2015;
687 Boskabadi et al., 2017; Hinsken et al., 2017; Menzel et al., 2018). Four main sources of carbonating fluids have
688 been proposed: (I) seawater-derived fluids; (II) metamorphic fluids from devolatilization
689 (dehydration/decarbonation) reactions; (III) mantle-derived or magmatic fluids; and (IV) meteoric water. The C
690 and O isotopic compositions of the Hangaran listvenites partially overlap with the fields of Wadi Mansah
691 (Oman), Great Serpentinite Belt (Australia), Appalachians and Advocate (Canada) listvenites but are different
692 from ANS (Arabian-Nubian Shield, Egypt), Leka and Linnajavri (Norway), and Tinos (Greece) listvenites, talc-
693 carbonates and carbonated ophiolites (Fig. 10a). A positive correlation between $\delta^{13}C$ and $\delta^{18}O$ (especially at $\delta^{18}O$
694 > 15 ‰ and $\delta^{13}C$ > -10 ‰) trending towards sedimentary limestone compositions can be observed for the
695 listvenite lithologies and associated dolomite veins. The most likely explanation for this trend is mixing between
696 a sediment-derived fluid and the ultramafic host rock. Therefore, a simple two-component mixing diagram can
697 be produced by assuming two end-members being Cretaceous seawater and mantle composition to test this
698 hypothesis (Fig. 10b). The total organic carbon (TOC) of carbonated rocks is unconstrained, so we cannot exclude
699 a contribution of oxidized organic carbon in samples with low $\delta^{13}C$. The $\delta^{13}C$ values for Cretaceous pelagic
700 limestones (+1.9 to +2.4 ‰) are taken to approximate the composition of seawater and limestone at the time of
701 listvenite formation. Cretaceous seawater (and pelagic limestone proxy) are assumed to have the same Sr and C
702 isotopic compositions (i.e., $^{87}Sr/^{86}Sr$ ~ 0.7078, $\delta^{13}C$ ~ 0 ‰) but different Sr abundances (38 ppm Cretaceous
703 seawater is taken from Coogan, 2009; 860 ppm for limestone of this study). The isotopic and trace element
704 composition of the mantle is taken to be $\delta^{13}C$ ~ -5 ‰ (Deines, 2002), Sr ~ 20 ppm (McDonough and Sun, 1995)
705 and $^{87}Sr/^{86}Sr$ = ~ 0.703 (Allègre, 2008). Figure 10b shows that listvenitic lithologies cluster around $^{87}Sr/^{86}Sr_{(59Ma)}$ =
706 0.7067; $\delta^{13}C$ = -2.1 ‰ and are clearly dominated by the Cretaceous seawater endmember. The mixing model

707 indicates the carbonating fluid dominantly has the composition of Cretaceous seawater with either mixing with
708 10% fluid of a mantle composition or more likely, partial equilibration Cretaceous seawater with the ultramafic
709 rock. In contrast to Oman listvenites, Hangaran listvenites have age corrected Sr isotopic ratios within the range
710 of, or less than Cretaceous seawater, also comparable to the Tinos listvenites (Fig. 10d), supporting seawater-
711 derived fluid.

712 Field observations and experimental studies however, show that magnesite (the dominant carbonate phase in
713 listvenites) does not commonly form due to direct interaction between seawater and ultramafic rock on the
714 modern day seafloor (Grozeva et al., 2017 and references therein). Magnesite precipitation requires a fluid with
715 a higher Mg/Ca ratio than occurs in unmodified seawater as the presence of Ca impede pure Mg-carbonate
716 formation (Noël et al., 2018). Compositions of seawater trapped in sediment pores can be modified by
717 carbonate dissolution of the host sediments; particularly if they are carbonate bearing. An alternative fluid
718 source could be produced by low temperature mineral transformation/dehydration in the shallow parts of an
719 accretionary prism (e.g., smectite-illite and opal-quartz reactions, Moore and Vrolijk, 1992). These fluids may
720 then be expelled at shallow levels (<30 km) beneath a forearc, as a result of mechanical compaction (Bebout,
721 2013), and then can infiltrate through ultramafic rocks where a continuous source of Mg likely enhance
722 magnesite formation.

723 Assuming 8 km of Sefidabeh sediment (Tirrul et al., 1983), 1-2 km of the Neh and Ratuk Complexes and a 3-4 km
724 thick crustal sequence of Birjand-Nehbandan ophiolite overlying mantle peridotite, a combined depth of 12-14
725 km is estimated for listvenitization, corresponding to lithostatic pressure of 0.3 to 0.4 GPa. This is in accord with
726 a peak temperature of 280 °C determined by microthermometry from the Hangaran listvenite (Monazzami
727 Bagherzadeh et al., 2013). $\delta^{34}S$ of disseminated pyrite in the listvenite lithologies overlap that of Great
728 Serpentinite Belt (Ashley, 1997) and Barramiya (Zoheir and Lehmann, 2011) listvenites and does not point to a
729 specific source (Fig. 10e).

730 Summarizing, we therefore interpret the source of the carbonate-rich fluid that formed the Hangaran listvenites
731 as having been produced as pore fluid and structurally bound fluid released from subducted carbonate-bearing
732 metasediments/limestone in shallow parts of the accretionary prism.

733 The low $\delta^{13}C$ (~ -12 to -8.7 ‰) and high $\delta^{18}O$ (~ +19 to +23 ‰) values of cryptocrystalline magnesite are lower
734 than other Iranian ophiolite-hosted magnesites (Mirnejad et al., 2008, 2015) but are in the range of
735 cryptocrystalline magnesites worldwide (García del Real et al., 2016, Fig. 10a). These types of veins form in
736 fractures near the surface (see section 6.1.4) after ophiolite obduction. Their isotopic signatures point to
737 meteoric water and formation at low temperatures, while low $\delta^{13}C$ values suggest microbial activity.

738

739 6.4. Geodynamic setting of Hangaran carbonated ophiolite

740 In this section, we consider the geodynamic setting where the Hangaran peridotites formed and where
741 serpentinization/listvenitization occurred. Hangaran peridotite Cr-spinel has an average Cr# ~ 0.4 and sits
742 dominantly in the forearc peridotite field with a small overlap into the MORB field (Supplementary Table S1 and
743 Fig. S1a). This composition is comparable to the Cr-spinel from other Birjand and Nehbandan ophiolites in the
744 region (e.g., Moghadam and Stern, 2015), where the forearc affinity is further supported by the orthopyroxene
745 compositions of the partially serpentinized harzburgite (Table 4 and Supplementary Fig. S1b). Forearc mantle is
746 widely acknowledged to be partly serpentinized (Hyndman and Peacock, 2003), and this could be where lizardite
747 serpentinization occurred in the Late Cretaceous via sediment-derived fluids. However, we do not exclude the
748 possibility of lizardite serpentinization via seawater hydrothermal alteration in a MOR setting. Phase relations
749 indicate that lizardite is stable at sub-greenschist conditions (T ~ 200-300 °C, P < 0.4 kbar) where antigorite is
750 absent (Schwartz et al., 2013), consistent with formation in the shallow parts of the forearc mantle wedge.
751 Formation of antigorite probably occurred where more CO_2-bearing fluids interacted with lizardite serpentinite,
752 forming coexisting carbonate and Atg-serpentinite. The progressive and focused percolation of such CO_2- and

753 FME-rich fluids along tectonic contacts and thrust fault zones resulted in listvenitization beneath a forearc
754 during obduction and accretion onto continental crust during the Paleocene-Oligocene collision of the Lut and
755 Afghan blocks. This younger age limit is provided by the youngest adakitic intrusions (59 Ma) in the SsSZ region,
756 which are interpreted as having formed just before collision (Delavari et al., 2014).

757 In this interpretation, subducted carbonate-bearing, weakly metamorphosed sediments from the accretionary
758 complex (i.e., Neh and Ratuk) in the SsSZ were the main source of carbonating fluids that formed the Hangaran
759 listvenites. The interpretation is presented in figure 13 and is similar to that proposed for Wadi Mansah
760 listvenite in Oman (Falk and Kelemen, 2015), indicating important hydrothermal carbonation in the shallow
761 forearc when Neotethys was closing. The spatial association of listvenite with thrust faults (e.g., Menzel et al.,
762 2018) and suture zones (e.g., Buisson and Leblanc, 1985), as observed in the Hangaran listvenites have been also
763 reported worldwide.

764

765 **7. Conclusions**

766 Carbonated ultramafics, different listvenite types and late cryptocrystalline magnesite veins in the Hangaran
767 region of eastern Iran represent an important example of natural CO_2 sequestration via a sequence of
768 serpentinization and carbonation within a fossil sub-forearc system. The observed mineral assemblages indicate
769 that the formation of distinct listvenite types from mantle peridotite occurred through contemporaneous
770 carbonation and lizardite-antigorite transformation at sub-greenschist facies conditions (< 280 °C).
771 Listvenitization is spatially associated with fault zones and resulted in a spectrum of variably quartz-carbonate
772 altered assemblages and in turn, distinct metasomatic zones. Silica listvenite formed by low temperature
773 decarbonation in a long-lived evolving hydrothermal system circulating in fault zones. Stable and radiogenic
774 isotopic data point to a sedimentary source of the carbonate-rich fluid. The mineralogical and chemical changes
775 associated with serpentinite carbonation and listvenitization suggest nearly isochemical alteration for the major

elements (except K and/or Ca) but non-isochemical modification for most trace elements (i.e., FME, HFSE and LREE). Geochemical patterns further suggest CO_2-rich fluid mediated transfer of such trace elements from dehydration of subducted metasediments during the closure of the Neotethys and suturing the Lut-Afghan continental blocks in the Eocene-Oligocene. This carbonation indicates that the shallow part of the mantle wedge in suture zones is not just an important natural CO_2 sequestration factory but is also experiences significant mass transport.

Acknowledgments

AB is greatly indebted to his main Ph.D. supervisor Prof. Robert J Stern who provided insight and expertise but could not be listed as a co-author for geopolitical reasons. We acknowledge funding by the Swedish Research Council (Swedish Research Links programme 2014-25616-114501-15). We also thank Pär Hjelmquist at the Department of Environmental Science and Analytical Chemistry, Stockholm University, and Heike Siegmund and Curt Broman at the Department of Geological Sciences, Stockholm University, for the gold, stable isotope and Laser Raman analyses. We thank two anonymous reviewers for their insightful comments and suggestions that improved the manuscript. This is UTD Geosciences contribution number 1344.

8. References:

Aftabi, A., Zarrinkoub, M.H., 2013. Petrogeochemistry of listvenite association in metaophiolites of Sahlabad region, eastern Iran: Implications for possible epigenetic Cu-Au ore exploration in metaophiolites. Lithos 156–159, 186–203. https://doi.org/10.1016/j.lithos.2012.11.006

Akbulut, M., Piskin, O., Karayigit, A.I., 2006. The genesis of the carbonatized and silicified ultramafics known as

798 listvenites: a case study from the Mihalıccık region (Eskisehir), NW Turkey. Geological Journal 41, 557–580

799 Akinfiev, N.N., Diamond, L.W., 2009. A simple predictive model of quartz solubility in water-salt-CO_2 systems at
800 temperatures up to 1000°C and pressures up to 1000 MPa. Geochimica et Cosmochimica Acta 73, 1597–1608.
801 https://doi.org/10.1016/j.gca.2008.12.011

802 Ali-Bik, M.W., Taman, Z., El Kalioubi, B., Abdel Wahab, W., 2012. Serpentinite-hosted talc-magnesite deposits of
803 Wadi Barramiya area, Eastern Desert, Egypt: Characteristics, petrogenesis and evolution. Journal of African Earth
804 Sciences 64, 77–89. https://doi.org/10.1016/j.jafrearsci.2011.11.002

805 Allègre, C., 2008. Isotope Geology. Cambridge University Press, Cambridge. doi:10.1017/CBO9780511809323

806 Alt, J.C., Shanks, W.C., 1998. Sulfur in serpentinized oceanic peridotites: Serpentinization processes and
807 microbial sulfate reduction. Journal of Geophysical Research 103, 9917–9929.
808 https://doi.org/10.1029/98jb00576

809 Ashley, P.M., 1997. Silica-carbonate alteration zones and gold mineralisation in the Great Serpentinite Belt, New
810 England Orogen, New South Wales, in: Ashley, P.M., Flood, P.G. (Eds.), Tectonics and Metallogenesis of the New
811 England Orogen, Geological Society of Australia, Special Publication 19, pp. 212–225

812 Auclair, M., Gauthier, M., Trottier, J., Jebrak, M., Chartrand, F., 1993. Mineralogy, geochemistry, and paragenesis
813 of the Eastern Metals serpentinite-associated Ni-Cu-Zn deposit, Quebec Appalachians. Economic Geology 88,
814 123–138. https://doi.org/10.2113/gsecongeo.88.1.123

815 Bach, W., Paulick, H., Garrido, C.J., Ildefonse, B., Meurer, W.P., Humphris, S.E., 2006. Unraveling the sequence of
816 serpentinization reactions: Petrography, mineral chemistry, and petrophysics of serpentinites from MAR 15°N
817 (ODP Leg 209, Site 1274). Geophysical Research Letters 33, 4–7. https://doi.org/10.1029/2006GL025681

818 Bebout, G.E., 2013. Metasomatism in subduction zones of subducted oceanic slabs, mantle wedges, and the
819 slab-mantle interface, in: Harlov, D.E., Austrheim, H., (Eds.), Metasomatism and the Chemical Transformation of

820 Rock: The Role of Fluids in Terrestrial and Extraterrestrial Processes, Springer-Verlag, pp. 289–349

821 Beinlich, A., Austrheim, H., Glodny, J., Erambert, M., Andersen, T.B., 2010. CO_2 sequestration and extreme Mg
822 depletion in serpentinized peridotite clasts from the Devonian Solund basin, SW-Norway. Geochimica et
823 Cosmochimica Acta 74, 6935–6964. https://doi.org/10.1016/j.gca.2010.07.027

824 Beinlich, A., Plümper, O., Hövelmann, J., Austrheim, H., Jamtveit, B., 2012. Massive serpentinite carbonation at
825 Linnajavri, N-Norway. Terra Nova 24, 446–455. https://doi.org/10.1111/j.1365-121.2012.01083.x

826 Belogub, E. V., Melekestseva, I.Y., Novoselov, K.A., Zabotina, M. V., Tret'yakov, G.A., Zaykov, V. V., Yuminov,
827 A.M., 2017. Listvenite-related gold deposits of the South Urals (Russia): A review. Ore Geology Reveiws 85, 247–
828 270. https://doi.org/10.1016/j.oregeorev.2016.11.008

829 Bjerga, A., Konopásek, J., Pedersen, R.B., 2015. Talc-carbonate alteration of ultramafic rocks within the Leka
830 Ophiolite Complex, Central Norway. Lithos 227, 21–36. https://doi.org/10.1016/j.lithos.2015.03.016

831 Boschi, C., Dini, A., Dallai, L., Ruggieri, G., Gianelli, G., 2009. Enhanced CO_2-mineral sequestration by cyclic
832 hydraulic fracturing and Si-rich fluid infiltration into serpentinites at Malentrata (Tuscany, Italy). Chemical
833 Geology 265, 209–226. https://doi.org/10.1016/j.chemgeo.2009.03.016

834 Boskabadi, A., Pitcairn, I.K., Broman, C., Boyce, A., Teagle, D.A.H., Cooper, M.J., Azer, M.K., Stern, R.J., Mohamed,
835 F.H., Majka, J., 2017. Carbonate alteration of ophiolitic rocks in the Arabian–Nubian Shield of Egypt: sources and
836 compositions of the carbonating fluid and implications for the formation of Au deposits. International Geology
837 Reveiw 59, 391–419. https://doi.org/10.1080/00206814.2016.1227281

838 Brand, W.A., Coplen, T.B., Vogl, J., Rosner, M., Prohaska T., 2014. Assessment of international reference
839 materials for isotope-ratio analysis (IUPAC Technical Report). Pure and Applied Chemistry 86(3), 425–467

840 Bröcker, M., Fotoohi Rad, G., Burgess, R., Theunissen, S., Paderin, I., Rodionov, N., Salimi, Z., 2013. New age
841 constraints for the geodynamic evolution of the Sistan Suture Zone, eastern Iran. Lithos 170–171, 17–34.

842 https://doi.org/10.1016/j.lithos.2013.02.012

843 Buisson, G., Leblanc, M., 1987. Gold in mantle peridotites from Upper Proterozoic ophiolites in Arabia, Mali and
844 Morocco. Economic Geology 82, 2091–2097

845 Buisson, G., Leblanc, M., 1985. Gold in carbonatized ultramafic rocks from ophiolite complexes. Economic
846 Geology 80, 2028–2029. https://doi.org/10.2113/gsecongeo.80.7.2028

847 Camp, V.E., Griffis, R.J., 1982. Character, genesis and tectonic setting of igneous rocks in the Sistan suture zone,
848 eastern Iran. Lithos 15, 221–239. https://doi.org/10.1016/0024-4937(82)90014-7

849 Coogan, L.A., 2009. Altered oceanic crust as an inorganic record of paleoseawater Sr concentration.
850 Geochemistry, Geophysics, Geosystems 10. https://doi.org/10.1029/2008GC002341

851 Deines, P., 2002. The carbon isotope geochemistry of mantle xenoliths. Earth-Science Reviews 58, 247–278.
852 https://doi.org/10.1016/S0012-8252(02)00064-8

853 Delavari, M., Amini, S., Saccani, E., Beccaluva, L., 2009. Geochemistry and petrogenesis of mantle peridotites
854 from the Nehbandan Ophiolitic complex, Eastern Iran. Journal of Applied Sciences 9, 2671–2687.
855 https://doi.org/10.3923/jas.2009.2671.2687

856 Delavari, M., Amini, S., Schmitt, A.K., McKeegan, K.D., Mark Harrison, T., 2014. U-Pb geochronology and
857 geochemistry of Bibi-Maryam pluton, eastern Iran: Implication for the late stage of the tectonic evolution of the
858 Sistan Ocean. Lithos 200–201, 197–211. https://doi.org/10.1016/j.lithos.2014.04.015

859 Deschamps, F., Guillot, S., Godard, M., Andreani, M., Hattori, K., 2011. Serpentinites act as sponges for fluid-
860 mobile elements in abyssal and subduction zone environments. Terra Nova 23, 171–178.
861 https://doi.org/10.1111/j.1365-3121.2011.00995.x

862 Deschamps, F., Godard, M., Guillot, S., Hattori, K., 2013. Geochemistry of subduction zone serpentinites: a

review. Lithos 178, 96–127

Eckstrand, O.R., 1975. The dumont serpentinite: A model for control of nickel-iferous opaque mineral assemblages by alteration reactions in ultramafic rocks. Economic Geology 70, 183–201. https://doi.org/10.2113/gsecongeo.70.1.183

Eiler, J. M. (2001), Oxygen isotope variations of basaltic lavas and upper mantle rocks, in: Valley, J.W., Cole, D.R., Rosso, J.J. (Eds.), Stable Isotope Geochemistry. Reviews in Mineralogy and Geochemistry 43, pp. 319– 64

Escayola, M., Proenza, J.A., van Staal, C., Rogers, N., Skulski, T., 2009. The Point Rousse listvenites, Baie Verte, Newfoundland: altered ultramafic rocks with potential for gold mineralization. Current Research, Geological Survey Report 09-1, 1–12.

Evans, B.W., 2004. The serpentinite multisystem revisited: chrysotile is metastable. International Geology Review 46, 479–506. https://doi.org/10.2747/0020-6814.46.6.479

Falk, E.S., Kelemen, P.B., 2015. Geochemistry and petrology of listvenite in the Samail ophiolite, Sultanate of Oman: Complete carbonation of peridotite during ophiolite emplacement. Geochimica et Cosmochimica Acta 160, 70–90. https://doi.org/10.1016/j.gca.2015.03.014

Fournier, R.O., 1985a. The behavior of silica in hydrothermal solution, in: Berger, B.R., Bethke, P.M. (Eds.), Geology and Geochemistry of Epithermal Systems. Reviews in Economic Geology, vol. 2. Society of Economic Geologists, pp. 45–61

Fournier, R.O., 1985b. Carbonate transport and deposition in the epithermal environment, in: Berger, B.R., Bethke, P.M. (Eds.), Geology and Geochemistry of Epithermal Systems. Reviews in Economic Geology, vol. 2. Society of Economic Geologists, pp. 63–72

Franz, G., 1989. Stability of magnesite in carbonate–silicate assemblages: a review, in: Möller, P. (Eds.), Magnesite Geology, Mineralogy, Geochemistry, Formation of Mg-Carbonates. Gebr. Borntraeger

885 Verlagsbuchhandlung. Monograph Series on Mineral Deposits, vol. 28. Science Publishers, Stuttgart, pp. 259–
886 268

887 Frost, B.R., 1985. On the stability of sulfides, oxides, and native metals in serpentinite. Journal of Petrology 26,
888 31–63. https://doi.org/10.1093/petrology/26.1.31

889 Frost, B.R., Evans, K.A., Swapp, S.M., Beard, J.S., Mothersole, F.E., 2013. The process of serpentinization in dunite
890 from new caledonia. Lithos 178, 24–39. https://doi.org/10.1016/j.lithos.2013.02.002

891 Frost, R.B., Beard, J.S., 2007. On silica activity and serpentinization. Journal of Petrology 48, 1351–1368.
892 https://doi.org/10.1093/petrology/egm021

893 García del Real, P., Maher, K., Kluge, T., Bird, D.K., Brown, G.E., John, C.M., 2016. Clumped-isotope thermometry
894 of magnesium carbonates in ultramafic rocks. Geochimica et Cosmochimica Acta 193, 222–250.
895 https://doi.org/10.1016/j.gca.2016.08.003

896 Ghorbani, M., 2013. The Economic Geology of Iran. Springer, Dordrecht, Heidelberg, New York, London.
897 https://doi.org/10.1007/978-94-007-5625-0

898 Griffis, R., 1972. Genesis of a magnesite deposit, Deloro Twp., Ontario. Economic Geology 67, 63–71.
899 https://doi.org/10.2113/gsecongeo.67.1.63

900 Groves, D.I., Hudson, D.R., Hack, T.B.C., 1974. Modification of iron-nickel sulfides during serpentinization and
901 talc-carbonate alteration at Black Swan, Western Australia. Economic Geology 69, 1265–1281.
902 https://doi.org/10.2113/gsecongeo.69.8.1265

903 Grozeva, N.G., Klein, F., Seewald, J.S., Sylva, S.P., 2017. Experimental study of carbonate formation in oceanic
904 peridotite. Geochimica et Cosmochimica Acta 199, 264–286. https://doi.org/10.1016/j.gca.2016.10.052

905 Halls, C., Zhao, R., 1995. Listvenite and related rock-perspectives on terminology and mineralogy with reference

906 to an occurance at Cregganbaun, Co. Mayo, Republic of Ireland. Mineral Deposita 30, 303–313

907 Hanghøj, K., Kelemen, P.B., Hassler, D., Godard, M., 2010. Composition and genesis of depleted mantle
908 peridotites from the Wadi Tayin massif, Oman ophiolite; Major and trace element geochemistry, and Os isotope
909 and PGE systematics. Journal of Petrology 51, 201–227. https://doi.org/10.1093/petrology/egp077

910 Hansen, L.D., Dipple, G.M., Gordon, T.M., Kellett, D.A., 2005. Carbonated serpentinite (listwanite) at Atlin, British
911 Columbia: A geological analogue to carbon dioxide sequestration. The Canadian Mineralogist 43, 225–239.

912 Hinsken, T., Bröcker, M., Strauss, H., Bulle, F., 2017. Geochemical, isotopic and geochronological characterization
913 of listvenite from the Upper Unit on Tinos, Cyclades, Greece. Lithos 282–283, 281–297.
914 https://doi.org/10.1016/j.lithos.2017.02.019

915 Hoefs, J., 2015. Stable isotope geochemistry, seventh ed. Springer, Heidelberg, New York, Dordrecht, London

916 Hyndman, R.D., Peacock, S.M., 2003. Serpentinization of the forearc mantle. Earth and Planetary Science Letters
917 212, 417–432. https://doi.org/10.1016/S0012-821X(03)00263-2

918 Keith, M.L., Weber, J.N., 1964. Carbon and oxygen isotopic composition of selected limestones and fossils.
919 Geochimica et Cosmochimica Acta 28, 1787–1816. https://doi.org/10.1016/0016-7037(64)90022-5

920 Kelemen, P.B, Al Rajhi A., Godard, M., Ildefonse, B., Köpke, J., MacLeod, C., Manning, C., Michibayashi, K., Nasir,
921 S., Shock, E., Takazawa, E., Teagle, D., 2013. Scientific drilling and related research in the Samail Ophiolite,
922 Sultanate of Oman. Scientific Drilling 15, 64–71. DOI: 10.5194/sd-15-64-2013

923 Kelemen, P.B., Matter, J., 2008. In situ carbonation of peridotite for CO_2 storage. Proceeding National Academy
924 Sciences 105, 17295–17300. https://doi.org/10.1073/pnas.0805794105

925 Kelemen, P.B., Matter, J., Streit, E.E., Rudge, J.F., Curry, W.B., Blusztajn, J., 2011. Rates and mechanisms of
926 mineral carbonation in peridotite: Natural processes and recipes for enhanced, in situ CO_2 capture and storage.

927 Annual Reviews of Earth and Planetary Sciences 39, 545–576. https://doi.org/10.1146/annurev-earth-092010-
928 152509

929 Kelley, D.S., Karson, J.A., Früh-Green, G.L., Yoerger, D.R., Shank, T.M., Butterfield, D.A., Hayes, J.M., Schrenk,
930 M.O., Olson, E.J., Proskurowski, G., Jakuba, M., Bradley, A., Larson, B., Ludwig, K., Glickson, D., Buckman, K.,
931 Bradley, A.S., Brazelton, W.J., Roe, K., Elend, M.J., Delacour, A., Bernasconi, S.M., Lilley, M.D., Baross, J.A.,
932 Summons, R.E., Sylva, S.P., 2005. A serpentinite-hosted ecosystem: The Lost City hydrothermal field. Science
933 307, 1428–1434. https://doi.org/10.1126/science.1102556

934 Kim, S., Coplen, T.B., Horita, J., 2015. Normalization of stable isotope data for carbonate minerals:
935 Implementation of IUPAC guidelines. Geochimica et Cosmochimica Acta 158, 276–289.
936 https://doi.org/10.1016/j.gca.2015.02.011

937 Klein, F., Bach, W., 2009. Fe-Ni-Co-O-S phase relations in peridotite-seawater interactions. Journal of Petrology
938 50, 37–59. https://doi.org/10.1093/petrology/egn071

939 Klein, F., Bach, W., Humphris, S.E., Kahl, W.A., Jöns, N., Moskowitz, B., Berquó, T.S., 2014. Magnetite in seafloor
940 serpentinite-Some like it hot. Geology 42, 135–138. https://doi.org/10.1130/G35068.1

941 Klein, F., Bach, W., Jöns, N., McCollom, T., Moskowitz, B., Berquó, T., 2009. Iron partitioning and hydrogen
942 generation during serpentinization of abyssal peridotites from 15°N on the Mid-Atlantic Ridge. Geochimica et
943 Cosmochimica Acta 73, 6868–6893. https://doi.org/10.1016/j.gca.2009.08.021

944 Klein, F., Garrido, C.J., 2011. Thermodynamic constraints on mineral carbonation of serpentinized peridotite.
945 Lithos 126, 147–160. https://doi.org/10.1016/j.lithos.2011.07.020

946 Lackner, K.S., Wendt, C.H., Butt, D.P., Joyce, E.L., Sharp, D.H., 1995. Carbon dioxide disposal in carbonate
947 minerals. Energy 20, 1153–1170. https://doi.org/10.1016/0360-5442(95)00071-N

948 Kodolányi, J., Pettke, T., Spandler, C., Kamber, B.S., Gméling, K., 2012. Geochemistry of ocean floor and fore-arc
949 serpentinites: constraints on the ultramafic input to subduction zones. Journal of Petrology 53, 235–270.

950 Lafay, R., Baumgartner, P.L., Schwartz, S., Picazo, S., Montes-Hernandez, G., Vennemann, T., 2017. Petrologic
951 and stable isotopic studies of a fossil hydrothermal system in ultramafic environment (Chenaillet ophicalcites,
952 Western Alps, France): Processes of carbonate cementation. Lithos 294-295, 319–338

953 Li, H., 1991. Distribution patterns of the elements in the ocean: A synthesis. Geochimica et Cosmochimica Acta
954 55, 3223–3240. https://doi.org/10.1016/0016-7037(91)90485-N

955 Lorand, J.P., 1987. Cu–Fe–Ni–S mineral assemblages in upper-mantle peridotites from the Table Mountain and
956 Blow-Me-Down Mountain ophiolite massifs (Bay of Islands area, Newfoundland): their relationships with fluids
957 and silicate melts. Lithos 20, 59–76

958 Mattey, D., Lowry D., Macpherson, C., 1994. Oxygen-isotope composition of mantle peridotite. Earth and
959 Planetary Science Letters 128, 231–241. https://doi.org/10.1016/0012-821X(94)90147-3

960 McCollom, T.M., Bach, W., 2009. Thermodynamic constraints on hydrogen generation during serpentinization of
961 ultramafic rocks. Geochimica et Cosmochimica Acta 73, 856–875

962 McDonough, W.F., Sun, S.-S., 1995. The composition of the Earth. Chemical Geology 120, 223–253

963 Menegatti, A.P., Weissert, H., Brown, R.S., Tyson, R. V., Farrimond, P., 1998. High-resolution ^{13}C stratigraphy
964 through the early Aptian “Livello Selli” of the Alpine Tethys. Paleoceanography 13, 530–545

965 Menzel, M., Garrido, C.J., Sánchez-Vizcaíno, V.L., Marchesi, C., 2018. Carbonation of peridotite by CO_2-rich fluids:
966 Listvenite formation in the Advocate Ophiolite (Newfoundland, Canada). Lithos 323, 238–261

967 Mirnejad, H., Aminzadeh, M., Ebner, F., Unterweissacher, T., 2015. Geochemistry and origin of the ophiolite
968 hosted magnesite deposit at Derakht-Senjed, NE Iran. Mineralogy and Petrology 109, 693–704.

https://doi.org/10.1007/s00710-015-0408-0

Mirnejad, H., Ebrahimi-Nasrabadi, K., Lalonde, A.E., Taylor, B.E., 2008. Mineralogy, stable isotope geochemistry, and paragenesis of magnesite deposits from the ophiolite belt of Eastern Iran. Economic Geology 103, 1703–1713. https://doi.org/10.2113/gsecongeo.103.8.1703

Moghadam, H.S., Stern, R.J., 2015. Ophiolites of Iran: Keys to understanding the tectonic evolution of SW Asia: (II) Mesozoic ophiolites. Journal of Asian Earth Sciences 100, 31–59. https://doi.org/10.1016/j.jseaes.2014.12.016

Monazzami Bagherzadeh, R., Mirnejad, H., Eshback, P., Karimpour, M.H., 2013. Investigation of Au-Bearing listvenite using mineralogy, geochemistry, fluid inclusion and stable isotopes (oxygen, carbon and sulfur) in ophiolite- mélange zone of East Iran (Hangaran area, south Birjand). Scientific Quarterly Journal of Geosciences 22, 131–144. doi: 10.22071/gsj.2013.53687 (in Persian with English abstract)

Moore, J.C., Vrolijk, P., 1992. Fluids in accretionary prisms. Reviews of Geophysics 30, 113–135. https://doi.org/10.1029/92RG00201

Nasir, S., Al Sayigh, A.R., Al Harthy, A., Al-Khirbash, S., Al-Jaaidi, O., Musllam, A., Al-Mishwat, A., Al-Bu'saidi, S., 2007. Mineralogical and geochemical characterization of listwaenite from the Semail Ophiolite, Oman. Chemie der Erde 67, 213–228. https://doi.org/10.1016/j.chemer.2005.01.003

Noël, J., Godard, M., Oliot, E., Martinez, I., Williams, M., Boudier, F., Rodriguez, O., Chaduteau, C., Escario, S., Gouze, P., 2018. Evidence of polygenetic carbon trapping in the Oman Ophiolite: Petro-structural, geochemical, and carbon and oxygen isotope study of the Wadi Dima harzburgite-hosted carbonates (Wadi Tayin massif, Sultanate of Oman). Lithos 323, 218–237

Ogg, J.G., Hinnov, L.A., Huang, C., 2012. Cretaceous, in: Gradstein F.M., Ogg, J.G., Schmitz, M., Ogg, G.M. (Eds.), The Geologic Time Scale. Elsevier, pp. 793–853. https://doi.org/10.1016/B978-0-444-59425-9.00027-5

991 Okumura, T., Ohara, Y., Stern, R. J., Yamanaka, T., Onishi, Y., Watanabe, H., Chen, C., Bloomer S.H., Pujana, I.,
992 Sakai, S., Ishii, T., Takai, K., 2016. Brucite chimney formation and carbonate alteration at the Shinkai Seep Field, a
993 serpentinite-hosted vent system in the southern Marian forearc. Geochemistry, Geophysics, Geosystems 17,
994 3775–3796. https://doi.org/https://doi.org/10.1002/2016GC006449

995 O'Hanley, D. S., 1996. Serpentinites: Records of Tectonic and Petrological History, Oxford University Press, New
996 York

997 Oskierski, H.C., Bailey, J.G., Kennedy, E.M., Jacobsen, G., Ashley, P.M., Dlugogorski, B.Z., 2013. Formation of
998 weathering-derived magnesite deposits in the New England Orogen, New South Wales, Australia: Implications
999 from mineralogy, geochemistry and genesis of the Attunga magnesite deposit. Mineralium Deposita 48, 525–
1000 541. https://doi.org/10.1007/s00126-012-0440-5

1001 Palme, H., O'Neill, H. St. C., 2014. Cosmochemical estimates of mantle composition, in Holland H.D., Turekian,
1002 K.K. (Eds.), Treatise on Geochemistry (Second Edition), Elsevier-Pergamon, Oxford, pp. 1-39.
1003 https://doi.org/10.1016/B978-0-08-095975-7.00201-1

1004 Peters, D., Bretscher, A., John, T., Scambelluri, M., Pettke, T., 2017. Fluid-mobile elements in serpentinites:
1005 Constraints on serpentinisation environments and element cycling in subduction zones. Chemical Geology 466,
1006 654–666. https://doi.org/10.1016/j.chemgeo.2017.07.017

1007 Pitcairn, I.K., Warwick, P.E., Milton, J.A., Teagle, D.A.H., 2006. Method for ultra-low-level analysis of gold in
1008 rocks. Analytical Chemistry 78, 1290–1295. https://doi.org/10.1021/ac051861z

1009 Plank, T., 2014. The chemical composition of subducting sediments, in: Holland, H.D., Turekian, K.K. (Eds.),
1010 Treatise on Geochemistry (Second Edition), Elsevier-Pergamon, Oxford, pp. 607–629.
1011 http://dx.doi.org/10.1016/b978-0-08-095975-7.00319-3

1012 Qiu, T., Zhu, Y., 2018. Listwaenite in the Sartohay ophiolitic mélange (Xinjiang, China): A genetic model based on

1013 petrology, U-Pb chronology and trace element geochemistry. Lithos 302–303, 427–446.
1014 https://doi.org/10.1016/j.lithos.2018.01.029

1015 Qiu, T., Zhu, Y., 2015. Geology and geochemistry of listwaenite-related gold mineralization in the Sayi gold
1016 deposit, Xinjiang, NW China. Ore Geology Review 70, 61–79. https://doi.org/10.1016/j.oregeorev.2015.03.017

1017 Rimstidt, J.D., 1997. Gangue mineral transport and deposition, in: Barnes, H.L. (Eds.), Geochemistry of
1018 Hydrothermal Ore Deposits. John Wiley and Sons, New York, pp. 487–515

1019 Rose, G., 1837. Mineralogisch-geognostische Reise nach dem Ural, dem Altai and dem Kaspischen Meere, in
1020 Reimer G.E. (Eds.), Reise nach dem nördlichen Ural and dem Altai. Volume 1. Verlag der Sanderschen
1021 Buchhandlung, Berlin.

1022 Rosenbaum, J., Sheppard, S.M.F., 1986. An isotopic study of siderites, dolomites and ankerites at high
1023 temperatures. Geochimica et Cosmochimica Acta 50, 1147–1150

1024 Saccani, E., Delavari, M., Beccaluva, L., Amini, S., 2010. Petrological and geochemical constraints on the origin of
1025 the Nehbandan ophiolitic complex (eastern Iran): Implication for the evolution of the Sistan Ocean. Lithos 117,
1026 209–228. https://doi.org/10.1016/j.lithos.2010.02.016

1027 Sadeghian, M., Bouchez, J.L., Nédélec, A., Siqueira, R., Valizadeh, M. V., 2005. The granite pluton of Zahedan (SE
1028 Iran): A petrological and magnetic fabric study of a syntectonic sill emplaced in a transtensional setting. Journal
1029 of Asian Earth Sciences 25, 301–327. https://doi.org/10.1016/j.jseaes.2004.03.001

1030 Schandl, E.S., Naldrett, A.J., 1992. CO_2 metasomatism of serpentinites, south of Timmins, Ontario. The Canadian
1031 Mineralogist 30, 93–108

1032 Schwartz, S., Guillot, S., Reynard, B., Lafay, R., Debret, B., Nicollet, C., Lanari, P., Auzende, A.L., 2013. Pressure-
1033 temperature estimates of the lizardite/antigorite transition in high pressure serpentinites. Lithos 178, 197–210.
1034 https://doi.org/10.1016/j.lithos.2012.11.023

1035 Seifritz, W., 1990. CO_2 disposal by means of silicates. Nature 345, 486

1036 Sieber, M.J., Hermann, J., Yaxley, G.M., 2018. An experimental investigation of C–O–H fluid-driven carbonation
1037 of serpentinites under forearc conditions. Earth and Planetary Science Letters 496, 178–188.
1038 https://doi.org/10.1016/j.epsl.2018.05.027

1039 Streit, E., Kelemen, P., Eiler, J., 2012. Coexisting serpentine and quartz from carbonate-bearing serpentinized
1040 peridotite in the Samail Ophiolite, Oman. Contribution to Mineralogy and Petrology 164, 821–837.
1041 https://doi.org/10.1007/s00410-012-0775-z

1042 Taylor, H.P., Frechen, J., Degens, E.T., 1967. Oxygen and carbon isotope studies of carbonatites from the Laacher
1043 See District, West Germany and the Alnö District, Sweden. Geochimica et Cosmochimica Acta 31, 407–430

1044 Tirrul, R., Bell, I.R., Griffis, R.J., Camp, V.E., 1983. The Sistan suture zone of eastern Iran. Geological Society of
1045 America Bulletin 94, 134–150. https://doi.org/10.1130/0016-7606(1983)94<134:TSSZOE>2.0.CO;2

1046 Tsikouras, B., Karipi, S., Grammatikopoulos, T.A., Hatzipanagiotou, K., 2006. Listwaenite evolution in the
1047 ophiolite mélange of Iti Mountain (continental Central Greece). European Journal of Mineralogy 18, 243–255.
1048 https://doi.org/10.1127/0935-1221/2006/0018-0243

1049 Ucurum, A., 2000. Listwaenites in Turkey: perspectives on formation and precious metal concentration with
1050 reference to occurrences in east-central Anatolia. Ofioliti 25, 15–29

1051 Veizer, J., Ala, D., Azmy, K., Bruckschen, P., Buhl, D., Bruhn, F., Carden, G.A.F., Diener, A., Ebneth, S., Godderis, Y.,
1052 Jasper, T., Korte, C., Pawellek, F., Podlaha, O.G., Strauss, H., 1999. $^{87}Sr/^{86}Sr$, ^{13}C and ^{18}O evolution of Phanerozoic
1053 seawater. Chemical Geology 161, 59–88. https://doi.org/10.1016/S0009-2541(99)00081-9

1054 Verkouteren, R.M., Klinedinst, D.B., 2004. Value assignment and uncertainty estimation of selected light stable
1055 isotope reference materials: RMs 8543- 8545, RMs 8562-8564, and RM 8566. NIST Special Publication 260-149
1056 2004 ED.

1057 Zarrinkoub, M.H., Amini, S., Aftabi, A., Karimpour, M.H., 2005. Mineralogy , geochemistry , structural position
1058 and a genetic model for listvenite in east of Iran. Iranian Journal of Crystallography and Mineralogy 13, 363–378.
1059 (in Persian with English abstract)

1060 Zarrinkoub, M.H., Pang, K.N., Chung, S.L., Khatib, M.M., Mohammadi, S.S., Chiu, H.Y., Lee, H.Y., 2012. Zircon U-
1061 Pb age and geochemical constraints on the origin of the Birjand ophiolite, Sistan suture zone, eastern Iran. Lithos
1062 154, 392–405. https://doi.org/10.1016/j.lithos.2012.08.007

1063 Zedef, V., Russell, M.J., Fallick, A.E., Hall, A.J., 2000. Genesis of vein stockwork and sedimentary magnesite and
1064 hydromagnesite deposits in the ultramafic terranes of southwestern Turkey: A stable isotope study. Economic
1065 Geolology 95, 429–445. https://doi.org/10.2113/gsecongeo.95.2.429

1066 Zoheir, B., Lehmann, B., 2011. Listvenite-lode association at the Barramiya gold mine, Eastern Desert, Egypt. Ore
1067 Geolology Review 39, 101–115. https://doi.org/10.1016/j.oregeorev.2010.12.002

1068

1069 **Figure captions:**

1070 Fig. 1 (a) Simplified geological map showing the main ophiolitic belts in Iran and Oman (modified after
1071 Moghadam and Stern, 2015 and Nasir et al., 2007), (b) Geological map of the northern Sistan Suture Zone (SsSZ)
1072 indicating three main ophiolite occurrences including the Birjand ophiolite (modified after Tirrul et al., 1983).
1073 Red and black rectangles show approximate location of the Hangaran (this study), Sahlabad (Aftabi and
1074 Zarrinkoub, 2013), Sulabest (Bröcker et al., 2013) and Wadi Mansah (Falk and Kelemen, 2015) localities in
1075 eastern Iran and Oman. Abbreviations: Neh-Nehbandan, T.K.-Tchehel Kure, WNF-West Nehbandan fault, ENF-
1076 East Nehbandan fault.

1077

Fig. 2 Geological map of the Hangaran subareas (I) and (II) showing different lithologies and sample locations (modified after Monazzami Bagherzadeh et al., 2013). Locations of boreholes BH-1, BH-2, and BH-3 are also shown with stars. Inset shows relationships between areas (I) and (II) on a Google Earth image.

Fig. 3 Field photos showing (a) different ophiolitic outcrops in the Hangaran area (solid-line and dashed-line boxes show the locations of figures b, e and f. (b) Stockwork magnesite formed on the slope of partially serpentinized harzburgite in topographic lows along drainage channels (dashed box b in figure a). (c) Dark grey Lz-serpentinite. (d) Greenish grey Atg-serpentinite. (e) Contacts between serpentinite, partially serpentinized harzburgite and highly weathered zone (dashed box e in figure a). (f) Contact between highly weathered zone and listvenite on higher topographies (dashed box f in figure a). (g) Silica listvenites forming the highest topographies of the area hosted by silica-carbonate and carbonate listvenites. The location of the borehole (BH1 in figure 2), where core samples (i.e., C-0, C-1, C-2 and C-3) were collected, is also shown.

Fig. 4 Examples of different types of listvenites from surface and drillcore, showing crosscutting relationships. (a) A core sample of silica-carbonate listvenite from 59 m depth, cut by a dolomite vein (C-0). (b) An example of carbonate listvenite from surface that is cut by a dolomite vein (H2-37). (c) A core sample of silica listvenites from 64 m depth with sulfide and malachite mineralization and abundant secondary porosity (por) (C-2). (d) Silica listvenite sample from outcrop with very porous texture, reddish color and late quartz veins (H2-15). (e and f) Listvenites with foliated (H2-35) and brecciated textures (H2-40) are distinctive within the fault and shear zones. Abbreviations: Dol-dolomite, Mgs-magnesite, Qz-quartz, Hem-hematite, Por-porosity, Mlc-malachite.

Fig. 5 (a) Paragenetic sequences of Hangaran ophiolitic rocks evolved during the serpentinization and subsequent carbonate alteration. (b) Illustrations summarizing different mineral parageneses and textural evolutions during serpentinization and carbonate alteration in Hangaran. (*)-Atg-Tlc-Mgs rock. Abbreviations: Ol-olivine, Opx-orthpyroxene, P.S.-partially serpentinized, Ctl-chrysotile, Bst-bastite, Lz-lizardite, Atg-antigorite, Tlc-talc, Mag-magnetite, Mgs-magnesite, Crypto-cryptocrystalline and Qz-quartz.

Fig. 6 Photomicrograph and backscatter electron images (BSE) of textural evolution in variably carbonate-altered ophiolitic rocks in the Hangaran area. (a) Primary harzburgite minerals including olivine (Ol), orthopyroxene (Opx), clinopyroxene (Cpx) and Cr-spinel (Chr), which are replaced by serpentine forming pseudomorphic mesh texture (H2-45). (b) Bottom left, relict olivine with magnetite (Mag)-free mesh rim of lizardite (Lz) + brucite (Brc) together with orthopyroxene and clinopyroxene that have been altered to lizardite/bastite (Bst) (H2-27). (c) Lizardite mesh texture is overprinted by co-precipitation of interpenetrating antigorite (Atg) and carbonate (Carb) (H2-1), in plain-polarized light (upper) and cross-polarized light (lower). (d) Mesh textured lizardite in Lz-serpentinite being replaced by minor columnar antigorite along bigger interconnecting mesh rim that is consisting of several smaller mesh cells (reflected light). Antigorite also occurred around Cr-spinel grain replacing clinochlore (Clc) (H2-2). (e) The appearance of magnesite + antigorite assemblage on a big cell rim where the interconnecting rims of smaller mesh cells facilitated the ingress of a fluid with elevated CO_2 (compare it to a sealed veinlet in the inset) (H2-20). (f) Antigorite in Atg-serpentinite replaces lizardite relict in the matrix (Atg1) or bastite pseudomorph (Atg2) after orthopyroxene with incipient magnesite (H1-11). (g) Atg-Tlc-Mgs rock (H1-26). Inset shows interpenetrating antigorite replaced by talc (Tlc). Note that mesh cell can still be traced by the alignment of opaque phases. (h) Lizardite-bastite after orthopyroxene overprinted by interpenetrating antigorite with later talc + magnesite parallel to the original cleavages of the orthopyroxene (H1-26).

1123

1124 Fig. 6 Continued (i) tiny green flakes of fuchsite (Fu) associated with magnesite in silica-carbonate listvenite (H2-
1125 38). (j) Advanced stage of carbonation in silica-carbonate listvenite where the pseudomorphic mesh texture is
1126 still preserved with cells mainly composed of variable amounts of magnesite + quartz and traces serpentine (H2-
1127 34). (k) A closer look at an individual mesh cell showing progressive replacement of serpentine (Serp) relict by
1128 carbonate + quartz. Note that the alignments of opaque grains defines the mesh rim. (l) Dashed box area in
1129 figure j, where the entire mesh cell is replaced by magnesite + quartz due to entire dissolution of relict
1130 serpentine. (m) Silica-carbonate listvenite with quartz pseudomorph after talc (C-2). (n) Carbonate listvenite
1131 invaded by a late dolomite vein (H2-37). Note that in figures m and n, the pseudomorphic mesh texture is not
1132 recognizable. (o) Silica listvenite with a ghost of mesh texture that is developed by the arrangements of
1133 secondary porosity (por, H2-18). (p) Cryptocrystalline magnesite (Cryp-Mgs), cemented by coarser-grained
1134 dolomite spar (H2-3).

1135

1136 Fig. 7 Backscatter electron images (BSE) of Cr-spinel alteration patterns and different sulfide phases in variably
1137 carbonate altered ophiolitic rocks in the Hangaran area. (a) Fresh Cr-spinel (Chr) rimmed with a very narrow
1138 magnetite (Mag) in partially serpentinized harzburgite (H2-32). (b) Pentlandite (Pn) relicts showing alteration to
1139 native copper (Cu) + awaruite (Awr) + magnetite in harzburgite (H2-45). The inset represents the top right area
1140 of the BSE image, where the native copper is reddish in reflected light. (c) Zoned Cr-spinel in Atg-serpentinite is
1141 characterized by large unaltered chromite cores that is rimmed by narrow ferritchromite (Fchr) and Cr-
1142 magnetite rims in parts with hematite (Hem, bright area in reflected light) (H1-30). (d) Sulfide phases in Atg-
1143 serpentinites are dominated by millerite (Mlr, possibly after pentlandite or heazlewoodite) that weathered to
1144 garnierite (Gnt) (H1-11). Note that in fully-serpentinized rocks, native copper is not preserved but chalcopyrite
1145 (Cpy) inclusions occur in magnetite (inset, H2-20). (e) Highly zoned Cr-spinel in silica-carbonate listvenite with

1146 chromite core and well developed ferritchromite and magnetite rims (drill core, C-1). Note that the brecciated
1147 Cr-spinel is mantled by pyrite (Py) ± bravoite (Bvt, Ni-pyrite) and late generation of euhedral pyrite. (f)
1148 Disseminated bravoite with inclusions of cinnabar (Cin) in silica-carbonate listvenites (drill core, C-1). (g)
1149 Brecciated Cr-spinel relict in silica listvenites with two generations of pyrite ± bravoite (H1-22). (h) Violarite (Vlt)
1150 and rutile (Rut) in silica-carbonate listvenite (drill core, C-3). Other mineral abbreviations are the same as in
1151 figure 6.

1152

1153 Fig. 8. (a) MgO+CaO-SiO_2-LOI ternary diagram, showing bulk compositional variations for partially serpentinized
1154 harzburgite, serpentinite and listvenite lithologies in the Hangaran area. (b) Major element bulk rock variations.
1155 Due to similarities in the major element compositions of Lz- and Atg-serpentinites, they are shown as one group
1156 of serpentinite. Gray symbols to the right of data points for each group shows averages and standard errors.
1157 Trend lines showing apparent mobilization of selected major elements during carbonation and listvenitization.
1158 (c) Molar MgO versus molar SiO_2. (d) Mg# (molar Mg/(Mg+Fe)) versus molar SiO_2. Dotted and dashed black lines
1159 represent the average composition of Hangaran harzburgite disturbed by adding or removing Mg or Si,
1160 respectively. For comparison, data from Sahlabad (shaded areas; Aftabi and Zarrinkoub, 2013) and Wadi
1161 Mansah listvenites (empty circles; Falk and Kelemen, 2015) are also plotted. Compositions are recalculated on a
1162 volatile free basis. P.S.-partially serpentinized, Listv.-listvenite.

1163

1164 Fig. 9 Trace element and REE concentrations of partially serpentinized harzburgite (brown), and the averaged
1165 compositions of Lz-, Atg-serpentinites, and listvenite lithologies in Hangaran area normalized to primitive mantle
1166 (PM; Palme and O'Neill, 2014). (a, c) PM-normalized patterns of trace element and REE in different lithologies in
1167 Hangaran area. (b, d) PM-normalized patterns of trace element and REE of Hangaran listvenites in figure (a, c)
1168 compared to the fields of other listvenites in Greece (Hinsken et al., 2017) and eastern Iran (Aftabi and

1169 Zarrinkoub, 2013). The sequence of elements shown in figure (a, b) is based on increasing element mobility,
1170 from least mobile (left) to most mobile (right) elements. Compositions are recalculated on a volatile free basis.

1171

1172 Fig. 10 (a) Plots of stable isotope (O, C) compositions of studied lithologies in the Hangaran area. Dotted tie-lines
1173 connect values for listvenite core samples (C-0b, C-1b, C-3b) and dolomite veins (C-0v, C-1v, C-3v) for the same
1174 samples. Other carbonated ultramafic rocks and veins are shown for comparison: Advocate listvenite, Canada
1175 (Menzel et al., 2018); D (Derakht Senjed), Iranian magnesite deposits associated with ophiolite (Mirnejad et al.,
1176 2015); ANS: Arabian-Nubian Shield carbonated ophiolites and veins, Egypt (Boskabadi et al., 2017); Great
1177 Serpentinite Belt listvenite, Australia (Ashley, 1997), Appalachians listvenite, Canada (Auclair et al., 1993); L:
1178 Leka talc-carbonates, Norway (Bjerga et al., 2015); Linnajavri listvenite, Norway (Beinlich et al., 2012); Wadi
1179 Mansah listvenite, Oman (Falk and Kelemen, 2015); Tinos listvenite, Greece (Hinsken et al., 2017). The field of
1180 cryptocrystalline magnesite from Zedef et al. (2000) and compilation by García del Real et al. (2016). Each field
1181 represents > 90% of the data points from each particular group. Cretaceous/Tethyan limestone is from Keith and
1182 Weber (1964) and Menegatti et al. (1998). The field of mantle carbonate is from Taylor et al. (1967). (b) $\delta^{13}C$ and
1183 Sr isotope data, compared with the field of Oman and Tinos listvenites. Simple two-component mixing curves
1184 are calculated for mantle-seawater and mantle-limestone end members. A 59, 96, 600 and 16-19 Ma of age-
1185 corrections of Sr isotope ratios were used for Hangaran, Wadi Mansah, ANS and Tinos ultramafic listvenites and
1186 veins, respectively. The $^{87}Sr/^{86}Sr$ values of mantle defined by mid-ocean-ridge-basalt (MORB) from Allègre
1187 (2008). Cretaceous seawater is from the same references for $\delta^{13}C$ as in figure (a). The $^{87}Sr/^{86}Sr$ values of
1188 Cretaceous seawater (and modern seawater in figure (d) from Veizer et al. (1999). (c) $\delta^{13}C$ distribution in
1189 listvenite lithologies. (d) Sr isotope ratios compared to Cretaceous and modern seawaters, mantle range, and
1190 two listvenite data. ANS data are shown with grey dots. (e) Sulfur isotope values of pyrite veins in Hangaran
1191 listvenites compared to other sources (Hoefs, 2015) and listvenite lithologies including Barramiya listvenite
1192 (Zoheir and Lehmann, 2011).

Fig. 11 Listvenite mobility sequences, (a) harzburgite-normalized major and trace elements, and (b) REE patterns from different ophiolitic lithologies in Hangaran. Averaged compositions of each lithology type are recalculated on a volatile free basis.

Fig. 12 Alkali-U element discrimination fields of mid-ocean-ridge (MOR) and forearc (FA) serpentinites from Peters et al. (2017), representing >95% of the data points from each particular group. (a) Cs/U vs. Li/U and (b) Cs/U vs. Rb/U. Blue and red stars, are showing the composition of ocean water (Li, 1991) and global subducted sediment (i.e., GLOSSII; Plank, 2014), respectively.

Fig. 13. Sketch illustrating a possible geodynamic setting for Hangaran listvenite (red star) during final stage of Neotethys closure, Eocene-Oligocene obduction of the Birjand ophiolite in Sistan Suture Zone (SsSZ) eastern Iran. Red arrows show possible fluid sources generated by expulsion of pore fluid and structurally bound fluid trapped within the subducted/overthrusted metasediments, whereas blue arrow indicates late meteoric fluid.

Supplementary document

Supplementary figure S1 caption

Fig. S1 (a) Chemical variations of Cr# [Cr/(Cr+Al)] versus Mg# [Mg/(Mg+Fe^{2+})] in Cr-spinel (Cr-Sp) cores of the Hangaran partially serpentinized (P. S.) harzburgite compared to the compositions of Cr-spinel from the Birjand (Moghadam and Stern, 2015) and Nehbandan peridotites (Saccani et al., 2010). Compositional fields for Cr-spinel are from different compilations including Oman (Le Mée et al., 2004, Hanghøj et al., 2010), abyssal (MORB, Dick and Bullen, 1984), forearc (Parkinson and Pearce, 1998) and backarc peridotites (Mariana Trough, Ohara et al., 2002), as well as general boninite field (Tamura and Arai, 2006 and references therein). (b) Composition of orthopyroxenes (Opx) in the Hangaran partially serpentinized harzburgite. Compositional field of forearc and abyssal peridotite from Pagé et al. (2008).

Fig. S2 Positive correlation between As, Mo, Sb, Sn, W, and S in sulfide-rich listvenites.

Supplementary references

Dick, H.J.B., Bullen, T., 1984. Chromian spinel as a petrogenetic indicator in abyssal and alpine-type peridotites and spatially associated lavas. Contribution to Mineralogy and Petrology 86, 54–76. https://doi.org/10.1007/BF00373711

Hanghøj, K., Kelemen, P.B., Hassler, D., Godard, M., 2010. Composition and genesis of depleted mantle peridotites from the Wadi Tayin massif, Oman ophiolite; Major and trace element geochemistry, and Os isotope and PGE systematics. Journal of Petrology 51, 201–227. https://doi.org/10.1093/petrology/egp077

Le Mée, L., Girardeau, J., Monnier, C., 2004. Mantle segmentation along the Oman ophiolite fossil mid-ocean ridge. Nature 432, 167–172. https://doi.org/10.1038/nature03075

Moghadam, H.S., Stern, R.J., 2015. Ophiolites of Iran: Keys to understanding the tectonic evolution of SW Asia: (II) Mesozoic ophiolites. Journal of Asian Earth Sciences 100, 31–59.

https://doi.org/10.1016/j.jseaes.2014.12.016

Ohara, Y., Stern, R.J., Ishii, T., Yurimoto, H., Yamazaki, T., 2002. Peridotites from the Mariana Trough: First look at the mantle beneath an active back-arc basin. Contribution to Mineralogy and Petrology 143, 1–18. https://doi.org/10.1007/s00410-001-0329-2

Pagé, P., Bédard, J.H., Schroetter, J.-M., Tremblay, A., 2008. Mantle petrology and mineralogy of the Thetford Mines ophiolite complex. Lithos 100, 255–292

Parkinson, I.J., Pearce, J.A., 1998. Peridotites from the Izu-Bonin-Mariana Forearc (ODP Leg 125): Evidence for mantle melting and melt-mantle interaction in a supra-subduction zone setting. Journal of Petrology 39, 1577–1618. https://doi.org/10.1093/petrology/39.9.1577

Saccani, E., Delavari, M., Beccaluva, L., Amini, S., 2010. Petrological and geochemical constraints on the origin of the Nehbandan ophiolitic complex (eastern Iran): Implication for the evolution of the Sistan Ocean. Lithos 117, 209–228. https://doi.org/10.1016/j.lithos.2010.02.016

Tamura, A., Arai, S., 2006. Harzburgite-dunite-orthopyroxenite suite as a record of supra-subduction zone setting for the Oman ophiolite mantle. Lithos 90, 43–56. https://doi.org/10.1016/j.lithos.2005.12.012

Figure1

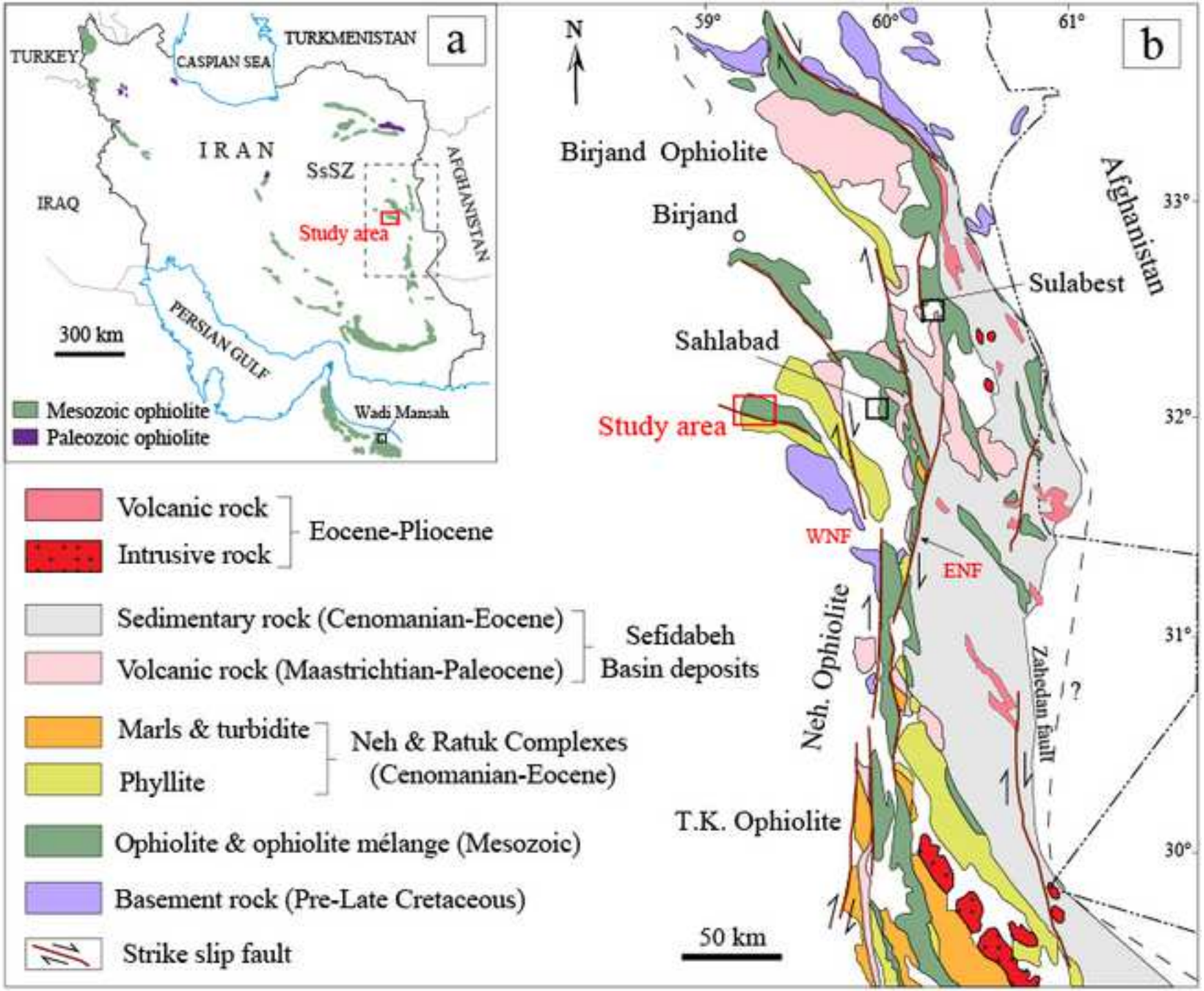
a
TURKEY
CASPIAN SEA
TURKMENISTAN
IRAN
SsSZ
IRAQ
AFGHANISTAN
Study area
PERSIAN GULF
300 km
Wadi Mansah
Mesozoic ophiolite
Paleozoic ophiolite
b
N
59°
60°
61°
Birjand Ophiolite
Birjand
Afghanistan
33°
Sulabest
Sahlabad
Study area
32°
WNF
ENF
Neh. Ophiolite
Zahedan fault
?
31°
T.K. Ophiolite
30°
50 km
Volcanic rock
Intrusive rock
Eocene-Pliocene
Sedimentary rock (Cenomanian-Eocene)
Volcanic rock (Maastrichtian-Paleocene)
Sefidabeh Basin deposits
Marls & turbidite
Phyllite
Neh & Ratuk Complexes (Cenomanian-Eocene)
Ophiolite & ophiolite mélange (Mesozoic)
Basement rock (Pre-Late Cretaceous)
Strike slip fault

Figure2

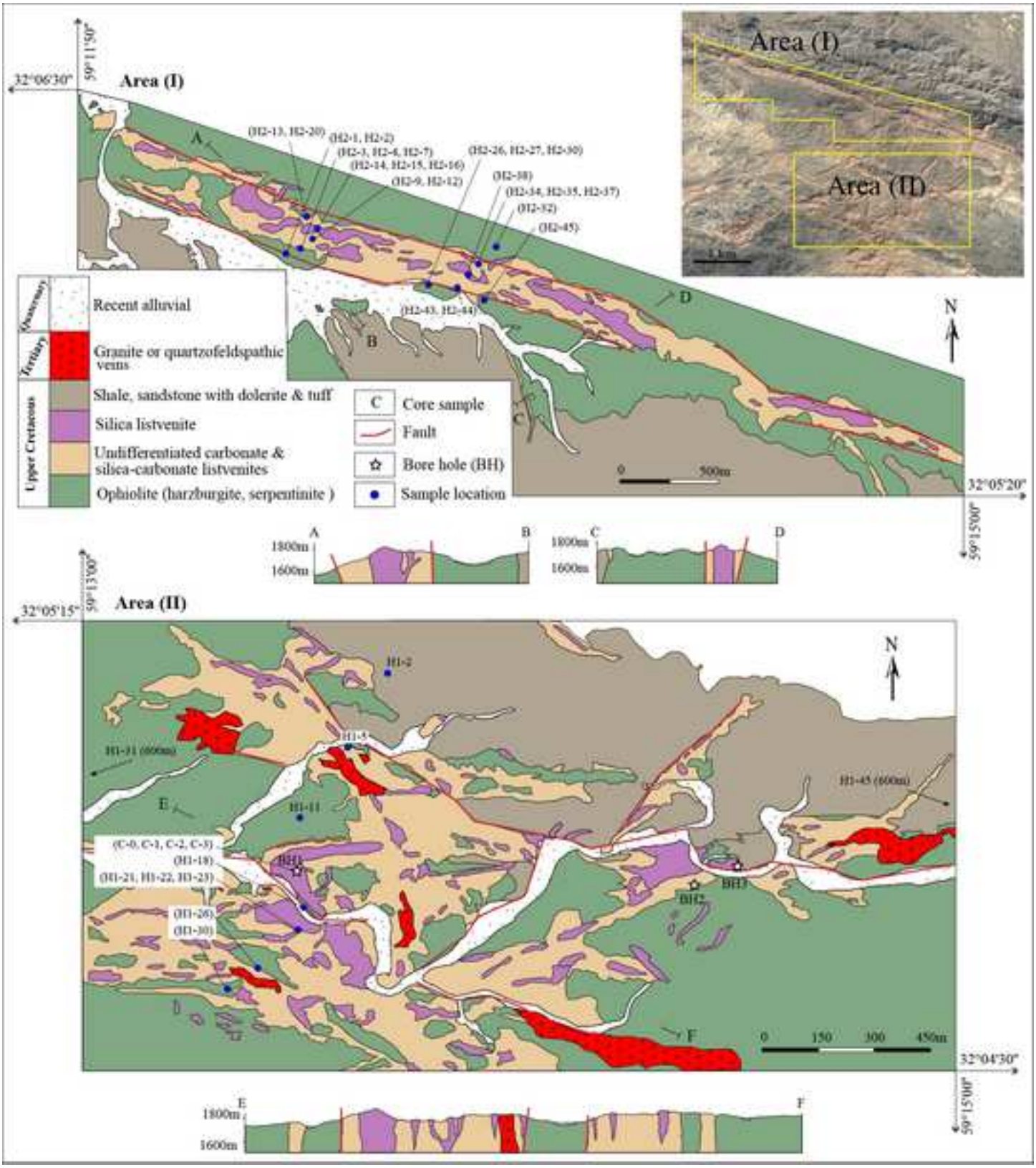
Area (I)
Area (II)
32°06'30"
59°11'50"
32°05'20"
59°15'00"
32°05'15"
59°13'00"
32°04'30"
59°15'00"
(H2-13, H2-20)
(H2-1, H2-2)
(H2-3, H2-4, H2-7)
(H2-14, H2-15, H2-16)
(H2-9, H2-12)
(H2-26, H2-27, H2-30)
(H2-10)
(H2-34, H2-35, H2-37)
(H2-32)
(H2-45)
(H2-43, H2-44)
Recent alluvial
Granite or quartzofeldspathic veins
Shale, sandstone with dolerite & tuff
Silica listvenite
Undifferentiated carbonate & silica-carbonate listvenites
Ophiolite (harzburgite, serpentinite)
Quaternary
Tertiary
Upper Cretaceous
C Core sample
Fault
Bore hole (BH)
Sample location
0 500m
N
1800m
1600m
H1-2
H1-5
H1-31 (600m)
H1-45 (600m)
H1-11
(C-0, C-1, C-2, C-3)
(H1-18)
(H1-21, H1-22, H1-23)
(H1-26)
(H1-30)
BH1
BH2
BH3
0 150 300 450m

Figure3

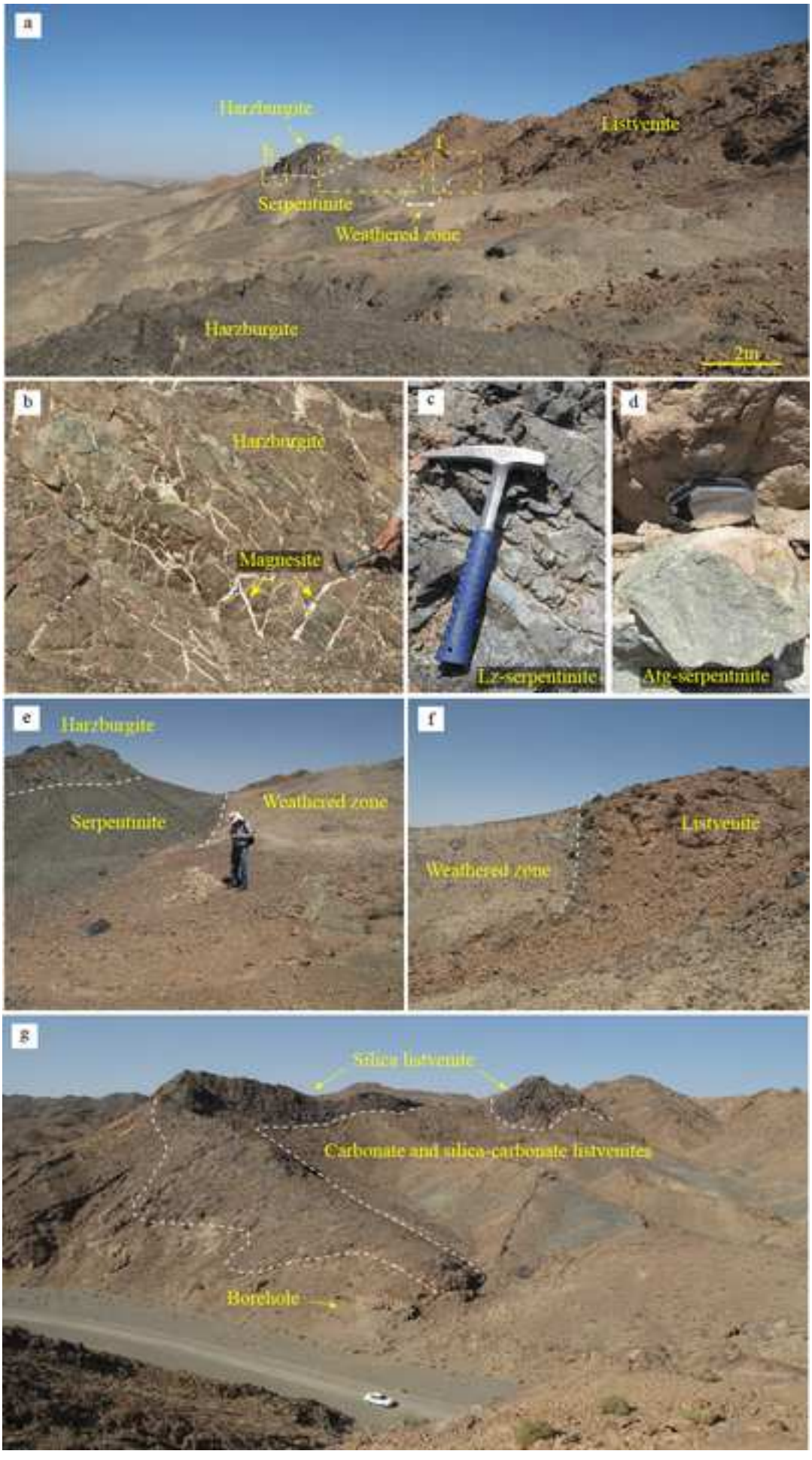
a
Harzburgite
Listvenite
Serpentinite
Weathered zone
Harzburgite
2m
b
Harzburgite
Magnesite
c
Lz-serpentinite
d
Atg-serpentinite
e
Harzburgite
Serpentinite
Weathered zone
f
Listvenite
Weathered zone
g
Silica listvenite
Carbonate and silica-carbonate listvenites
Borehole

Figure4

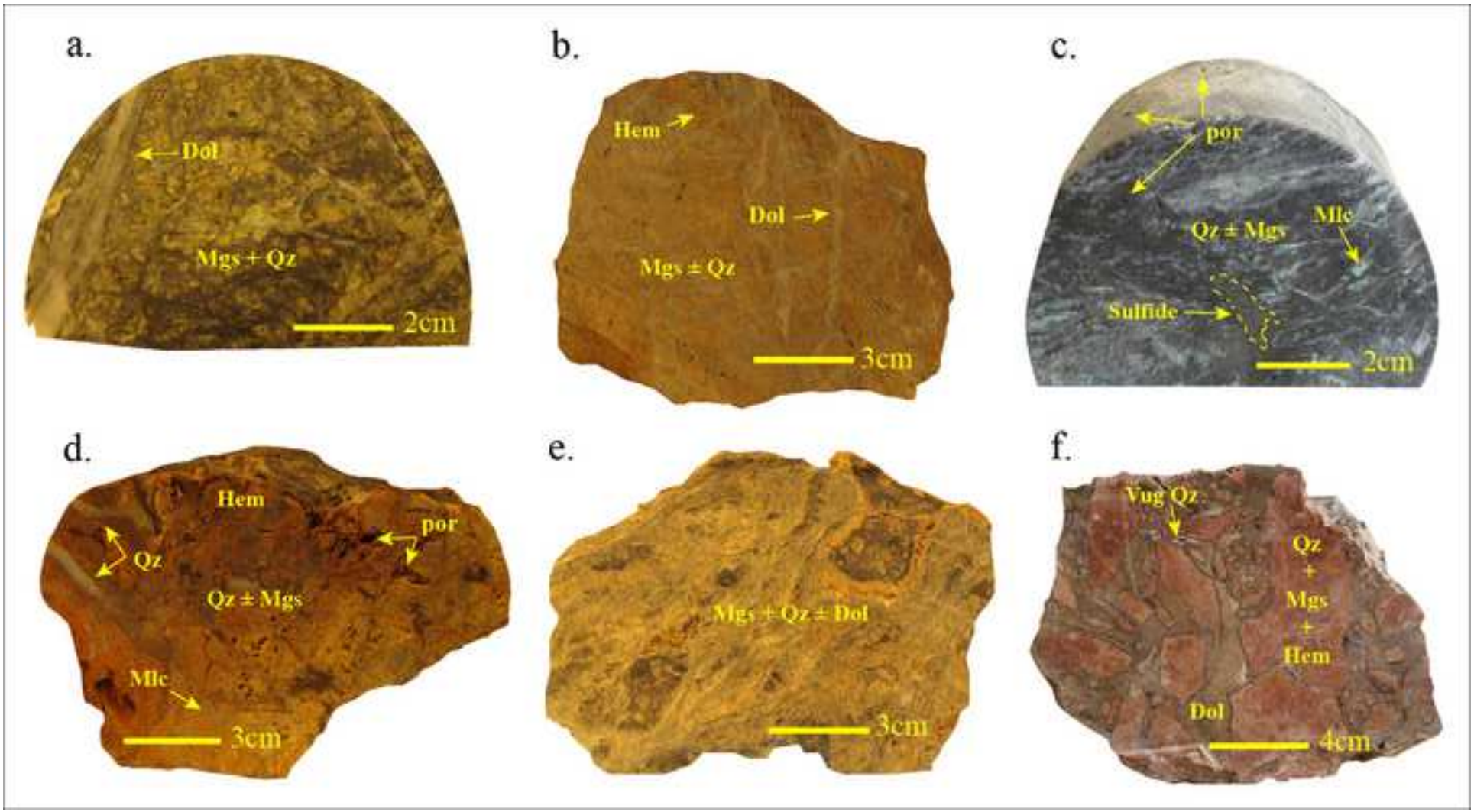
a.
Dol
Mgs + Qz
2cm
b.
Hem
Dol
Mgs ± Qz
3cm
c.
por
Qz ± Mgs
Mlc
Sulfide
2cm
d.
Hem
por
Qz
Qz ± Mgs
Mlc
3cm
e.
Mgs + Qz ± Dol
3cm
f.
Vug Qz
Qz
+
Mgs
+
Hem
Dol
4cm

Figure5

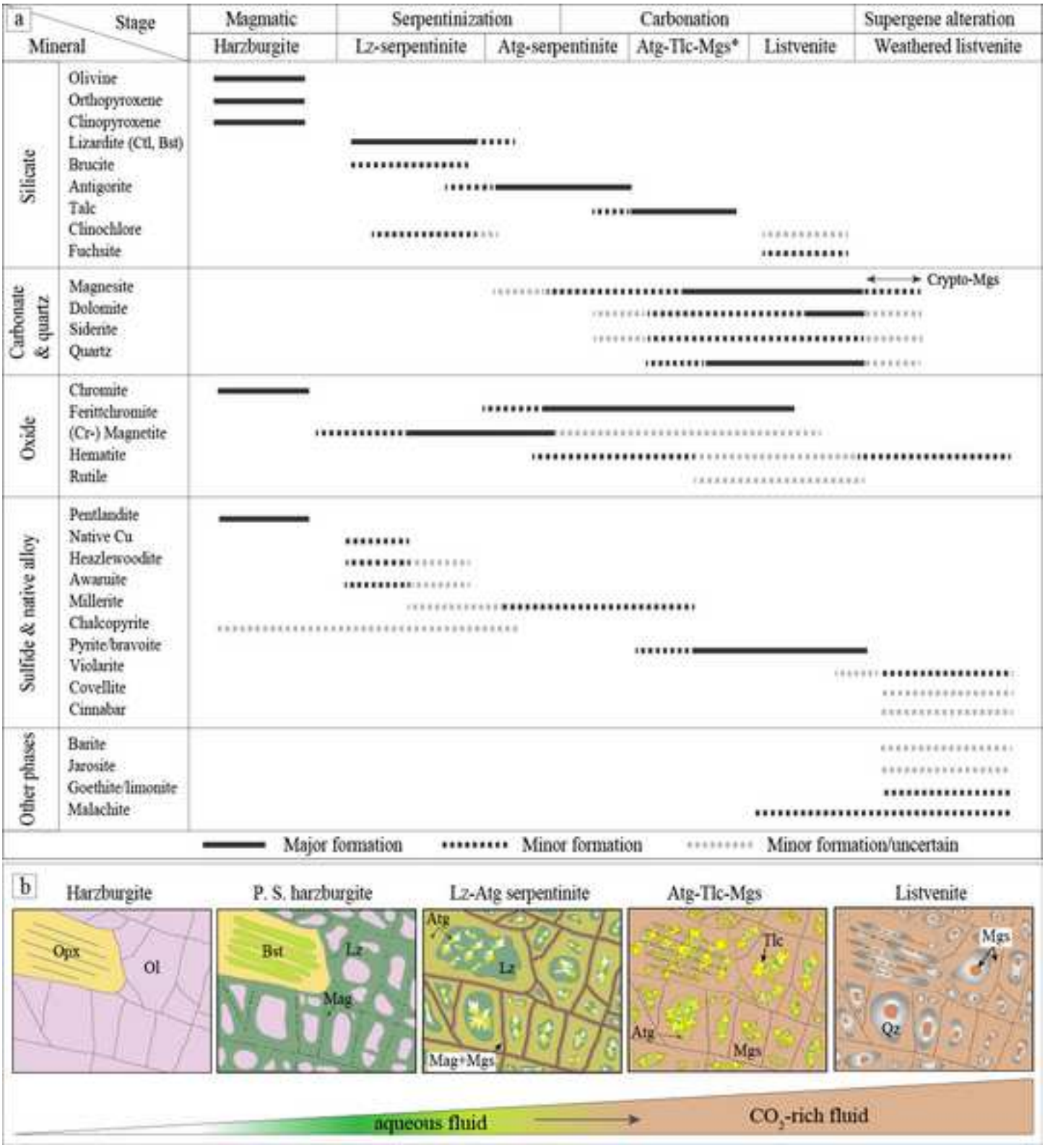
a
Stage
Mineral
Magmatic
Serpentinization
Carbonation
Supergene alteration
Harzburgite
Lz-serpentinite
Atg-serpentinite
Atg-Tlc-Mgs*
Listvenite
Weathered listvenite
Silicate
Olivine
Orthopyroxene
Clinopyroxene
Lizardite (Ctl, Bst)
Brucite
Antigorite
Talc
Clinochlore
Fuchsite
Carbonate & quartz
Magnesite
Dolomite
Siderite
Quartz
Crypto-Mgs
Oxide
Chromite
Ferritchromite
(Cr-) Magnetite
Hematite
Rutile
Sulfide & native alloy
Pentlandite
Native Cu
Heazlewoodite
Awaruite
Millerite
Chalcopyrite
Pyrite/bravoite
Violarite
Covellite
Cinnabar
Other phases
Barite
Jarosite
Goethite/limonite
Malachite
Major formation
Minor formation
Minor formation/uncertain
b
Harzburgite
P. S. harzburgite
Lz-Atg serpentinite
Atg-Tlc-Mgs
Listvenite
Opx
Ol
Bst
Lz
Mag
Atg
Lz
Mag+Mgs
Tlc
Atg
Mgs
Mgs
Qz
aqueous fluid
CO2-rich fluid

Figure6

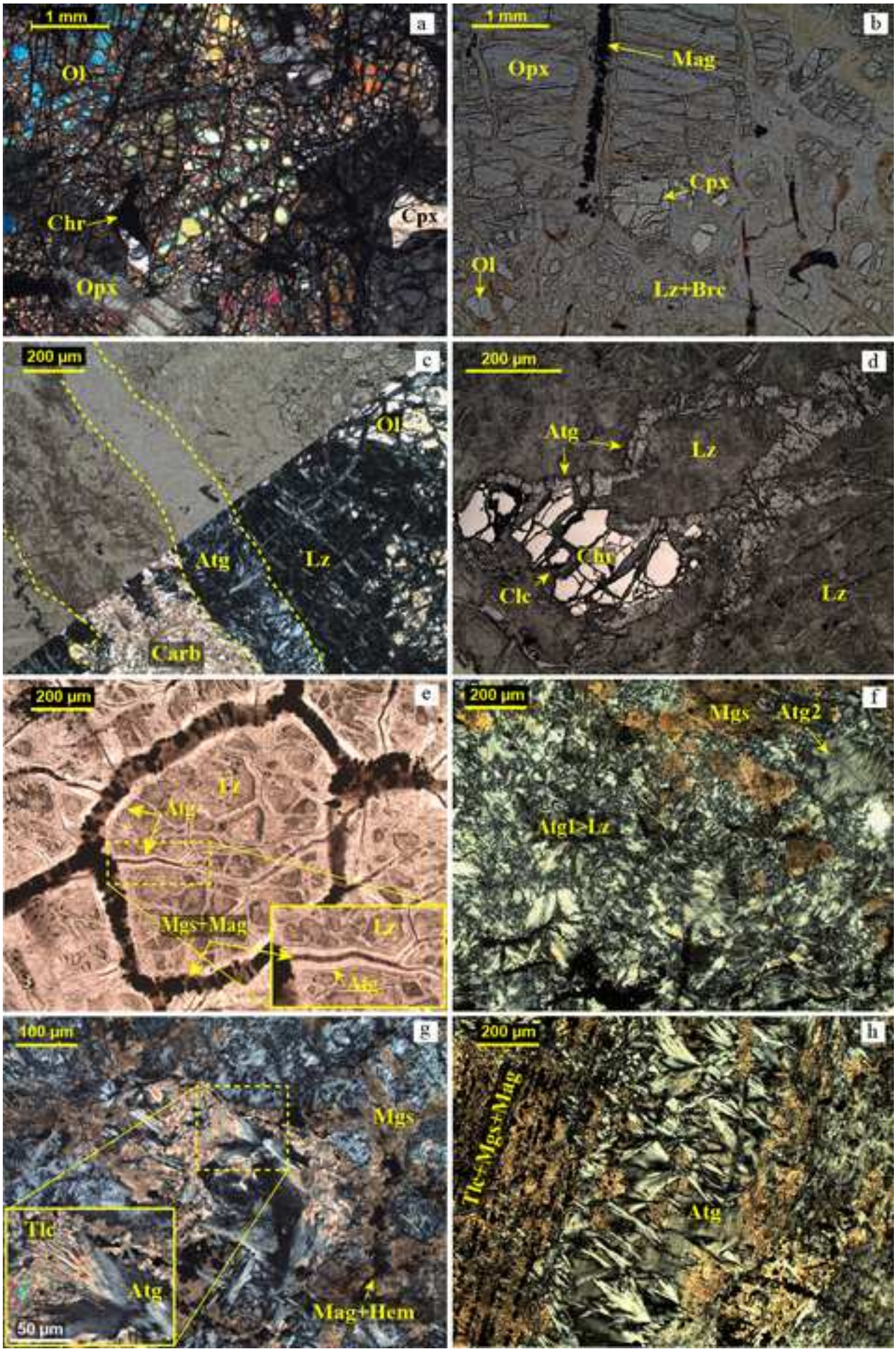
1 mm
a
Ol
Chr
Cpx
Opx
1 mm
b
Opx
Mag
Cpx
Ol
Lz+Brc
200 μm
c
Ol
Atg
Lz
Carb
200 μm
d
Atg
Lz
Chr
Cle
Lz
200 μm
e
Ol
Atg
Mgs+Mag
Lz
Atg
200 μm
f
Mgs
Atg2
Atg1>Lz
100 μm
g
Mgs
Tlc
Atg
Mag+Hem
50 μm
200 μm
h
Tlc+Mgs+Mag
Atg

Figure6(continued)

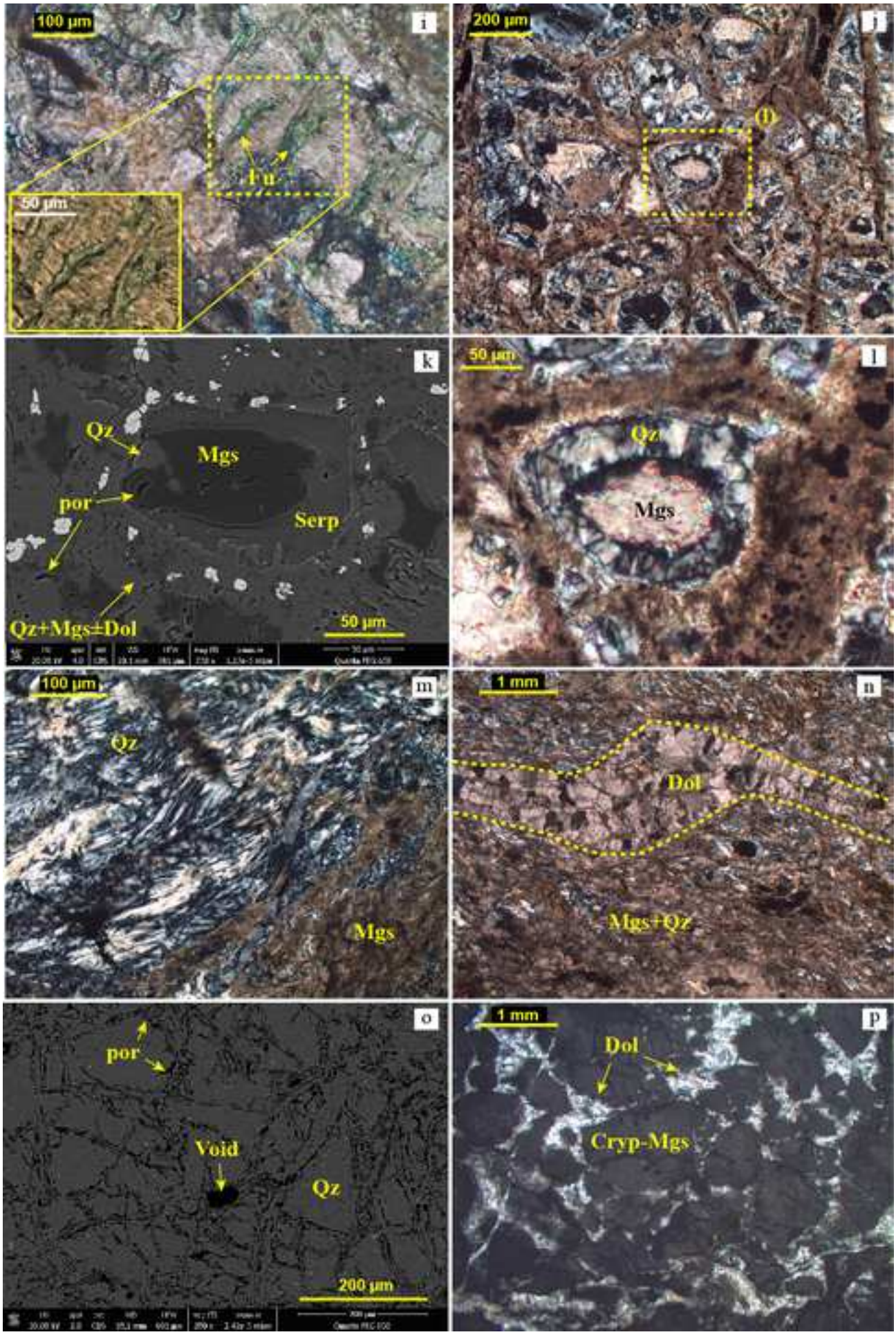

Figure7

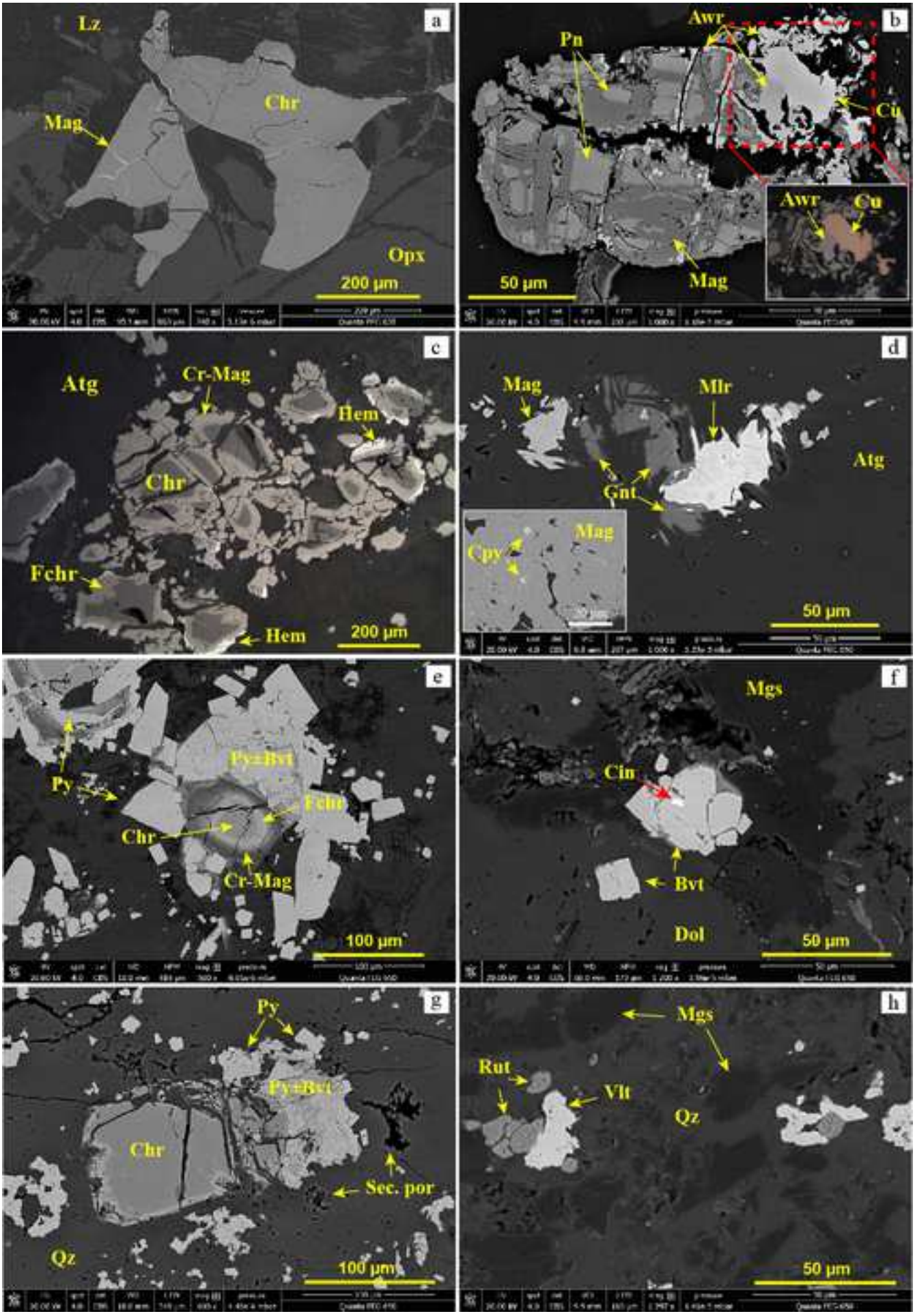
a
Lz
Chr
Mag
Opx
200 μm
b
Awr
Pn
Cu
Awr
Cu
50 μm
Mag
c
Atg
Cr-Mag
Hem
Chr
Fchr
Hem
200 μm
d
Mag
Mlr
Atg
Gnt
Mag
Cpy
50 μm
e
Py
Py+Bvt
Fchr
Chr
Cr-Mag
100 μm
f
Mgs
Cin
Bvt
Dol
50 μm
g
Py
Py+Bvt
Chr
Sec. por
Qz
100 μm
h
Mgs
Rut
Vlt
Qz
50 μm

Figure8

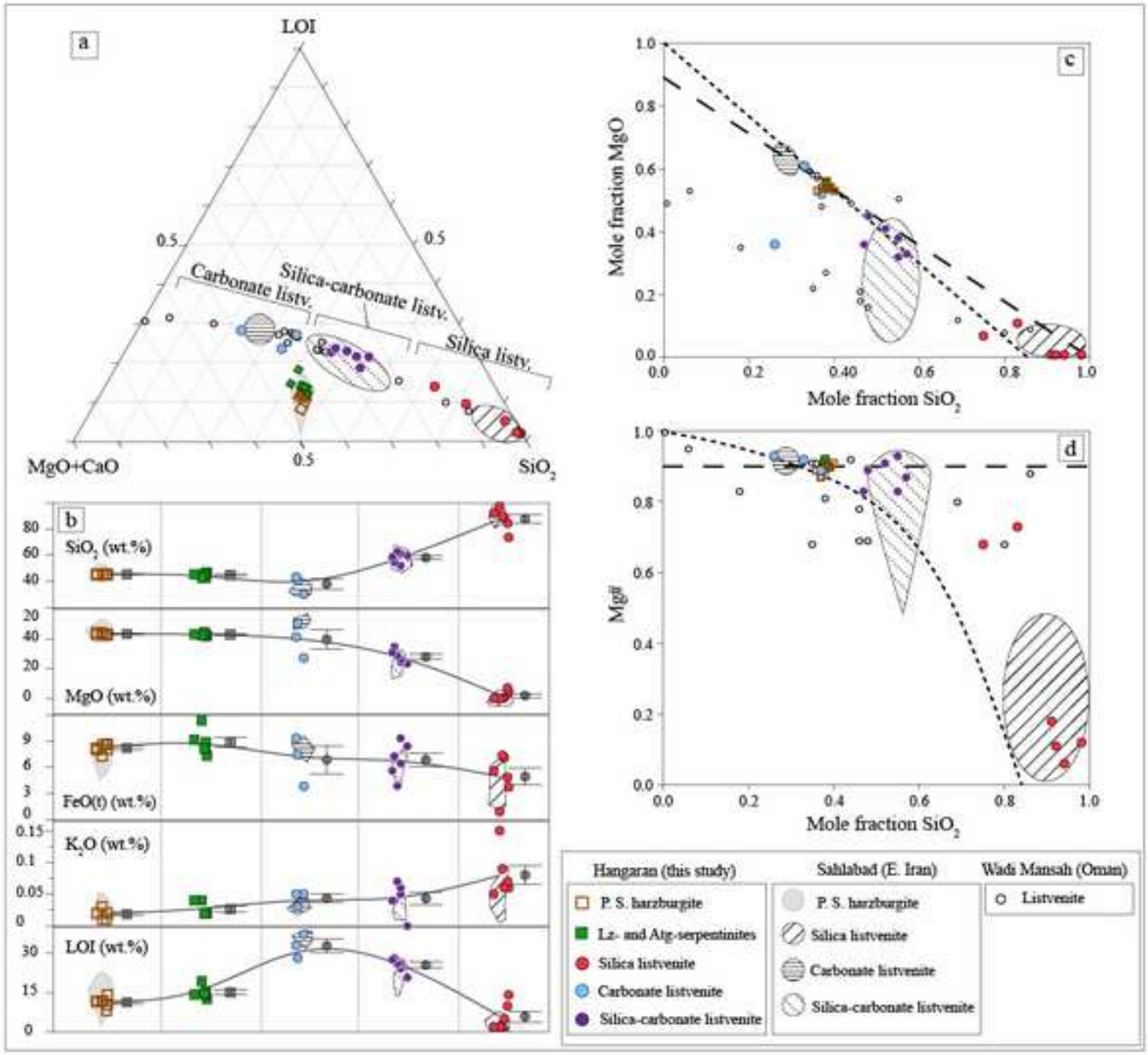
a
LOI
MgO+CaO
SiO2
0.5
0.5
0.5
Carbonate listv.
Silica-carbonate listv.
Silica listv.
b
SiO2 (wt.%)
MgO (wt.%)
FeO(t) (wt.%)
K2O (wt.%)
LOI (wt.%)
c
Mole fraction MgO
Mole fraction SiO2
d
Mg#
Mole fraction SiO2
Hangaran (this study)
P. S. harzburgite
Lz- and Atg-serpentinites
Silica listvenite
Carbonate listvenite
Silica-carbonate listvenite
Sahlabad (E. Iran)
P. S. harzburgite
Silica listvenite
Carbonate listvenite
Silica-carbonate listvenite
Wadi Mansah (Oman)
Listvenite

Figure9

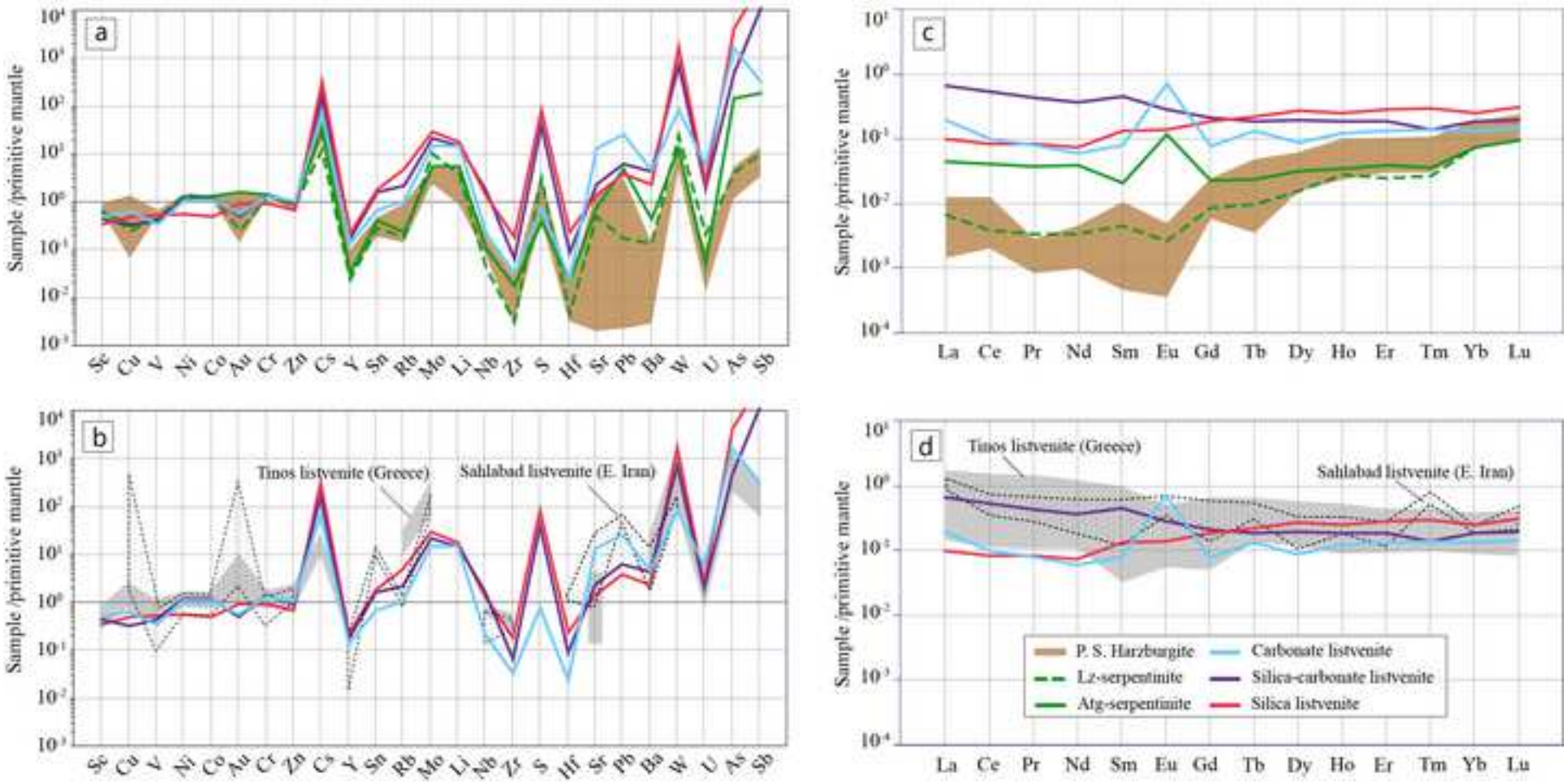
a
b
c
d
Sample /primitive mantle
Se Cu V Ni Co Au Cr Zn Cs Y Sn Rb Mo Li Nb Zr S Hf Sr Pb Ba W U As Sb
La Ce Pr Nd Sm Eu Gd Tb Dy Ho Er Tm Yb Lu
Tinos listvenite (Greece)
Sahlabad listvenite (E. Iran)
P. S. Harzburgite
Lz-serpentinite
Atg-serpentinite
Carbonate listvenite
Silica-carbonate listvenite
Silica listvenite

Figure10

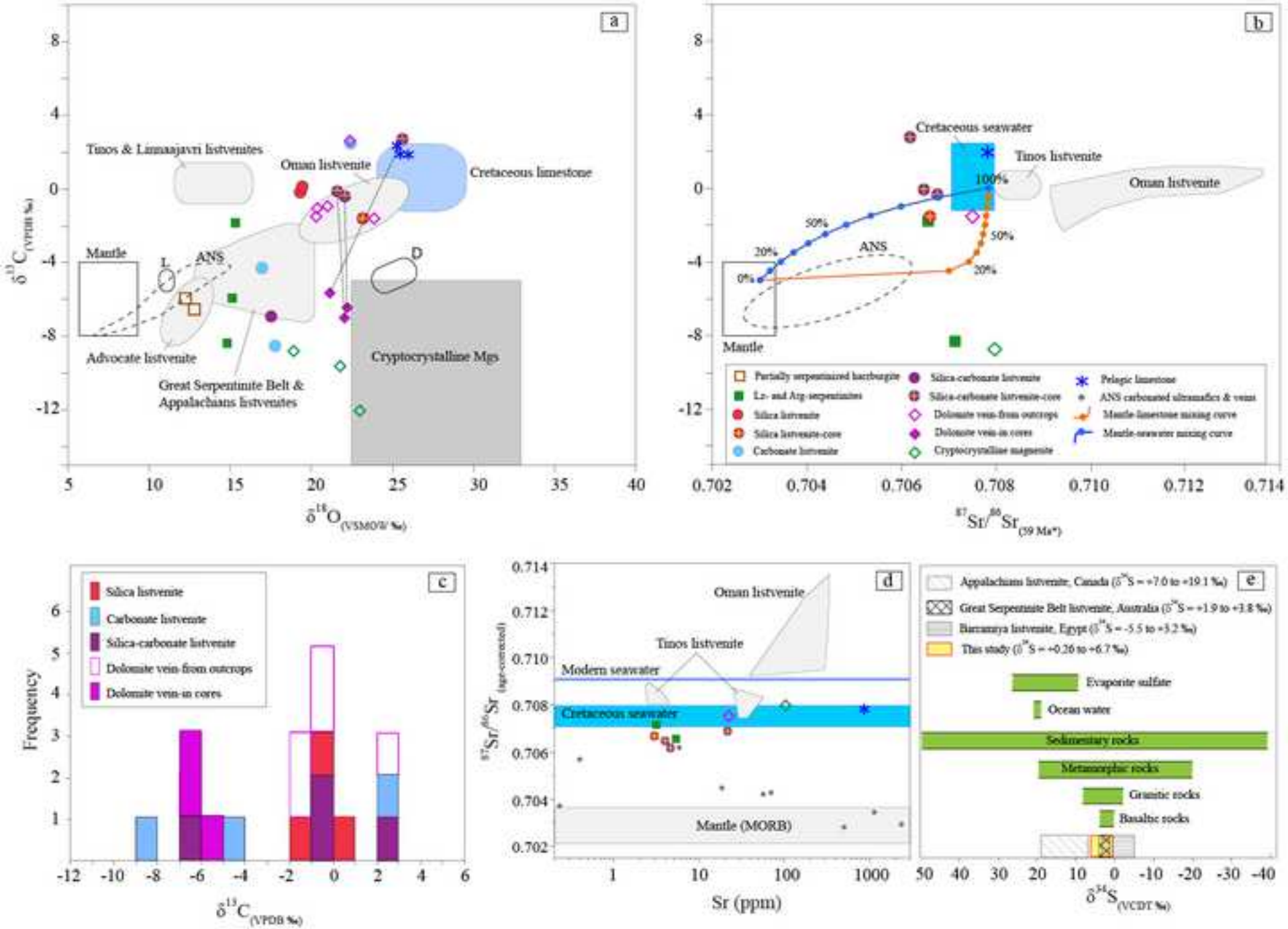
a
Tinos & Linnaajavri listvenites
Oman listvenite
Cretaceous limestone
Mantle
L
ANS
D
Advocate listvenite
Great Serpentinite Belt &
Appalachians listvenites
Cryptocrystalline Mgs
δ13C(VPDB ‰)
δ18O(VSMOW ‰)
b
Cretaceous seawater
Tinos listvenite
Oman listvenite
100%
50%
50%
20%
ANS
20%
0%
Mantle
Partially serpentinized harzburgite
Lz- and Atg-serpentinites
Silica listvenite
Silica listvenite-core
Carbonate listvenite
Silica-carbonate listvenite
Silica-carbonate listvenite-core
Dolomite vein-from outcrops
Dolomite vein-in cores
Cryptocrystalline magnesite
Pelagic limestone
ANS carbonated ultramafics & veins
Mantle-limestone mixing curve
Mantle-seawater mixing curve
87Sr/86Sr(59 Ma*)
c
Silica listvenite
Carbonate listvenite
Silica-carbonate listvenite
Dolomite vein-from outcrops
Dolomite vein-in cores
Frequency
δ13C(VPDB ‰)
d
Oman listvenite
Tinos listvenite
Modern seawater
Cretaceous seawater
Mantle (MORB)
87Sr/86Sr(age-corrected)
Sr (ppm)
e
Appalachians listvenite, Canada (δ34S = +7.0 to +19.1 ‰)
Great Serpentinite Belt listvenite, Australia (δ34S = +1.9 to +3.8 ‰)
Barramiya listvenite, Egypt (δ34S = -5.5 to +3.2 ‰)
This study (δ34S = +0.20 to +6.7 ‰)
Evaporite sulfate
Ocean water
Sedimentary rocks
Metamorphic rocks
Granitic rocks
Basaltic rocks
δ34S(VCDT ‰)

Figure11

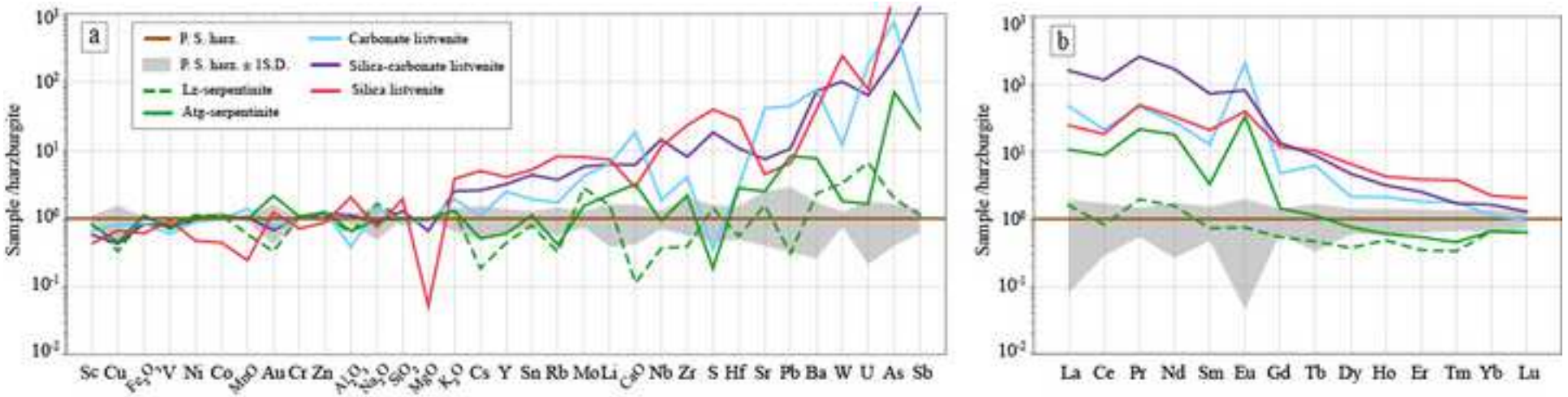
a
P. S. harz.
P. S. harz. ± IS.D.
Lz-serpentinite
Atg-serpentinite
Carbonate listvenite
Silica-carbonate listvenite
Silica listvenite
Sample /harzburgite
Sc Cu Fe2O3 V Ni Co MnO Au Cr Zn Al2O3 CaO SiO2 MgO K2O Cs Y Sn Rb Mo Li CaO Nb Zr S Hf Sr Pb Ba W U As Sb
b
Sample /harzburgite
La Ce Pr Nd Sm Eu Gd Tb Dy Ho Er Tm Yb Lu

Figure12

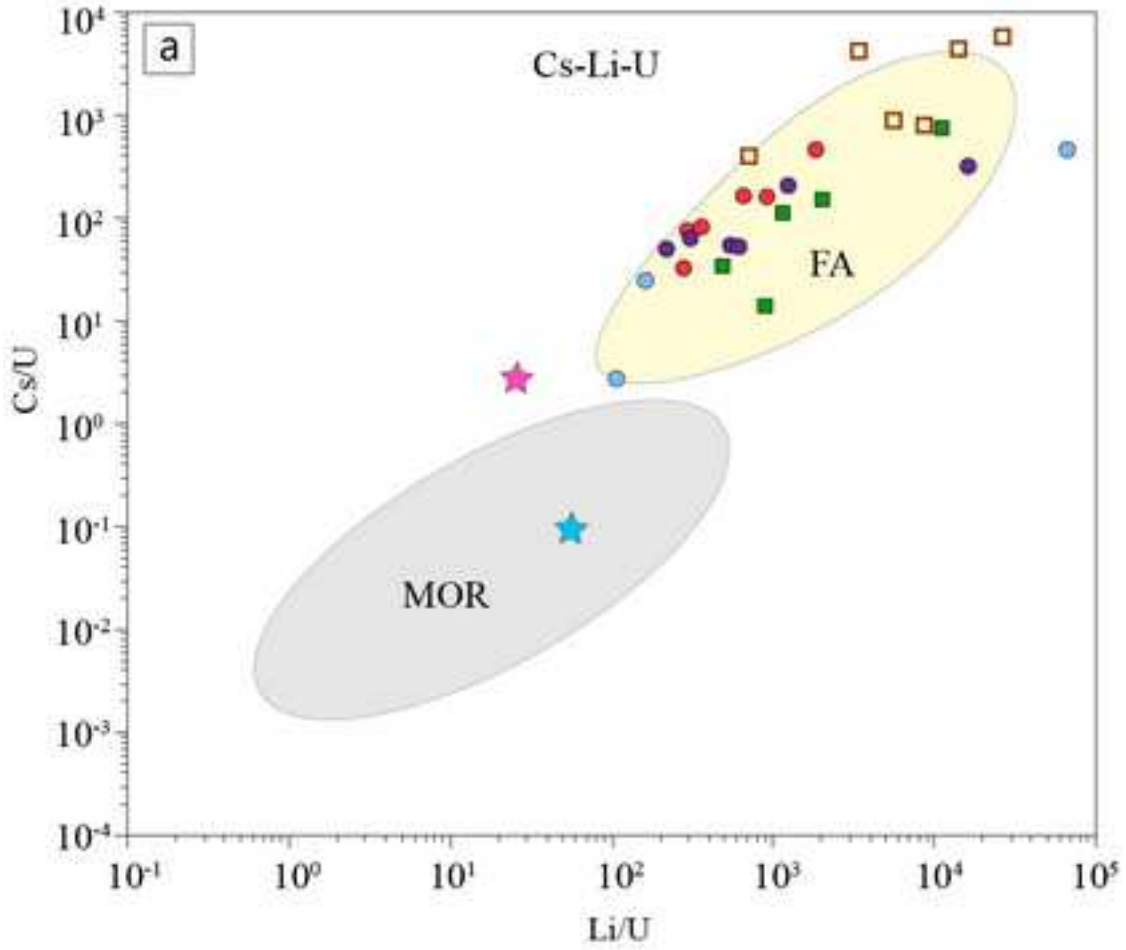
a
Cs-Li-U
FA
MOR
Cs/U
Li/U
10^{4}
10^{3}
10^{2}
10^{1}
10^{0}
10^{-1}
10^{-2}
10^{-3}
10^{-4}
10^{-1}
10^{0}
10^{1}
10^{2}
10^{3}
10^{4}
10^{5}

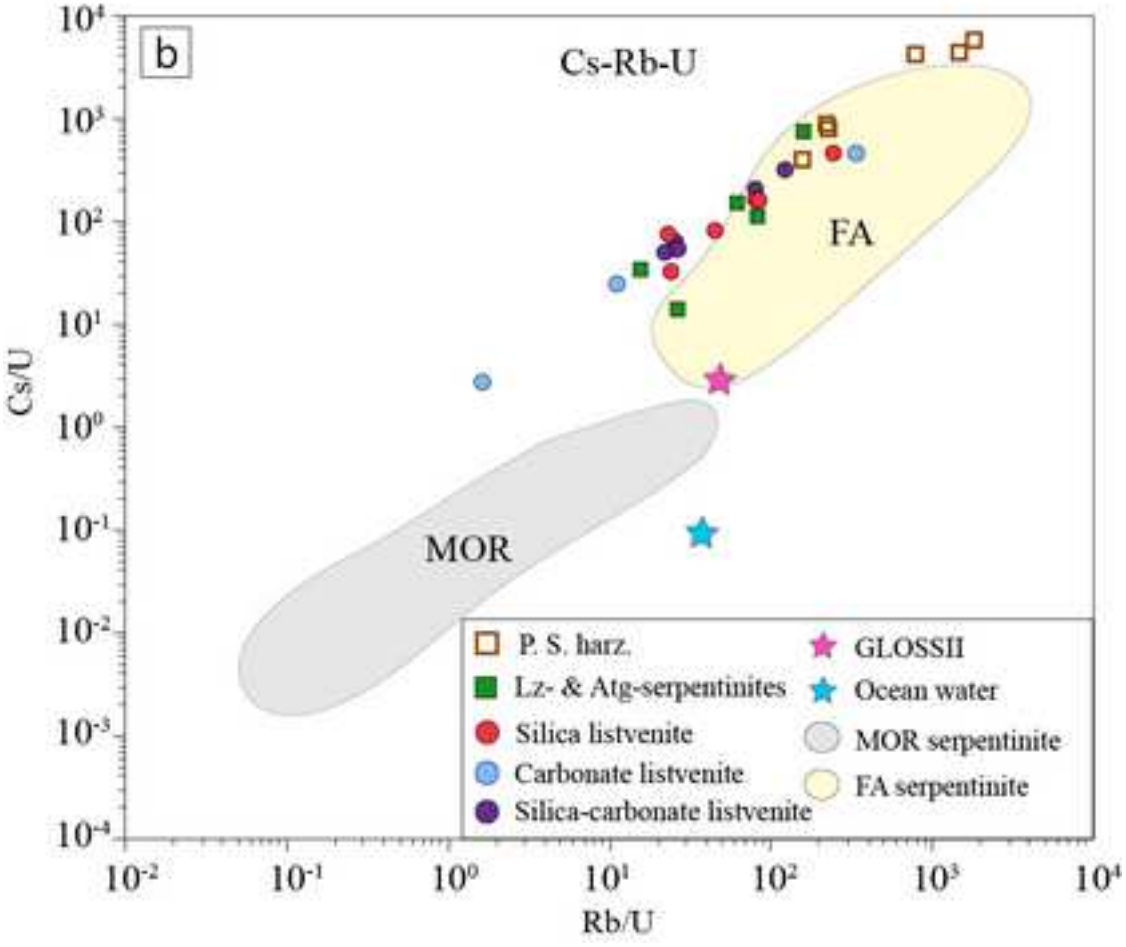
b
Cs-Rb-U
FA
MOR
Cs/U
Rb/U
P. S. harz.
Lz- & Atg-serpentinites
Silica listvenite
Carbonate listvenite
Silica-carbonate listvenite
GLOSSII
Ocean water
MOR serpentinite
FA serpentinite
10^{4}
10^{3}
10^{2}
10^{1}
10^{0}
10^{-1}
10^{-2}
10^{-3}
10^{-4}
10^{-2}
10^{-1}
10^{0}
10^{1}
10^{2}
10^{3}
10^{4}

Figure13

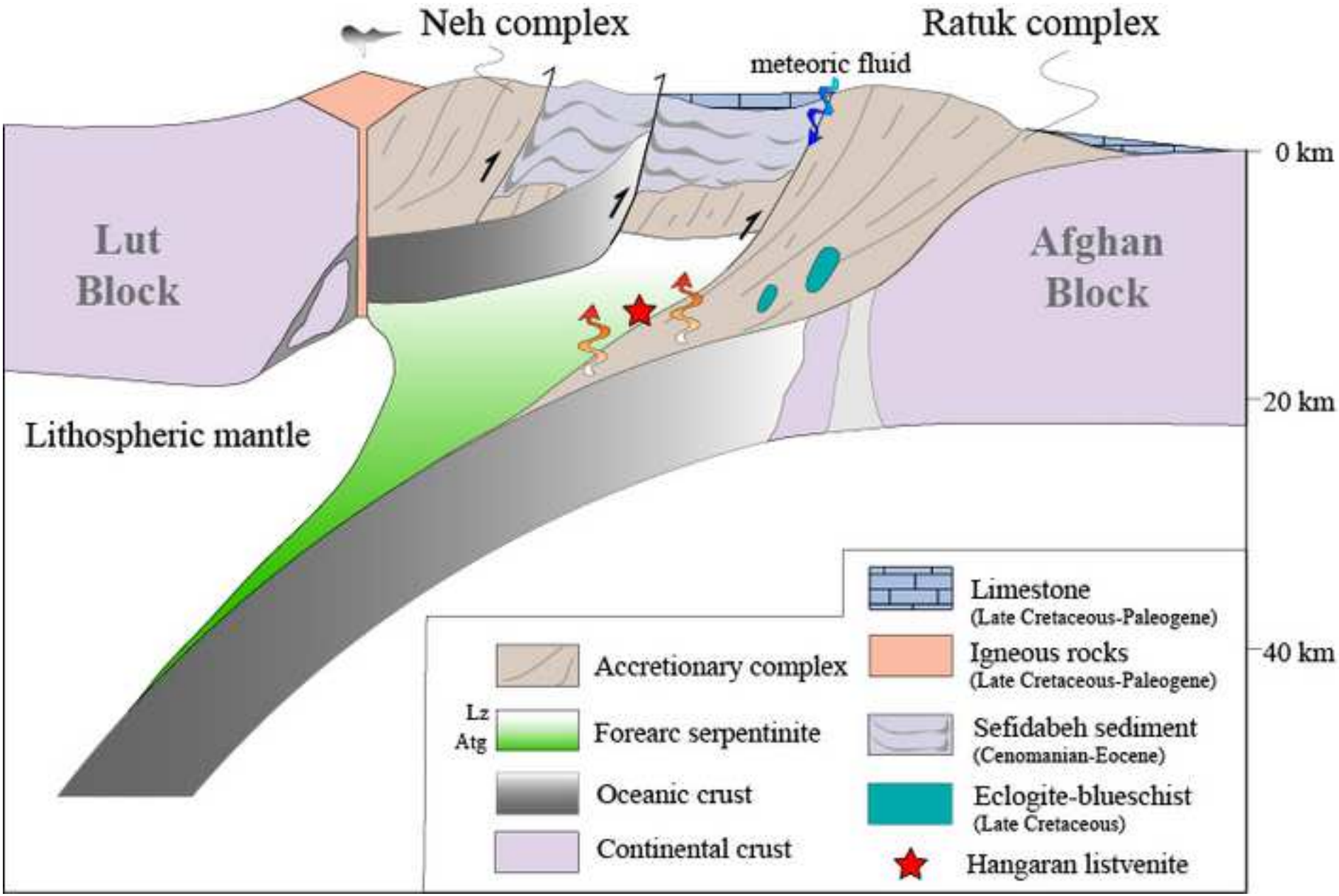
Neh complex
Ratuk complex
meteoric fluid
Lut Block
Afghan Block
Lithospheric mantle
1
1
1
0 km
20 km
40 km
Limestone
(Late Cretaceous-Paleogene)
Igneous rocks
(Late Cretaceous-Paleogene)
Sefidabeh sediment
(Cenomanian-Eocene)
Eclogite-blueschist
(Late Cretaceous)
Hangaran listvenite
Accretionary complex
Lz
Atg
Forearc serpentinite
Oceanic crust
Continental crust

Supplementary Figure S1

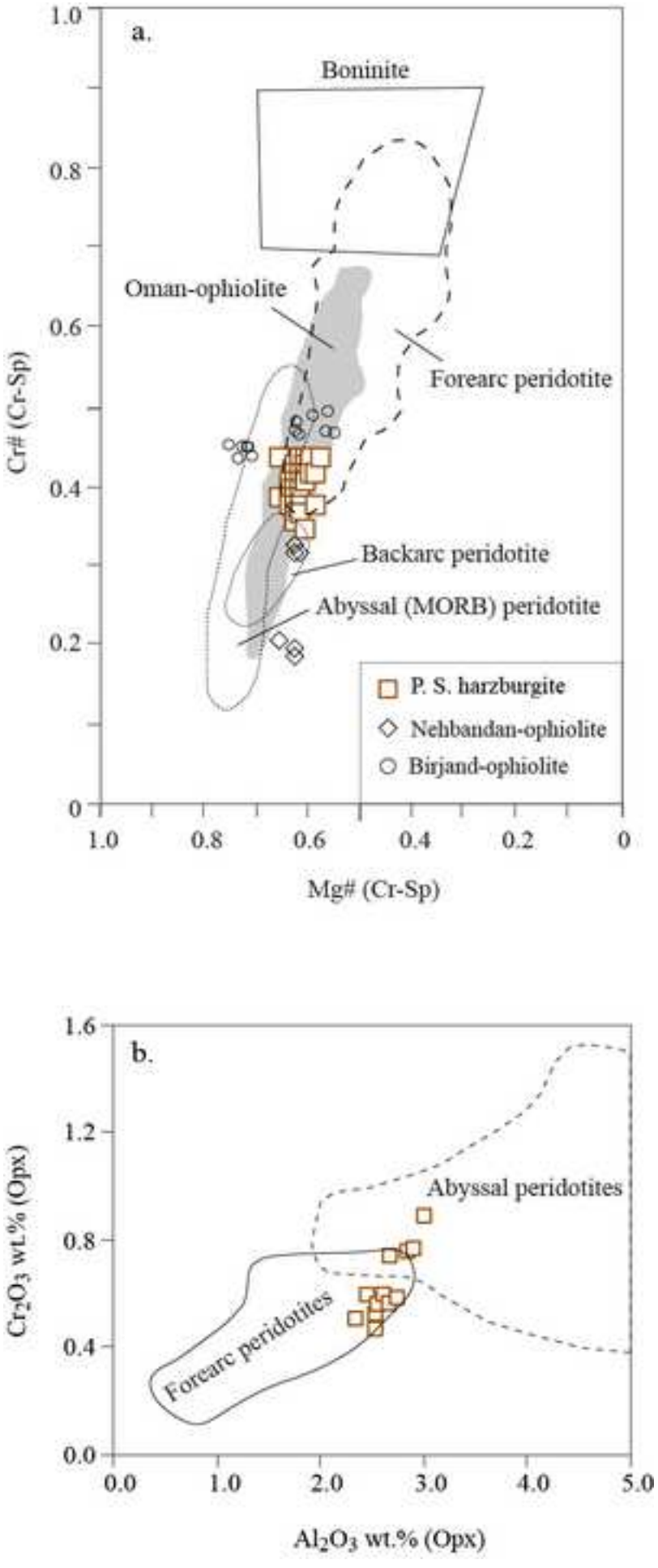

Supplementary Figure S2

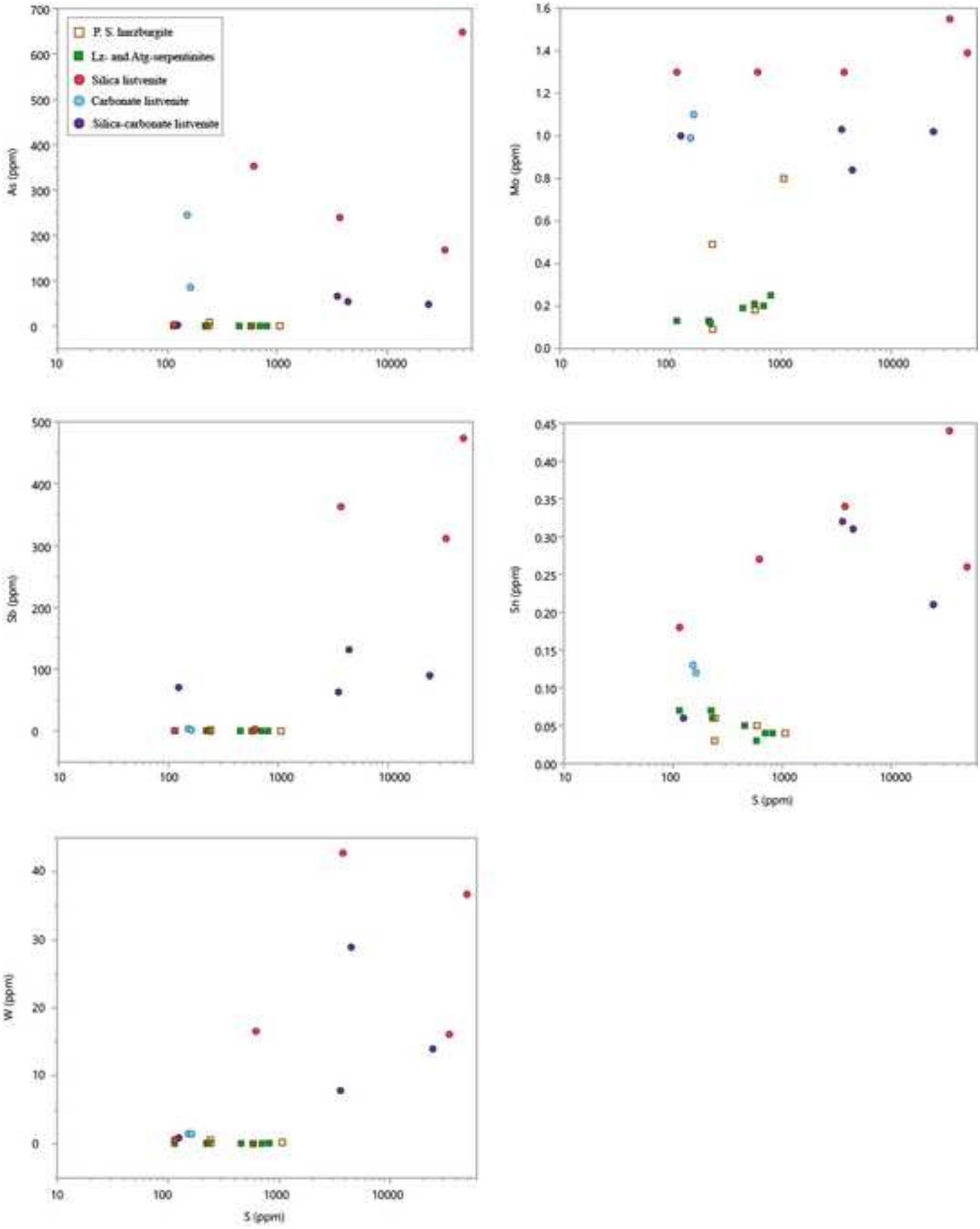

Table 1

Table 1 Classification of rock types and veins and their mineral parageneses in Hangaran area.

Sample	Locality	Northing	Easting	Mineralogy (microscopy/Raman/SEM)*			Description/Texture
				M	m	tr	
Partially serpentinized Harzburgite							
H2-1	Hangaran I	32° 06' 02.9''	059° 12' 37.1''	Ol + En + Lz + Brc	Di + Bst + Ctl	Chr ± Mag + Pn ± Cpy ± Atg ± Mgs ± Awr ± Hzl ± Mlr ± native Cu ± Mag	Mesh with minor interpenetrating
H2-7	Hangaran I	32° 06' 03.0''	059° 12' 37.0''				
H2-26	Hangaran I	32° 05' 30.0''	059° 13'05.6''				
H2-27	Hangaran I	32° 05' 30.0''	059° 13'05.6''				
H2-32	Hangaran I	32° 06' 03.4''	059° 13' 19.1''				
H2-44	Hangaran I	32° 05' 57.0''	059° 13' 14.5''				
H2-45	Hangaran I	32° 05' 53.2''	059° 13' 15.7''				
Lz-serpentinite							
H2-2	Hangaran I	32° 06' 02.9''	059° 12' 37.1''	Lz	Atg + Bst + Ctl	Chr + Mag ± Mgs ± Clc ± Pn ± Mlr ± Cpy ± Hzl	Mesh, minor interpenetrating & transitional
H2-20	Hangaran I	32° 06' 09.5''	059° 12' 34.9''				
H2-43	Hangaran I	32° 05' 57.0''	059° 13' 14.5''				
Atg-serpentinite							
H1-11	Hangaran II	32° 04' 55.6''	059° 13' 30.0''	Atg	Mgs ± Tlc	Lz + Chr + Fchr + (Cr-) Mag ± Dol ± Pn ± Mlr ± Gnt ± Cpy ± Hem	Interpenetrating, minor transitional
H1-26	Hangaran II	32° 04' 39.2''	059° 13' 22.0''				
H1-30	Hangaran II	32° 04' 37.0''	059° 13' 20.0''				
Silica-carbonate listvenite							
C-0	Hangaran II	32° 04' 50.0''	059° 13' 29.0''	Mgs + Qz	Dol	Serp + Chr + Fchr + (Cr-) Mag ± Hem ± Tlc ± Mlr ± Cpy ± Hzl ± Vlt ± Brt ± Fu ± Clc	Mesh or pesoudomorph, minor breccia & foliation
C-1	Hangaran II	32° 04' 50.0''	059° 13' 29.0''				
C-3	Hangaran II	32° 04' 50.0''	059° 13' 29.0''				
H2-34	Hangaran I	32° 06' 00.7''	059° 13' 17.1''				
H2-35	Hangaran I	32° 06' 00.7''	059° 13' 17.1''				
H2-38	Hangaran I	32° 06' 00.0''	059° 13' 16.0''				
Carbonate listvenite							
H2-13	Hangaran I	32° 06' 09.5''	059° 12' 34.9''	Mgs	Dol ± Qz	Chr + Fchr + (Cr-) Mag ± Hem ± Ctl ± Mlr ± Cpy ± Hzl ± Vlt ± Brt	Mesh or pesoudomorph, minor breccia & foliation
H2-16	Hangaran I	32° 06' 05.9''	059° 12' 41.0''				
H2-37	Hangaran I	32° 06' 00.7''	059° 13' 17.1''				
Silica listvenite							
H1-18	Hangaran II	32° 04' 45.7''	059° 13' 30.9''	Qz	Mgs + Dol	Chr + Fchr + (Cr-) Mag ± Hem ± Py + Bvt ± Mlr ± Rut ± Vlt ± Cov ± Gth ± Mlc ± Cin ± Fu ± Clc	Breccia, minor mesh
C-2	Hangaran II	32° 04' 50.0''	059° 13' 29.0''				
H1-21	Hangaran II	32° 04' 43.5''	059° 13' 29.0''				
H1-22	Hangaran II	32° 04' 43.5''	059° 13' 29.0''				
H2-14	Hangaran I	32° 06' 05.9''	059° 12' 41.0''				
H2-15	Hangaran I	32° 06' 05.9''	059° 12' 41.0''				
Cryptocrystalline magnesite vein							
H2-3	Hangaran I	32° 06' 03.0''	059° 12' 37.0''	Mgs		Dol ± Qz	Cryptocrystalline, stockwork
H2-4	Hangaran I	32° 06' 03.0''	059° 12' 37.0''				
H2-30	Hangaran I	32° 05' 58.3''	059° 13' 07.6''				
Dolomite vein							
H1-2	Hangaran II	32° 05' 12.3''	059° 13' 43.0''	Dol	± Sd/Cal ± Qz	Fe-oxides ± Py ± Cin ± Brt	Coarse to micro crystalline, vein, breccia
H1-5	Hangaran II	32° 05' 05.9''	059° 13' 37.3''				
H1-23	Hangaran II	32° 04' 43.5''	059° 13' 29.0''				
H2-9	Hangaran I	32° 06' 09.3''	059° 12' 34.5''				
H2-12	Hangaran I	32° 06' 09.3''	059° 12' 34.5''				
Pelagic limestone							
H1-31	Hangaran II	32° 04' 59.1''	059° 12' 33.1''	Cal			
H1-45	Hangaran II	32° 05' 01.3''	059° 15' 20.6''				

* Mineral identification by a combination of different methods performed on the majority of samples. M = major phase, m = minor phase, tr = trace phase, C = drill core samples. Mineral abbreviations: Ol-olivine, En-enstatite, Di-diopside, Serp-serpentine, Lz-lizardite, Atg-antigorite, Ctl-chrysotile, Brc-brucite, Bst-bastite, Clc-clinochlore, Tlc-talc, Amp-amphibole, Mgs-magnesite, Dol-dolomite, Sd-siderite, Cal-calcite, Qz-quartz, Chr-chromite, Fchr-ferritchromite, (Cr-) Mag-(Cr-) magnetite, Pn-pentlandite, Awr-awaruite, Hzl-heazlewoodite, Cpy-chalcopyrite, Mlr-millerite, Gnt-garnierite, Py-pyrite, Cin-cinnabar, Bvt- bravoite, Rut-rutile, Vlt-violarite, Fu-fuchsite, Cov-covelite, Brt-barite, Gth-geothite

Table 2

Table 2 Whole rock compostions of partially serpentinized harzburgites, Lz- and Atg-serpentinites and listvenites in Hangaran area.

Lithology	Partially serpentinized harzburgite							Lz-serpentinite			Atg-serpentinite		
Sample	H2-1	H2-7	H2-26	H2-27	H2-32	H2-44	H2-45	H2-2	H2-20	H2-43	H1-11	H1-26*	H1-30
SiO_2 (%)	39.3	39.4	39.1	40.4	40.2	39.7	40.4	38.7	39.1	38.5	35.2	41.2	34.7
TiO_2	0.01	0.01	0.01	0.01	0.01	0.01	0.01	0.01	<0.01	0.01	0.01	0.01	0.01
Al_2O_3	0.78	0.87	1.04	1.00	1.05	0.62	0.99	0.73	0.43	0.45	0.35	1.07	0.31
Fe_2O_3	7.79	6.95	8.38	8.09	7.86	8.30	8.64	7.77	7.55	8.64	8.17	7.17	10.2
MnO	0.09	0.11	0.12	0.12	0.12	0.10	0.12	0.04	0.08	0.07	0.13	0.09	0.09
MgO	39.0	38.0	37.5	37.8	37.2	37.3	38.5	38.2	36.1	36.5	34.9	36.9	34.2
CaO	0.42	0.38	0.29	0.91	0.98	0.25	1.34	0.02	0.07	0.12	3.78	1.09	1.00
Na_2O	0.09	0.18	0.06	0.08	0.05	0.06	<0.01	0.08	0.08	0.26	<0.01	0.07	0.09
K_2O	0.02	0.03	0.02	0.02	0.02	0.01	0.01	0.02	0.02	0.03	0.02	0.02	0.03
P_2O_5	<0.01	<0.01	<0.01	<0.01	<0.01	<0.01	<0.01	<0.01	<0.01	<0.01	<0.01	0.01	<0.01
LOI	11.50	12.00	14.20	11.75	10.25	11.75	8.08	14.60	14.25	14.30	15.40	12.55	19.35
Total	99.42	98.31	101.10	100.60	98.09	98.45	98.49	100.56	98.07	99.27	98.33	100.53	100.40
S %	0.01	0.06	0.05	0.04	0.02	0.07	0.02	0.05	0.02	0.09	0.02	<0.01	<0.01
Au (ppb)	0.20	0.69	2.41	0.81	1.39	1.33	1.12	0.41	0.31	0.37	3.77	2.56	0.78
Ag (ppm)	0.002	0.007	0.011	0.020	0.011	0.136	0.011	0.008	0.010	0.009	0.004	0.003	0.021
As	0.08	0.08	0.12	0.07	0.30	0.08	0.15	0.21	0.13	0.38	7.53	9.12	9.31
Ba	0.40	0.18	0.85	0.54	0.22	0.23	0.02	0.64	0.86	0.86	1.22	2.75	3.65
Ce	0.019	0.003	0.006	0.009	0.005	0.004	0.005	0.006	0.006	0.005	0.044	0.112	0.028
Co	102	110	98	108	102	106	102	104	101	127	115	113	111
Cr	2820	2910	2720	3050	3070	2720	3060	2910	2880	3060	2810	3030	3110
Cs	0.67	1.21	0.31	1.47	2.02	0.58	1.07	0.01	0.30	0.25	0.05	0.10	1.32
Cu	1.19	13.27	15.85	18.57	5.12	16.73	24.79	0.63	7.83	4.36	3.51	5.98	7.93
Dy	0.010	0.025	0.038	0.030	0.040	0.013	0.028	0.010	0.010	0.007	0.007	0.041	0.011
Er	0.013	0.040	0.032	0.031	0.043	0.014	0.038	0.018	0.005	0.006	0.006	0.032	0.009
Eu	0.0004	0.0001	0.0007	0.0014	0.0001	_	_	0.0004	_	_	0.0187	0.0259	0.0056
Ga	0.81	0.88	0.99	0.93	1.01	0.63	0.99	0.82	0.50	0.58	0.52	0.95	0.43
Gd	0.003	0.005	0.008	0.011	0.013	0.007	0.011	0.003	0.004	0.006	0.002	0.021	0.012
Hf	0.001	_	0.002	0.004	0.003	0.001	0.002	0.001	0.001	0.001	0.004	0.009	0.005
Ho	0.003	0.009	0.011	0.009	0.013	0.004	0.008	0.005	0.003	0.003	0.002	0.010	0.002
La	0.007	0.001	0.004	0.001	0.002	0.001	0.001	0.004	0.005	0.002	0.041	0.024	0.011
Li	1.19	3.89	1.94	6.69	1.63	6.25	2.30	0.53	11.30	3.61	0.54	1.39	19.50
Lu	0.006	0.014	0.008	0.008	0.012	0.009	0.009	0.009	0.003	0.005	0.004	0.009	0.004
Mo	0.12	0.17	0.18	0.17	0.11	0.21	0.12	0.15	0.41	0.67	0.08	0.10	0.47
Nb	0.064	0.045	0.037	0.071	0.076	0.051	0.098	0.020	0.035	0.012	0.055	0.067	0.044
Nd	0.005	0.001	0.005	0.002	0.001	_	0.003	0.001	0.002	0.008	0.011	0.100	0.024
Ni	2063	2242	1906	2123	1943	2026	1965	2072	2082	2498	2043	1940	2133
Pb	0.11	0.00	0.02	0.01	0.52	0.01	0.00	0.03	0.04	0.02	0.17	0.48	1.56
Pr	0.000	_	0.000	0.001	0.001	0.000	0.000	0.001	0.001	0.001	0.003	0.017	0.006
Rb	0.26	0.40	0.08	0.46	0.38	0.16	0.49	0.02	0.16	0.12	0.04	0.04	0.28
Sb	0.06	0.06	0.03	0.02	0.06	0.03	0.04	0.03	0.03	0.08	1.51	0.43	0.55
Sc	10.04	10.53	11.48	12.17	12.26	9.16	13.10	10.24	8.22	8.37	9.63	9.66	6.55
Sm	0.003	0.000	0.004	0.001	0.003	0.003	_	_	_	0.002	0.000	0.022	0.002
Sn	0.06	0.04	0.02	0.05	0.06	0.03	0.06	0.04	0.03	0.04	0.05	0.04	0.05
Sr	4.89	1.10	3.35	28.46	2.24	3.27	0.04	2.52	5.71	19.37	23.40	5.33	14.65
Tb	0.000	0.001	0.004	0.002	0.003	0.001	0.002	0.001	0.000	0.001	0.000	0.005	0.001
Th	0.004	0.000	0.001	0.002	0.002	0.001	0.005	0.001	0.001	0.003	0.003	0.001	0.002
Tm	0.002	0.006	0.007	0.006	0.007	0.003	0.005	0.002	_	0.001	0.001	0.006	0.000
U	0.002	0.000	0.000	0.000	0.000	0.001	_	0.001	_	0.007	0.000	0.001	0.002
V	40	41	43	47	46	36	52	41	28	33	30	36	21
W	0.07	0.06	0.06	0.08	0.07	0.11	0.10	0.03	0.50	0.20	0.09	0.13	0.18
Y	0.10	0.20	0.28	0.21	0.32	0.12	0.19	0.11	0.07	0.08	0.04	0.25	0.07
Yb	0.030	0.035	0.055	0.054	0.079	0.030	0.049	0.043	0.020	0.028	0.016	0.058	0.016
Zn	29	44	35	40	38	39	39	29	38	50	35	45	52
Zr	0.06	0.02	0.05	0.06	0.03	0.25	0.04	0.01	0.04	0.03	0.06	0.24	0.17

(*) Atg-Tlc-Mgs: talc-bearing Atg-serpentinite.

Table 2 (continued)

Table 2 (continued)

Lithology	Silica-carbonate listvenite						Carbonate listvenite			Silica listvenite					
Sample	C-0	C-1	C-3	H2-34	H2-35	H2-38	H2-13	H2-16	H2-37	H1-18	C2	H1-21	H1-22	H2-14	H2-15
SiO_2 (%)	41.2	35.8	45.6	48.1	38.2	45.9	28.6	28.6	18.7	64.4	75.2	96.1	83.4	87.6	89.6
TiO_2	0.02	0.02	0.10	<0.01	<0.01	<0.01	<0.01	0.01	<0.01	0.12	0.01	0.08	0.02	0.01	<0.01
Al_2O_3	0.69	0.51	2.84	0.27	0.39	0.34	0.15	0.28	0.33	7.20	0.88	0.99	0.90	0.99	0.46
Fe_2O_3	4.39	7.13	5.34	7.54	5.64	3.16	5.80	6.84	2.64	3.65	4.80	1.04	7.43	7.99	6.08
MnO	0.07	0.14	0.09	0.14	0.07	0.07	0.06	0.12	0.16	0.06	0.03	0.02	0.02	0.01	<0.01
MgO	21.7	18.1	18.1	18.9	24.2	21.1	35.2	27.2	16.9	3.90	6.47	0.07	0.82	0.50	0.21
CaO	1.99	6.85	1.99	5.42	0.96	2.60	0.09	2.60	22.8	7.86	1.40	0.18	1.11	0.05	0.79
Na_2O	0.07	0.02	0.08	0.02	0.09	0.09	0.10	0.09	0.10	0.09	0.08	0.14	0.03	0.04	0.04
K_2O	0.03	0.04	0.04	<0.01	0.03	0.05	0.02	0.03	0.03	0.05	0.06	0.15	0.06	0.09	0.05
P_2O_5	<0.01	<0.01	<0.01	<0.01	<0.01	<0.01	<0.01	<0.01	<0.01	<0.01	<0.01	<0.01	<0.01	0.01	<0.01
LOI	27.60	26.00	24.30	20.80	28.30	26.20	28.20	33.10	37.30	14.15	9.87	1.97	5.02	2.22	2.12
Total	98.12	94.96	98.81	101.66	98.22	99.77	98.54	99.24	99.25	101.70	99.14	100.98	99.04	100.05	99.64
S %	0.25	1.66	0.33	0.01	<0.01	<0.01	<0.01	0.01	0.01	0.01	3.03	0.37	4.61	<0.01	0.06
Au (ppb)	0.60	0.60	1.10	0.16	0.82	0.47	0.18	1.30	0.40	2.53	1.21	0.21	2.73	0.82	1.30
Ag (ppm)	0.013	0.006	0.019	0.026	0.023	0.028	0.005	0.046	0.096	0.009	0.009	0.009	0.047	0.023	0.035
As	46.19	32.87	40.13	1.70	2.60	16.06	2.00	161.11	52.74	2.91	149.12	236.32	607.88	313.00	343.20
Ba	9.272	12.905	10.349	57.65	33.74	8.61	2.43	43.44	15.46	15.22	10.30	18.11	20.18	14.00	10.87
Ce	0.572	0.226	3.149	0.001	0.073	0.100	0.008	0.104	0.215	0.381	0.052	0.314	0.039	0.010	0.018
Co	75	116	75	104	77	77	90	58	79	20	99	12	74	65	25
Cr	2790	2610	2520	3210	2460	1900	2010	2820	1760	1500	2620	1840	1740	3630	2020
Cs	2.23	1.80	4.06	0.40	1.72	3.14	0.12	0.52	1.77	2.22	4.65	8.05	5.52	8.05	5.42
Cu	4.74	2.75	10.83	3.82	3.16	3.39	0.47	3.99	19.30	1.55	10.12	3.91	18.56	17.95	6.48
Dy	0.119	0.124	0.326	0.007	0.022	0.009	0.002	0.009	0.110	0.448	0.024	0.402	0.029	_	0.003
Er	0.067	0.093	0.186	0.008	0.011	0.009	0.000	0.017	0.099	0.370	0.019	0.303	0.023	0.008	0.003
Eu	0.0229	0.0232	0.1197	0.0001	0.0026	0.0397	0.0000	0.0044	0.2189	0.0506	0.0043	0.0250	0.0040	_	_
Ga	1.47	2.55	2.69	0.31	0.61	0.58	0.24	0.46	0.81	6.19	2.46	1.50	1.41	0.78	0.50
Gd	0.112	0.086	0.329	0.002	0.012	0.004	_	0.007	0.077	0.244	0.013	0.216	0.026	_	0.005
Hf	0.030	0.023	0.056	0.004	0.001	0.006	_	0.002	0.008	0.144	0.019	0.192	0.023	0.011	0.018
Ho	0.021	0.028	0.071	0.001	0.005	0.001	0.001	0.004	0.032	0.116	0.007	0.084	0.009	0.002	0.001
La	0.265	0.098	1.432	0.002	0.040	0.121	0.003	0.105	0.143	0.160	0.040	0.143	0.019	0.006	0.011
Li	10.77	17.97	17.71	20.27	20.04	18.81	17.44	20.13	11.60	19.02	18.52	32.08	24.29	45.80	21.24
Lu	0.015	0.013	0.021	0.002	0.004	0.004	0.002	0.002	0.015	0.064	0.003	0.031	0.002	_	0.001
Mo	0.72	0.70	0.62	0.80	0.69	0.82	0.05	0.65	0.68	1.13	1.38	1.28	1.31	1.45	1.26
Nb	0.597	0.398	2.075	0.265	0.512	0.699	0.031	0.119	0.105	0.603	1.019	0.944	0.920	0.394	0.695
Nd	0.301	0.157	1.612	_	0.053	0.015	0.001	0.033	0.117	0.239	0.012	0.238	0.037	_	0.016
Ni	1479	1606	1261	2547	1523	1155	1908	1104	1176	166	1796	140	1498	1730	748
Pb	0.33	0.63	1.51	0.70	0.46	1.46	0.00	1.27	7.91	0.09	1.19	0.23	2.38	0.01	0.06
Pr	0.077	0.033	0.389	0.001	0.011	0.005	0.001	0.006	0.034	0.046	0.004	0.048	0.003	_	0.003
Rb	0.89	0.88	1.78	0.15	0.84	1.21	0.09	0.31	0.80	1.64	2.45	3.92	3.04	4.21	1.66
Sb	44.30	61.64	97.60	56.75	2.33	4.51	0.06	2.43	1.00	0.59	276.80	358.23	444.05	4.44	3.02
Sc	5.42	7.04	5.90	2.71	6.75	4.01	2.45	6.97	6.82	22.43	1.84	0.51	1.09	2.81	1.00
Sm	0.092	0.044	0.433	_	0.005	_	0.000	0.009	0.056	0.127	0.006	0.113	0.016	_	0.002
Sn	0.22	0.14	0.23	0.05	0.12	0.21	0.03	0.08	0.07	0.16	0.39	0.33	0.24	0.11	0.26
Sr	15.11	46.15	24.73	47.73	27.65	66.87	6.41	52.69	487.25	73.89	15.59	29.91	21.24	10.40	22.06
Tb	0.019	0.015	0.048	0.000	0.002	0.001	_	0.002	0.015	0.056	0.002	0.044	0.005	_	0.001
Th	0.024	0.015	0.196	0.001	0.001	0.006	0.001	0.002	0.004	0.111	0.005	0.107	0.007	0.008	0.004
Tm	0.010	0.010	0.020	0.000	0.002	0.001	_	0.001	0.012	0.055	0.003	0.041	0.001	0.002	_
U	0.035	0.033	0.081	0.001	0.033	0.015	0.000	0.188	0.072	0.068	0.010	0.049	0.067	0.050	0.072
V	32	43	41	7	22	17	9	25	23	144	32	16	15	31	13
W	5.50	9.58	21.46	0.72	1.10	0.97	0.13	0.98	0.91	0.56	14.32	42.23	34.41	16.50	16.10
Y	0.61	0.63	1.64	0.03	0.16	0.08	0.02	0.10	0.95	2.85	0.16	1.94	0.17	0.05	0.03
Yb	0.082	0.085	0.168	0.009	0.022	0.014	0.007	0.022	0.090	0.390	0.027	0.207	0.023	0.008	0.003
Zn	41	45	52	34	29	21	28	43	37	20	83	34	30	28	13
Zr	0.58	0.45	1.64	0.04	0.06	0.19	0.02	0.13	0.50	2.85	0.36	6.11	0.59	0.30	0.92

Table 3

Table 3 Geochemical and isotopic data of carbonates in Hangaran carbonate-bearing lithologies

Sample	Fraction	Description	Rb	Sr	$^{87}Rb/^{86}Sr$	$^{87}Sr/^{86}Sr$		$(^{87}Sr/^{86}Sr)_{59\ Ma}$	$\delta^{13}C$	$\delta^{18}O$	$\delta^{34}S$
			(ppm)			(measured)	±2SE		(‰ VPDB)	(‰ VSMOW)	(‰ VCDT)
Partially serpentinized harzburgite											
H2-7	Bulk	Mgs	_	_	_	_	_	_	-5.88	12.19	_
H2-26	Bulk	Mgs	_	_	_	_	_	_	-6.47	12.74	_
Lz-serpentinite											
H2-20	Bulk	minor Mgs	_	_	_	_	_	_	-5.86	15.08	_
Atg-serpentinite											
H1-11	Bulk	Mgs, trace Dol	0.007	5.34	0.004	0.706562	0.000016	0.706559	-1.77	15.28	_
H1-30	Bulk	Mgs, trace Dol	0.032	3.14	0.030	0.707177	0.000013	0.707152	-8.31	14.77	_
Silica-carbonate listvenite											
C-0b*	Bulk, core	Mgs	0.894	15.11	0.171	0.707024	0.00004	0.706881	-0.33	22.02	_
C-0v	Vein in C-0b	Dol vein	_	_	_	_	_	_	-6.41	22.17	_
C-1b	Bulk, core	Mgs	0.003	3.97	0.002	0.706474	0.000014	0.706472	-0.06	21.55	_
C-1v	Vein in C-1b	Dol, Py vein	_	_	_	_	_	_	-6.94	22.01	
C-1s1	Vein	Py vein	_	_	_	_	_	_	_	_	3.24
C-3b	Bulk, core	Mgs	0.003	4.57	0.002	0.706178	0.000016	0.706176	2.78	25.58	_
C-3v	Vein in C-3b	Dol vein	_	_	_	_	_	_	-5.59	21.10	_
H2-34	Bulk	Mgs+Dol	_	_	_	_	_	_	-6.86	17.48	_
H2-38	Bulk	Mgs	_	_	_	_	_	_	-3.12	24.34	_
Carbonate listvenite											
H2-13	Bulk	Mgs	_	_	_	_	_	_	-8.46	17.72	_
H2-16	Bulk	Mgs, minor Dol	_	_	_	_	_	_	-4.23	16.91	_
H2-37	Bulk	Dol, minor Mgs	_	_	_	_	_	_	2.55	22.37	_
Silica listvenite											
C-2b	bulk, core	Mgs, minor Dol	0.112	2.98	0.109	0.706769	0.000015	0.706678	-1.53	23.13	_
C-2-s	Vein in C-2b	Py vein	_	_	_	_	_	_	_	_	0.28
H1-18	Bulk	Mgs, Dol	_	_	_	_	_	_	-0.11	19.27	_
H1-22a	Bulk	Dol & Py vein	_	_	_	_	_	_	0.19	19.40	_
H1-22b	Bulk	Py vein	_	_	_	_	_	_	_	_	6.72
Cryptocrystalline magnesite vein											
H2-3	Bulk	Mgs, traces Dol	_	_	_	_	_	_	-9.56	21.73	_
H2-4	Bulk	Mgs, traces Dol	0.001	103.30	0.00003	0.707966	0.000013	0.707966	-8.74	18.87	_
H2-30	Bulk	Mgs, traces Dol	_	_	_	_	_	_	-11.98	22.95	_
Dolomite vein (surface outcrop)											
H1-2	Bulk	Dol, minor Sd	_	_	_	_	_	_	-0.87	20.96	_
H1-5	Bulk	Dol, minor Sd	_	_	_	_	_	_	-1.44	20.26	_
H1-23	Bulk	Dol	0.247	22.30	0.032	0.707555	0.000015	0.707528	-1.53	23.83	_
H2-9	Bulk	Dol	_	_	_	_	_	_	-0.98	20.31	_
H2-12	Bulk	Dol							2.54	22.33	_
Pelagic limestone											
H1-31-a	Bulk	Cal	0.18	863.40	0.001	0.707816	0.000015	0.707815	1.96	25.42	_
H1-31-b	Bulk	Cal	_	_	_	_	_	_	1.93	25.94	_
H1-45	Bulk	Cal	_	_	_	_	_	_	2.41	25.23	_

* Rb and Sr concentration, measured by ICPMS (Table 2). Abbreviations: Mgs-magnesite, Dol-dolomite, Sd-siderite, Cal-calcite, Py-pyrite.

Table 4

Table 4 Representative electron microprobe analyses of olivine, clinopyroxene, orthopyroxene, lizardite, antigorite, bastite, magnesite and dolomite.

Rock type	Partially-serpentinized peridotite												Lz-serpentinite						Atg-Serpentinite (carbonated)				
Sample	H2-27												H2-2						H1-11		H1-30		
Mineral	Ol		Cpx		Opx		Lz after Ol		Bst after Opx		Late Lz		Lz		Atg		Bst after Opx		Atg		Dol		Mgs
Comment							mesh rim		Lz		Vein		mesh center		mesh rim		mainly Lz		matrix		vein		matrix
	Average	S.D.	Average	S.D.	Average	S.D.	Average	S.D.	Average	S.D.	Average	S.D.	Average	S.D.	Average	S.D.	Average	S.D.	Average	S.D.	Average	S.D.	
Wt.%																							
SiO_2	39.67	0.16	52.11	0.26	55.03	0.50	38.26	0.66	37.67	0.46	40.45	0.45	40.17	0.69	42.62	0.54	37.85	0.99	42.81	0.21	0.33	0.20	0.47
TiO_2	0.002	0.01	0.05	0.01	0.02	0.01	0.00	0.01	0.01	0.01	0.00	0.00	0.01	0.01	0.00	0.01	0.01	0.01	0.002	0.01	0.00	0.00	0.00
Cr_2O_3	0.01	0.01	0.75	0.08	0.63	0.12	0.02	0.02	0.01	0.02	0.01	0.02	0.03	0.02	0.05	0.06	0.80	0.10	0.03	0.03	0.01	0.01	0.02
Al_2O_3	0.01	0.01	2.69	0.14	2.65	0.18	0.01	0.02	0.35	0.12	0.06	0.11	0.58	0.04	0.07	0.06	0.70	0.21	0.15	0.06	0.00	0.01	0.00
FeO (tot)	8.88	0.13	2.10	0.10	5.80	0.22	5.82	1.47	6.24	0.93	3.08	0.19	4.27	0.37	3.53	0.51	6.85	1.54	2.76	0.27	0.22	0.08	1.84
MnO	0.12	0.05	0.08	0.04	0.14	0.03	0.09	0.04	0.14	0.03	0.08	0.03	0.07	0.03	0.04	0.03	0.10	0.04	0.03	0.03	0.03	0.02	0.06
NiO	0.37	0.04	0.04	0.03	0.10	0.04	0.37	0.05	0.37	0.10	0.10	0.19	0.20	0.04	0.18	0.02	0.18	0.05	0.20	0.06	0.00	0.00	0.15
MgO	49.74	0.17	17.09	0.12	33.41	0.32	38.62	1.01	38.67	2.31	39.36	0.38	39.35	0.66	37.92	0.32	37.30	0.65	38.92	0.24	20.69	1.03	44.13
CaO	0.01	0.01	23.82	0.14	0.79	0.16	0.06	0.03	0.09	0.02	0.03	0.01	0.04	0.01	0.01	0.01	0.03	0.01	0.01	0.01	30.25	0.17	0.15
SrO	n.d.		n.d.		n.d.		n.d.		n.d.		n.d.		n.d.		n.d.		n.d.		n.d.		0.079	0.044	0.007
Na_2O	0.01	0.01	0.05	0.02	0.01	0.02	0.01	0.01	0.01	0.01	0.02	0.01	0.01	0.01	0.01	0.01	0.01	0.01	0.01	0.01	0.002	0.003	0.013
K_2O	0.01	0.01	0.01	0.01	0.01	0.01	0.01	0.01	0.01	0.01	0.01	0.01	0.01	0.01	0.01	0.01	0.003	0.004	0.01	0.01	0.00	0.00	0.00
V_2O_3	0.002	0.01	0.03	0.03	0.03	0.02	0.01	0.02	0.02	0.02	0.01	0.02	0.02	0.01	0.01	0.01	0.02	0.02	0.002	0.01	n.d.		n.d.
CO_2																					46.77		49.93
Total	98.82		98.81		98.62		83.29		83.59		83.23		84.75		84.45		83.88		84.93		98.39		96.78
$XCaCO_3$																					0.51		0.002
$XMgCO_3$																					0.48		0.97
$XFeCO_3$																					0.003		0.023
$XMnCO_3$																					0.0004		0.001
N	12		6		12		14		10		13		6		9		11		12		3		1
atom-per-formula-unit (p.f.u.)																							
Si	0.98	0.00	1.91	0.01	1.92	0.01	1.89	0.02	1.86	0.06	1.98	0.01	1.94	0.03	2.08	0.02	1.87	0.04	2.07	0.01	0.02	0.01	0.01
Ti	0.000	0.000	0.001	0.000	0.001	0.000	0.000	0.000	0.000	0.000	0.000	0.000	0.000	0.001	0.000	0.000	0.001	0.001	0.000	0.000	0.000	0.000	0.000
Cr	0.000	0.000	0.022	0.002	0.017	0.003	0.001	0.001	0.001	0.001	0.000	0.001	0.001	0.001	0.002	0.002	0.031	0.004	0.001	0.001	0.000	0.001	0.000
Al	0.000	0.000	0.116	0.006	0.109	0.007	0.001	0.001	0.021	0.007	0.003	0.006	0.033	0.002	0.004	0.003	0.041	0.012	0.008	0.003	0.000	0.000	0.000
Fe^{3+}	0.000	0.000	0.034	0.012	0.025	0.018	0.000	0.000	0.000	0.000	0.000	0.000	0.000	0.000	0.000	0.000	0.000	0.000	0.000	0.000	0.000	0.000	0.000
Fe^{2+}	0.183	0.003	0.031	0.011	0.144	0.013	0.241	0.063	0.257	0.035	0.126	0.008	0.173	0.015	0.144	0.020	0.284	0.065	0.111	0.011	0.012	0.004	0.023
Mn	0.003	0.001	0.003	0.001	0.004	0.001	0.004	0.001	0.006	0.001	0.003	0.001	0.003	0.001	0.002	0.001	0.004	0.002	0.001	0.001	0.001	0.001	0.001
Ni	0.007	0.001	0.001	0.001	0.003	0.001	0.015	0.002	0.015	0.004	0.004	0.007	0.008	0.001	0.007	0.001	0.007	0.002	0.008	0.002	0.000	0.000	0.002
Mg	1.828	0.005	0.936	0.006	1.741	0.007	2.843	0.051	2.837	0.063	2.875	0.013	2.836	0.047	2.759	0.026	2.753	0.035	2.801	0.014	1.931	0.058	0.965
Ca	0.000	0.000	0.938	0.006	0.030	0.006	0.003	0.001	0.005	0.001	0.002	0.001	0.002	0.000	0.001	0.001	0.002	0.000	0.001	0.001	2.031	0.044	0.002
Sr	n.d.		n.d.		n.d.		n.d.		n.d.	n.d.	n.d.		n.d.		n.d.		n.d.		n.d.		0.003	0.002	0.000
Na	0.000	0.000	0.003	0.001	0.001	0.001	0.001	0.001	0.001	0.001	0.002	0.001	0.001	0.001	0.001	0.001	0.001	0.001	0.001	0.001	0.000	0.000	0.000
K	0.000	0.000	0.000	0.000	0.000	0.000	0.001	0.000	0.000	0.000	0.001	0.000	0.000	0.000	0.000	0.000	0.000	0.000	0.000	0.000	0.000	0.000	0.000
V	0.000	0.000	0.001	0.001	0.001	0.000	0.000	0.001	0.001	0.001	0.001	0.001	0.001	0.001	0.000	0.000	0.001	0.001	0.000	0.000	n.d.		n.d.
Total	3		4		4		5		5		5		5		5		5		5		4		1
Mg/Si	1.87	0.01	0.49	0.00	0.90	0.01	1.50	0.02	1.53	0.09	1.45	0.01	1.46	0.05	1.33	0.02	1.47	0.02	1.36	0.01	129.64	64.68	139.65
Mg#	0.91	0.001	0.97	0.01	0.92	0.01	0.92	0.02	0.92	0.01	0.96	0.003	0.94	0.01	0.95	0.01	0.91	0.02	0.96	0.004	0.99	0.00	0.98

N = number of point analysis; CO_2 by stoichiometry after ZAF correction; S.D. = standard deviation; n.d. = not detected. Mineral abbreviations: Ol-olivine, Px-pyroxene, Cpx-clinopyroxene, Opx-orthpyroxene, Lz-lizardite, Atg-antigorite, Bst-bastite.

Mg# = $Mg/(Mg+Fe^{2+})$ atomic ratio.

Supplementary Table S1

Table S1 Representative microprobe analyses (wt.%) of chromian spinel from Hangaran harzburgite

sample	H2-45		H2-7		H2-27 (a)		H2-27 (b)		H2-32	
	Average	S.D.	Average	S.D.	Average	S.D.	Average	S.D.	Average	S.D.
SiO_2	0.00	0.00	0.00	0.00	0.00	0.00	0.008	0.015	0.00	0.00
TiO_2	0.05	0.01	0.05	0.02	0.04	0.02	0.03	0.01	0.05	0.03
Al_2O_3	32.87	0.69	34.09	1.25	35.14	1.38	35.46	0.43	35.83	1.11
Cr_2O_3	36.44	0.88	34.80	1.54	33.98	1.50	33.27	0.52	33.17	1.33
V_2O_3	0.21	0.03	0.18	0.03	0.20	0.04	0.20	0.03	0.16	0.03
FeO (tot)	16.57	0.69	16.22	0.19	15.67	0.43	15.60	0.30	15.95	0.49
MnO	0.12	0.04	0.10	0.03	0.11	0.03	0.09	0.03	0.12	0.03
MgO	14.14	0.37	14.62	0.20	14.83	0.29	14.70	0.24	14.77	0.17
CaO	n.d.	n.d.	n.d.	n.d.	n.d.	n.d.	n.d.	n.d.	n.d.	n.d.
ZnO	n.d.	n.d.	n.d.	n.d.	n.d.	n.d.	0.22	0.09	0.23	0.07
NiO	0.12	0.04	0.13	0.03	0.12	0.03	0.12	0.04	0.16	0.05
Na_2O	n.d.	n.d.	n.d.	n.d.	n.d.	n.d.	n.d.	n.d.	n.d.	n.d.
K_2O	n.d.	n.d.	n.d.	n.d.	n.d.	n.d.	n.d.	n.d.	n.d.	n.d.
Total	100.51	0.83	100.19	0.46	100.10	0.34	99.71	0.44	100.43	0.37
n	12		11		12		17		17	
atom-per-formula-unit (p.f.u.)										
Si	0.00	0.00	0.00	0.00	0.00	0.00	0.0002	0.0004	0.00	0.00
Ti	0.001	0.000	0.001	0.001	0.001	0.001	0.001	0.0004	0.001	0.001
Al	1.13	0.02	1.17	0.04	1.20	0.04	1.21	0.01	1.21	0.03
Cr	0.84	0.02	0.80	0.04	0.78	0.04	0.76	0.01	0.75	0.03
V	0.005	0.001	0.004	0.001	0.005	0.001	0.005	0.001	0.004	0.001
Fe^{3+}	0.02	0.005	0.03	0.01	0.02	0.01	0.02	0.01	0.03	0.01
Fe^{2+}	0.38	0.01	0.36	0.01	0.36	0.01	0.36	0.01	0.36	0.01
Mn	0.003	0.001	0.003	0.001	0.003	0.001	0.002	0.001	0.003	0.001
Mg	0.61	0.01	0.63	0.01	0.64	0.01	0.63	0.01	0.63	0.01
Ca	n.d.	n.d.	n.d.	n.d.	n.d.	n.d.	n.d.	n.d.	n.d.	n.d.
Zn	n.d.	n.d.	n.d.	n.d.	n.d.	n.d.	0.005	0.002	0.005	0.002
Ni	0.003	0.001	0.003	0.001	0.003	0.001	0.003	0.001	0.004	0.001
Na	n.d.	n.d.	n.d.	n.d.	n.d.	n.d.	n.d.	n.d.	n.d.	n.d.
K	n.d.	n.d.	n.d.	n.d.	n.d.	n.d.	n.d.	n.d.	n.d.	n.d.
Total	3.00		3.00		3.00		3.00		3.00	
Cr#	0.43	0.01	0.41	0.02	0.39	0.02	0.39	0.01	0.38	0.02
Mg#	0.62	0.01	0.63	0.01	0.64	0.01	0.64	0.01	0.64	0.01
Fe^{3+}#	0.01	0.00	0.02	0.00	0.01	0.00	0.01	0.00	0.01	0.00

n = number of point analysis; n.d. = not determined; S.D. = standard deviation.

Cr# = Cr/(Cr+Al) atomic ration, Mg# = Mg/(Mg+Fe^{2+}) atomic ratio, Fe^{3+}# = Fe^{3+}/(Fe^{3+}+Cr+Al).